UNIVERSIDAD DE EXTREMADURA

Diseño e implementación eficiente de nuevos métodos de preprocesado espacial para desmezclado de imágenes hiperespectrales de la superficie terrestre

Gabriel Martín Hernández

2013

UNIVERSIDAD DE EXTREMADURA

TESIS DOCTORAL

Diseño e implementación eficiente de nuevos métodos de preprocesado espacial para desmezclado de imágenes hiperespectrales de la superficie terrestre

Design and implementation of new methods for spatial preprocessing prior to spectral unmixing of remotely sensed hyperspectral data

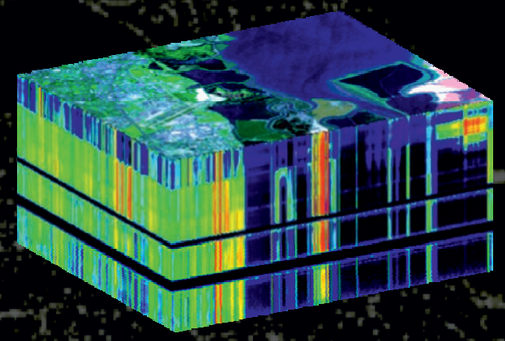

Gabriel Martín Hernández

Departamento de Tecnología
de los Computadores y las Comunicaciones

2013

UNIVERSIDAD  DE EXTREMADURA

Tesis Doctoral

Diseño e implementación eficiente de nuevos métodos de preprocesado espacial para desmezclado de imágenes hiperespectrales de la superficie terrestre

Design and implementation of new methods for spatial preprocessing prior to spectral unmixing of remotely sensed hyperspectral data

Autor: Gabriel Martín Hernández

DEPARTAMENTO DE TECNOLOGÍA DE LOS COMPUTADORES Y DE LAS COMUNICACIONES

Conformidad de los directores: Antonio Plaza Miguel
(Universidad de Extremadura)
José Bioucas Dias
(Universidade Técnica de Lisboa)

Fdo: Dr. Antonio Plaza Fdo: Dr. José Bioucas Dias

2013

Resumen

La principal contribución del presente trabajo de tesis doctoral viene dada por la propuesta e implementación de nuevas técnicas de análisis hiperespectral capaces de incorporar la información espacial en aplicaciones de desmezclado y obtención comprimida de imágenes hiperespectrales de la superficie terrestre. Los sensores hiperespectrales tienen la capacidad de medir la radiación reflejada por la superficie terrestre en cientos de canales a diferentes longitudes de onda obteniendo un cubo de datos multidimensional que normalmente comprende varios *gigabytes* por vuelo. Debido al tamaño extremadamente grande de los datos recogidos por los sensores hiperespectrales, la compresión de datos hiperespectrales ha obtenido un interés considerable en los últimos años. Estos datos normalmente son tomados por un satélite o un sensor aerotransportado, el cual los envía a la estación de Tierra para su posterior procesamiento. Normalmente el ancho de banda de la conexión entre el satélite/avión y la estación de Tierra es reducido, lo que limita la cantidad de datos que pueden ser transmitidos. Este hecho provoca que haya una clara necesidad de desarrollo de técnicas para la compresión de datos hiperespectrales que puedan ser empleadas a bordo del sensor. Por otra parte uno de los principales problemas que surge a la hora de caracterizar los elementos que aparecen en una escena hiperespectral se basa en el hecho de que muchos píxeles en la escena contienen varias sustancias a nivel sub-píxel, con lo que la firma espectral resultante en dichos píxeles no es pura sino que viene dada por una composición o mezcla de diferentes sustancias que cohabitan a nivel sub-píxel. La aproximación fundamental para caracterizar el fenómeno de la mezcla a nivel sub-píxel consiste en la utilización de un modelo lineal de mezcla que asume que cada fotón procedente de la radiación solar solamente interactúa con un único componente a nivel sub-píxel, de forma que la radiación total reflejada por un píxel mezcla se puede descomponer de forma proporcional a la abundancia de cada uno de los componentes (endmembers) que lo constituyen. La mayor parte de las técnicas de desmezclado se basan en la utilización de la información espectral de forma exclusiva. En este sentido, una de las principales contribuciones del presente trabajo de tesis doctoral es la integración de la información espacial y espectral con carácter previo al proceso de extracción de endmembers (a través de la propuesta de nuevos métodos de preprocesado espacial que permiten integrar la información espacial en las técnicas espectrales sin necesidad de modificarlas). Además en este trabajo de tesis ha sido propuesto un nuevo método para obtención comprimida de imágenes hiperespectrales, el cual aprovecha la correlación espacial de las imágenes hiperespectrales y el fenómeno de la mezcla para conseguir comprimir los datos en el proceso de adquisición. Las nuevas técnicas desarrolladas han permitido mejorar notablemente la representatividad espacial de los endmembers obtenidos y reducir los errores en la etapa de desmezclado al emplear endmembers más representativos desde el punto de vista espacial. De forma similar, los algoritmos de obtención comprimida pueden lograr unos *ratios* de compresión muy altos sin perder calidad espectral. Como se demuestra experimentalmente utilizando una base de datos de imágenes hiperespectrales sintéticas y reales (obtenidas por una variedad de sensores hiperespectrales, tales como Airborne Visible Infra-Red Imaging Spectrometer (AVIRIS)

de NASA), los nuevos desarrollos realizados con motivo de la presente tesis doctoral permiten modelar de forma muy precisa los patrones espaciales y espectrales presentes en la escena. Las simulaciones realizadas con datos sintéticos también analizan la sensibilidad al ruido de las técnicas desarrolladas, y permiten concluir que las técnicas desarrolladas pueden mejorar las prestaciones en presencia de ruido, tanto para las técnicas de preprocesado espacial como para las de obtención comprimida de la imagen.

Palabras clave: Análisis hiperespectral, compresión, desmezclado espectral, preprocesado espacial.

Abstract

The main contribution of this thesis is de development and implementation of new techniques for hyperspectral analysis which are able to incorporate the spatial component of the data when performing spectral unmixing and remote compressive sensing of hyperspectral images. Hyperspectral imaging spectrometers collect hundreds or thousands of bands (at different wavelength channels) resulting a multidimensional data cube which typically comprises several gigabytes per flight. Due to the extremely large volumes of data collected by imaging spectrometers, hyperspectral data compression has received considerable interest in recent years. These data are usually collected by a satellite or an airbone instrument and sent to a ground station on Earth for subsequent processing. Usually the bandwidth connection between the satellite/airborne platform and the ground station is reduced, which limits the amount of data that can be transmitted. As a result, there is a clear need for hyperspectral data compression techniques that can be applied onboard the imaging instrument. On the other hand, spectral mixing is one of the main problems that arise when characterizing the spectral constituents residing at a sub-pixel level in a hyperspectral scene. It consists of the fact that many pixels in the scene are mixed in nature, i.e. they are formed by different spectral constituents at sub-pixel levels. The main approach for dealing with the mixture problem in the literature has been linear spectral unmixing, which assumes that the incident radiation interacts linearly with the material residing inside a pixel and, hence, the response obtained at the sensor can be modelled as a linear combination of a set of pure spectral signatures (called endmembers in hyperspectral unmixing jargon) weighted by their fractional abundances in the pixel. In this regard, one of the main contributions of the present thesis is the integration of spatial and spectral information as a previous step to the traditional endmember identification conducted by many algorithms. We accomplish this through a set of innovative spatial preprocessing modules, intended to guide the endmember identification process by including spatial information but without the need to modify the already available, spectral-based endmember identification algorithms. Furthermore in this thesis work, we develop a new compressive sensing framework for hyperspectral imaging, which exploits the spatial correlation of hyperspectral images and the spectral mixing phenomenon in order to compress the hyperspectral data in the acquisition process. According to our experiments, conducted using both real and synthetic hyperspectral scenes, the newly developed spatial preprocessing techniques can significantly improve the spatial representativeness of the extracted endmembers and reduce the modelling errors in the unmixing step resulting from the use of more spatially consistent endmembers. Similarly, the newly developed compressive sensing algorithms can achieve very high compression ratios without losing spectral quality. In other words, the new techniques resulting from the proposed thesis work allow for a better integration of the spatial and the spectral information contained in hyperspectral image scenes, as illustrated using data sets from a variety of instruments such as the popular NASAs Airborne Visible Infra-Red Imaging Spectrometer (AVIRIS). The simulations with synthetic data sets have been conducted using different noise levels in order to analyse the sensitivity of the proposed techniques

to this parameter, resulting in the conclusion that the inclusion of spatial information can also assist in the hyperspectral imaging analysis when the data to be characterized are noisy, both for unmixing and compressive sensing techniques.

Keyworkds: Hyperspectral imaging, compressive sensing, spectral unmixing, spatial preprocessing.

Acknowledgements

This thesis work has been developed with the support of the Spanish National Program for Research Staff Formation (Programa de Formación de Personal Investigador, FPI). The applicant was awarded with a four years scholarship with reference BES-2009-017737 for the development of this thesis work. The Spanish Ministry of Science and Innovation (Ministerio de Ciencia e Innovación) is gratefully acknowledged for this support. This work also has been supported by the European Community's Marie Curie Research Training Networks Programme under reference MRTN-CT-2006-035927, Hyperspectral Imaging Network (HYPER-I-NET). Finally, we also acknowledge the support provided by the Spanish Ministry of Science and Innovation (HYPERCOMP/EODIX project, reference AYA2008-05965-C04-02) and from Junta de Extremadura (local government) under project PRI09A110. We also acknowledge the support provided by the Spanish Ministry of Science and Innovation (HYPERCOMP/EODIX project, reference AYA2008-05965-C04-02) and from Junta de Extremadura (local government) under project PRI09A110. Finally, we would like to acknowledge the Instituto de Telecomunicaões in Lisbon, (Portugal) which kindly hosted two research stays of 5 and 6 moths respectively, in order to collaborate in the development of this thesis work.

Contents

List of Figures

Table Index

Chapter 1

Motivations and objectives

1.1 Motivations

The work developed in this thesis results from a collaboration between the Hyperspectral Computing Laboratory (HyperComp)[1] research group at the Department of Technology of Computers and Communications, University of Extremadura, Cáceres, Spain, and the Pattern and Image Analysis Group, Instituto de Telecomunicações, Instituto Superior Técnico, Lisbon, Portugal. The thesis represents an effort to improve the analysis and interpretation of remotely sensed hyperspectral images by taking advantage of the complementary nature of spectral and spatial information.

Hyperspectral imaging instruments are now able to characterize the surface of the Earth using hundreds of (narrow) spectral bands, corresponding to different wavelengths. These imaging systems produce enormous data volumes comprising information that is much more detailed than the one provided by more conventional sensor systems such as multispectral imagers, which collect information using a few spectral bands only. One of the main problems associated with hyperspectral imaging is the high dimensionality of these images, which provides at the same time a very fine resolution in the spectral domain. This allows approaching the problem of mixtures happening at sub-pixel levels, which is not possible to address in data sets with more limited spectral resolution such as those collected by multispectral instruments. The possibility to perform accurate sub-pixel analysis of remotely sensed hyperspectral data is very interesting in many applications of high social impact, such as fire detection and monitoring, environment studies, pollutants detection in water and atmosphere, military applications, etc.

Over the last decade, the area of spectral unmixing has been very active. Among the techniques developed, there has been a plethora of algorithms designed to exploit the wealth of spectral information available in remotely sensed hyperspectral data sets. However, a current trend in the literature is the development of techniques which use make synergistic use of both spatial and spectral information. The complementary exploitation of spatial and spectral information allows for a more natural interpretation of the data taking into account both the very fine spectral resolution provided by

[1] http://www.hypercomp.es

hyperspectral instruments and also the fact that natural scenes exhibit spatial correlation that can be exploited in order to improve the analysis.

In this work, we follow the aforementioned direction and further develop several techniques for jointly exploiting spatial and spectral information simultaneously in the analysis of hyperspectral data. Our specific contributions can be summarized as follows:

- One of the main contributions of this thesis is the development of a set of pre-processing techniques which can be combined with classic approaches for spectral unmixing of hyperspectral data (mostly based on spectral information alone). The newly developed pre-processing algorithms include spatial information without the need to modify existing algorithms, thus allowing to tune these approaches for the inclusion of spatial information when considered suitable, thus transforming them from purely spectral approaches to spatial-spectral approaches without the need to modify such algorithms. It is our feeling that the introduction of these pre-processing algorithms covers an important need in the hyperspectral imaging literature, as the inclusion of spatial information in spectral unmixing is a long-desired goal but which can be more or less effective depending on the application context. In this regard, our pre-processing algorithms introduce an (optional) way to perform such integration in a way that is totally controlled by the user, who may decide if the combination of spatial and spectral information is suitable or not for the application at hand. In order to evaluate fairly the newly developed pre-processing techniques, we have performed a detailed assessment of the improvements that can be obtained with regards to using spectral-based techniques alone using a database of synthetic (custom-designed) and real hyperspectral images. Specifically, we have conducted a detailed quantitative and comparative assessment of the results provided by classic techniques for spectral unmixing, with and without the newly developed pre-processing algorithms.

- Another important aspect addressed by this thesis is the extremely large data volumes collected by hyperspectral imaging instruments, which introduces problems in the processing and transmission of hyperspectral data to Earth due to the limited bandwidth of the downlink connection (in comparison with the sheer amount of information to be transmitted). As a result, there is a clear need for (either lossless or lossy) compression of hyperspectral data onboard the imaging instrument. In order to tackle this crucial issue, in this thesis work we also develop a new compressive sensing framework (based on spectral unmixing concepts) which integrates the spatial and the spectral information. As a result, this development can be seen as a natural extension of the idea of integrating spatial and spectral information, explored in the development of pre-processing algorithms, to a new domain in which such integration is used to effectively compress the hyperspectral data and obtain a more compact representation that can be exploited for onboard compression purposes. As in the case of pre-processing algorithms, we conduct a detailed quantitative and comparative assessment of the presented compressive sensing framework using both synthetic and real hyperspectral data sets.

1.2 Objectives

The main objective of this thesis is to investigate the complementarity of spatial and spectral information in hyperspectral image analysis and, more specifically, to explore whether the two sources of information can be combined in order to improve spectral unmixing applications. This is done by presenting and discussing a new set of techniques for spatial pre-processing prior to unmixing and also to perform compressive sensing based on spectral unmixing and spatial information. More specifically, we focus on achieving the following goals:

- To acquire the necessary knowledge about the different algorithms and existing techniques for the analysis and interpretation of remotely sensed hyperspectral scenes, with particular emphasis on spectral unmixing approaches. In this task, we will analyze the advantages and disadvantages of existing approaches and their computational requirements.
- To develop new techniques for spectral unmixing of hyperspectral data which are able to include the spatial information as an optional step in the process, thus exploiting the two sources of information in complementary (and synergistic) fashion in applications in which spatial information can provide added benefits with regards to spectral information.
- To develop new techniques for compressive sensing of remotely sensed hyperspectral data by integrating spectral unmixing concepts and the piecewise smooth nature of real hyperspectral scenes, which allows for the inclusion of spatial information in the design of such algorithms thus providing a natural extension of spatial-spectral unmixing to the task of effectively reducing the dimensionality of hyperspectral data onboard the imaging instrument.
- To perform an exhaustive quantitative and comparative assessment of the newly developed analysis techniques using both synthetic and real hyperspectral scenes widely used in the spectral unmixing community.
- To provide recommendations of best use and practice for the exploitation of the newly developed analysis techniques in different application domains, based on our experience with specific (and highly representative) case sudies that will be extensively analyzed in the present thesis work.

1.3 Thesis organization

The present thesis has been structured in a series of chapters as follows (see Fig. 1.1 for a graphical overview of how these chapters are inter-related):

1. **Motivations and objectives**. In the present chapter, we describe the main motivations and objectives that have led to the development of the thesis. Here, we also describe how the present document is structured.

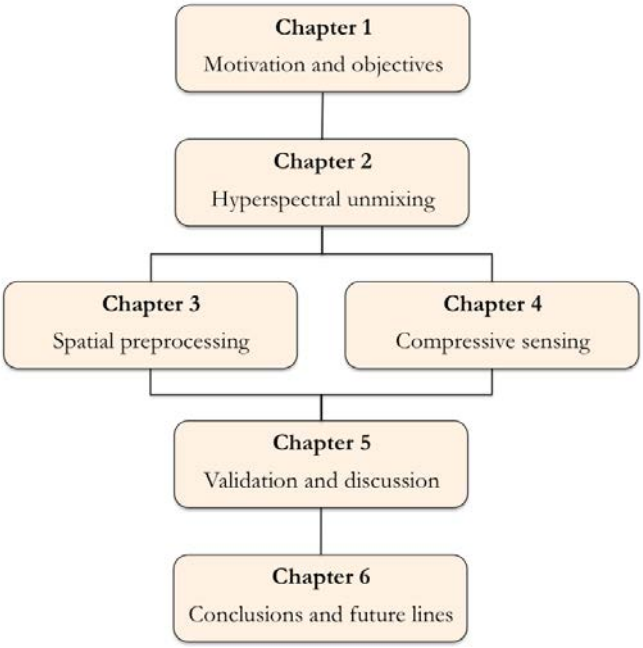

Figure 1.1: Thesis organization.

2. **Hyperspectral unmixing**. In this chapter we introduce the hyperspectral imaging concept and further explain the importance of mixed pixels and their management in hyperspectral data interpretation. The chapter also describes several classic algorithms for spectral unmixing purposes.

3. **Spatial pre-processing**. This chapter describes the newly developed techniques for the purpose of integrating the spatial and the spectral information contained in the data. Specifically, we present three algorithms: spatial pre-processing (SPP), region-based spatial pre-processing (RBSPP) and spatial-spectral pre-processing (SSPP) which use different strategies to achieve the desired integration.

4. **Compressive sensing**. In this chapter we describe a new algorithm for compressive sensing of hyperspectral data which exploits the concepts of spectral unmixing and the integration of spatial and spectral information. The newly developed algorithm is called hyperspectral coded aperture (HYCA). The chapter also describes a variant of this algorithm called constrained HYCA (C-HYCA).

5. **Validation and discussion**. This chapter performs an experimental validation of the newly presented techniques introduced in previous chapters, using both synthetic and real hyperspectral data sets. A joint discussion follows since the developed techniques are strongly related. For instance, the compressive sensing framework is based on the concept of spectral unmixing and on the inclusion of spatial information. As a result, the relationship and best use of the algorithmic contributions presented in this work are extensively discussed in this chapter.

6. **Conclusions and future lines**. This chapter concludes by summarizing the advantages, disadvantages and main contributions of the methods developed in this thesis work, as well as with a presentation of the most plausible future research lines that should be explored after this research.

The thesis concludes with the list of references used during the ellaboration of this document. In an appendix we include the the publications resulting from the present thesis work, together with a statement on the main contributions and relevant aspects which are highlighted for each individual contribution. Specifically, the thesis has resulted in 7 journal citation reports (JCR) papers (one of them submitted and the rest already published), 2 international book chapters, and 18 peer-reviewed conference papers, for a total of 27 international publications.

Chapter 2

Hyperspectral unmixing

In this chapter we describe the fundamental concepts related with hyperspectral imaging and then we specifically focus on the previous research conducted in spectral unmixing. First, we introduce the concept of hyperspectral imaging for Earth remote sensing. Then, we discuss the mixture problem and the techniques existing in the literature to address this problem and perform sub-pixel analysis of hyperspectral scenes. The chapter continues by describing a hyperspectral unmixing chain based on the linear mixture model that will be used as a standard approach for spectral unmixing in this work. For clarity, Table 2.1 summarizes several terms that will be used throughout the chapter, together with their corresponding acronyms.

2.1 The hyperspectral imaging concept

Hyperspectral imaging is an emerging and fast growing area in remote sensing. It is concerned with the measurement, analysis, and interpretation of spectra acquired from a given scene (or specific object) at a short, medium or long distance by an airborne or satellite sensor. The main characteristic of hyperspectral images is the high resolution they present in the spectral domain, since they are collected by instruments able to measure hundreds of *narrow* spectral bands corresponding to continuous wavelength channels [27]. In contrast, multispectral imaging instruments are only able to provide information in a few spectral bands [28]. In fact, hyperspectral imaging instruments have experienced a significant evolution [29]. The very high spectral resolution of remotely sensed hyperspectral data [30], rooted in technological, modeling and processing advances, has fostered a strong interest in this image modality at an unprecedented rate in recent years. In fact, the very high spectral resolution of hyperspectral data offers very significant potential in the identification of materials and their properties [31]. However, the high dimensionality of hyperspectral data (and its usually low spatial resolution) raises a series of new challenges on several fronts, namely, in signal and image processing [32], physical modeling, sensor design and calibration, applications and computationally efficient processing [28].

The wealth of information available from hyperspectral imaging instruments has

Table 2.1: List of acronyms used in this chapter

Acronym	**Term**
AIC	Akaike information criterion [1]
AMEE	Automated morphological endmember extraction [2]
ANC	Abundance non-negativity constraint [3]
ASC	Abundance sum-to-one constraint [4]
AVIRIS	Airbone Visible Infra-Red Imaging Spectrometer [5]
CCA	Convex cone analysis [6]
C-HYCA	Constrained hyperspectral coded aperture
ESA	European Space Agency
FCLSU	Fully constrained spectral unmixing [4]
HYCA	Hyperspectral coded aperture
HYSIME	Hyperspectral subspace identification by minimum error [7]
IEA	Iterative error analysis [8]
JPL	Jet Propulsion Laboratory [5]
MNF	Maximum noise fraction [9]
MVSA	Minimum volume simplex analysis [10]
NAPC	Noise adjusted principal components [11]
NASA	National Aeronautics and Space Administration
NMSE	Normalized mean squared error [7]
MDL	Minimum description length [12, 13]
ORASIS	Optical real-time adaptive spectral identification system [14]
OSP	Orthogonal subspace projections [15]
PCA	Principal component analysis [16]
PPI	Pixel purity index [17]
RBSPP	Region-based spatial pre-processing [18]
RMSE	Root mean squared error [19]
SA	Spectral angle [19]
SISAL	Simplex identification via split augmented Lagrangian [20]
SNR	Signal-to-noise ratio [19]
SPP	Spatial pre-processing [21]
SSPP	Spatial-Spectral pre-processing [22]
SSEE	Spatial-spectral endmember extraction [23]
SVD	Singular vector decomposition [24]
VD	Virtual dimensionality [25]
VCA	Vertex component analysis [26]

opened ground-breaking perspectives in several applications, including environmental modeling and assessment for Earth-based and atmospheric studies, risk/hazard prevention and response including wild land fire tracking, biological threat detection, monitoring of oil spills and other types of chemical contamination, target detection for military and defense/security purposes, and urban planning and management studies, among many others [31]. For instance, NASA's AVIRIS[1] is now able to record the visible and near-infrared spectrum (wavelength region from 400 to 2500 nanometers) of the reflected light of an area 2 to 12 kilometers wide and several kilometers long, using 224 spectral bands. The resulting data volume can be seen as a data cube with two spatial

[1] http://aviris.jpl.nasa.gov

and one spectral dimension (see Figure 2.1). In fact, each pixel can be considered as a high-dimensional vector (see Fig. 2.2) where the values of a pixel comprise its associated spectral signature. The spectral signature is characteristic of each observed object and can be used as a *fingerprint* for identification purposes.

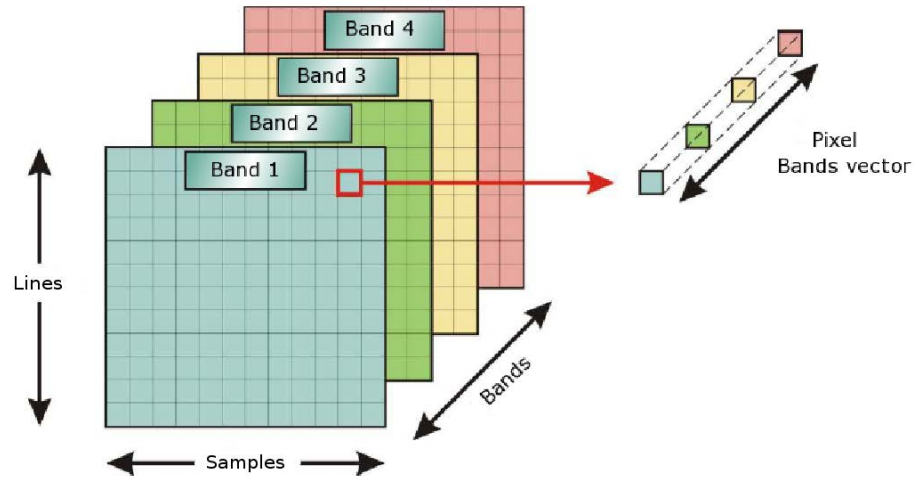

Figure 2.1: Hyperspectral imaging concept

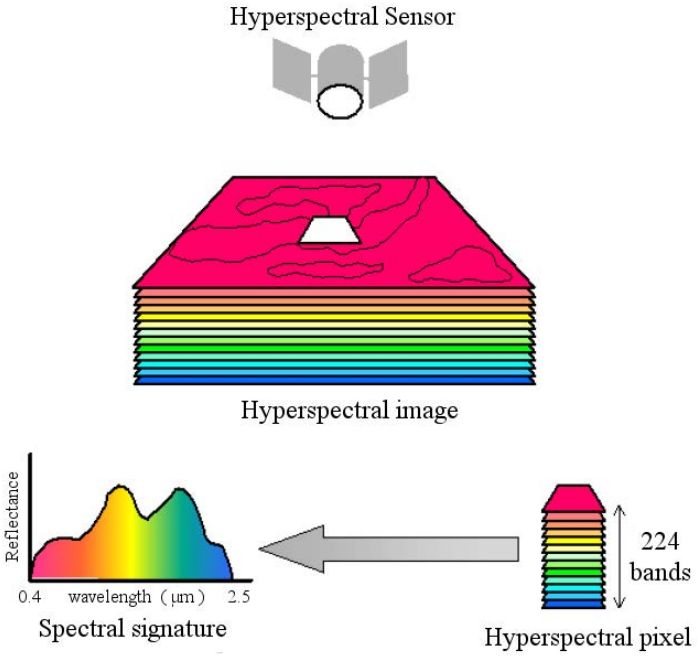

Figure 2.2: Hyperspectral sensor data acquisition.

Although AVIRIS is a widely used platform, it constitutes only one source of hyperspectral data. Table 2.2 summarizes other international Earth observation missions

Table 2.2: Overview of some present and future remote sensing missions including hyperspectral sensors.

	Hyperion[*]	**Prisma**[†]	**EnMAP**[‡]	**HyspIRI**[§]
Country of origin	USA	Italy	Germany	USA
Spatial Resolution	30 meters	5-30 meters	30 meters	60 meters
Revisit Time	16 days	3/7 days	4 days	18 days
Spectral Range	400-2500 nm	400-2500 nm	420-2450 nm	380-2500 nm
Spectral Resolution	10 nm	10 nm	6.5-10 nm	10 nm
Swath width	7.7 km	30 km	30 km	120 km
Earth coverage	Partial	Full	Full	Full
Launch	2000	2014	2014	2018
Lifetime	10 years	$\approx$ 6 years	$\approx$ 6 years	$\approx$ 6 years

[*]http://eo1.gsfc.nasa.gov [†]http://www.asi.it/en/flash_en/observing/prisma [‡]http://www.enmap.org [§]http://hyspiri.jpl.nasa.gov

with hyperspectral sensors already launched or to be launched in the near future. While in this work our focus is on remote sensing applications, hyperspectral sensors have been widely used in many other areas. For instance, hyperspectral cameras are now routinely used for industrial quality control, food inspection, forensics and medical imaging purposes. Hyperspectral microscopes are also gaining popularity in applications such as nanotoxicology, chemometrics and drug discovery.

The number and variety of processing tasks in hyperspectral remote sensing is enormous [33]. However, the majority of algorithms can be organized according to the following specific tasks [34]:

- *Dimensionality reduction* consists of reducing the dimensionality of the input hyperspectral scene in order to facilitate subsequent processing tasks.
- *Target and anomaly detection* consist of searching the pixels of a hyperspectral data cube for "rare" (either known or unknown) spectral signatures.
- *Change detection* consists of finding the "significant" (i.e., important to the user) changes between two hyperspectral scenes of the same geographic region.
- *Classification* consists of assigning a label (class) to each pixel of a hyperspectral data cube.
- *Spectral unmixing* consists of estimating the fraction of the pixel area covered by each material present in the scene.
- *Compression* consists of reducing the size of the hyperspectral image without losing the relevant information that is needed in order to extract information from the scene.

In the following section we explore the problem of spectral unmixing and summarize the most commonly used solutions available in the literature in order to unmix hyperspectral images.

2.2 Spectral unmixing of hyperspectral data

Spectral unmixing has been an alluring exploitation goal since the earliest days of hyperspectral image and signal processing [35, 36, 37, 38]. No matter the spatial resolution, the spectral signatures collected in natural environments are invariably a mixture of the signatures of the various materials found within the spatial extent of the ground instantaneous field view of the imaging instrument. For instance, the pixel vector labeled as "vegetation" in Figure 2.3 may actually comprise a mixture of vegetation and soil, or different types of soil and vegetation canopies. In this case, several spectrally pure signatures (called *endmembers* in hyperspectral imaging terminology) are combined into the same (mixed) pixel. The availability of hyperspectral imagers with a number of spectral bands that exceeds the number of spectral mixture components [39] has allowed to cast the unmixing problem in terms of an over-determined system of equations in which, given a set of *endmembers*, the actual unmixing to determine apparent abundance fractions can be defined in terms of a numerical inversion process [17].

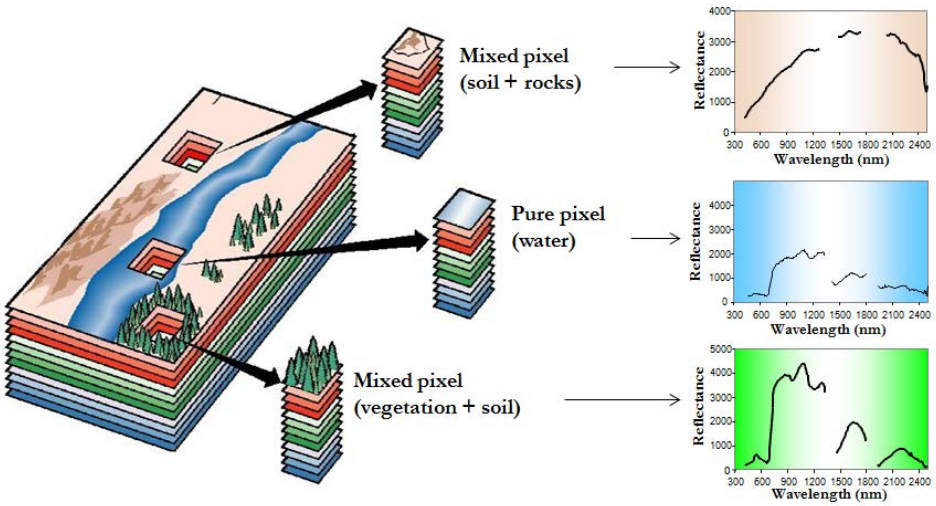

Figure 2.3: Mixed pixels in hyperspectral imaging.

A standard technique for spectral mixture analysis is *linear* spectral unmixing [40, 41, 42], which assumes that the collected spectra at the spectrometer can be expressed in the form of a linear combination of endmembers weighted by their corresponding abundances. It should be noted that the linear mixture model assumes minimal secondary reflections and/or multiple scattering effects in the data collection procedure, and hence the measured spectra can be expressed as a linear combination of the spectral signatures of materials present in the mixed pixel [see Fig. 2.4(a)]. Although the linear model has practical advantages such as ease of implementation and flexibility in different applications [43], *nonlinear* spectral unmixing may best characterize the resultant mixed spectra for certain endmember distributions, such as those in which the endmember components are randomly distributed throughout the field of view of the instrument

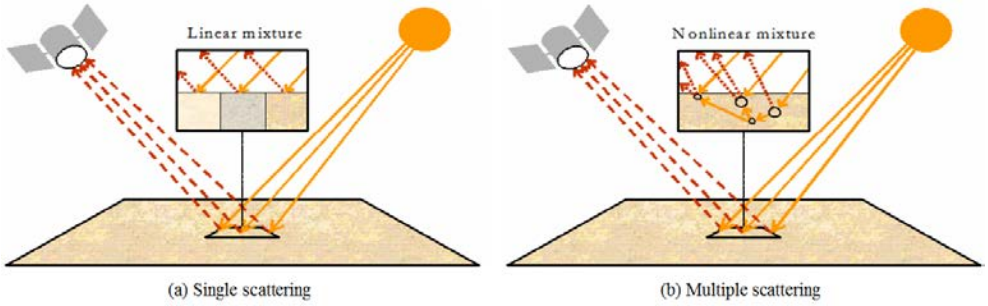

Figure 2.4: Linear versus nonlinear mixture models: single versus multiple scattering.

[44, 45]. In those cases, the mixed spectra collected at the imaging instrument is better described by assuming that part of the source radiation is multiply scattered before being collected at the sensor [see Fig. 2.4(b)]. In this case, interactions can be at a *classical*, or *multilayered*, level or at a *microscopic*, or *intimate*, level. Mixing at the classical level occurs when light is scattered from one or more objects, is reflected off additional objects, and eventually is measured by hyperspectral imager. A nice illustrative derivation of a multilayer model is given by Borel and Gerstl [46] who show that the model results in an infinite sequence of powers of products of reflectances. Generally, however, the first order terms are sufficient and this leads to the bilinear model. Microscopic mixing occurs when two materials are homogeneously mixed [47]. In this case, the interactions consist of photons emitted from molecules of one material are absorbed by molecules of another material, which may in turn emit more photons. The mixing is modeled by Hapke as occurring at the *albedo* level and not at the reflectance level. The apparent albedo of the mixture is a linear average of the albedos of the individual substances but the reflectance is a nonlinear function of albedo, thus leading to a different type of nonlinear model.

In the following, we focus on describing recent advances in the linear spectral unmixing domain. The reason is that, despite its simplicity, it is an acceptable approximation of the light scattering mechanisms in many real scenarios. Furthermore, in contrast to nonlinear mixing, the linear mixing model is the basis of a plethora of unmixing models and algorithms spanning back at least 25 years. A sampling can be found in [48, 42, 49, 50, 51, 52, 53, 54, 55, 56, 57, 58, 59, 60, 61], see also [35] and references therein. As shown in Fig. 2.4(a), the linear mixture model assumes that mixed pixels are a linear combination of the endmembers. This scenario holds when the mixing scale is macroscopic [62] and the incident light interacts with just one material, as is the case in checkerboard type scenes [63, 64]. In this case, the mixing occurs within the instrument itself. It is due to the fact that the resolution of the instrument is not fine enough. The light from the materials, although almost completely separated, is mixed within the measuring instrument.

In order to define the linear mixture model in mathematical terms, let us assume that $\mathbf{Y} \in \mathbb{R}^{l \times n}$ is a hyperspectral image with l bands and n pixels. In this case the matrix $\mathbf{Y} = [\mathbf{y}_1, \ldots, \mathbf{y}_n]$ represents a hyperspectral image in a matrix form, in which the columns of the matrix $\mathbf{Y}$ are the spectral signatures of the image pixels $\mathbf{y}_i$, and the rows

of $\mathbf{Y}$ are the bands of the hyperspectral image. Under the linear mixture assumption, we can model the hyperspectral data as follows:

$$\mathbf{Y} = \mathbf{MA} + \mathbf{N}, \tag{2.1}$$

where $\mathbf{M} \in \mathbb{R}^{l \times p}, \mathbf{M} = [\mathbf{m}_1, \ldots, \mathbf{m}_p]$ is a matrix containing endmembers $\mathbf{m}_i$ by columns and $\mathbf{A} \in \mathbb{R}^{p \times n}, \mathbf{A} = [\mathbf{a}_1, \ldots, \mathbf{a}_n]$ contains the abundance fractions $\mathbf{a}_i$ associated to each endmember in each pixel. Finally, $\mathbf{N} \in \mathbb{R}^{l \times n}$ is a matrix which represents the noise introduced in the model by the acquisition process. Usually two constraints are imposed to the abundances fraction in the linear mixture model. The first one is the ANC (see Table 2.1), which enforces to all the abundances fractions to be non-negative [3], *i.e.* $\mathbf{a}_j \geq 0, j = 1, \ldots, p$. The second constraint is the ASC (see Table 2.1) which enforces the abundances of a given pixel to sum one, *i.e.* $\sum_{j=1}^{p} \mathbf{a}_j = 1$. The unmixing process which consider both constraints is called FCLSU (see Table 2.1) [4]. The linear mixture model can be interpreted in graphic fashion by using a scatter plot between two bands or, more generally, between two non-colinear projections of the spectral vectors. For illustrative purposes, Fig. 2.5 provides a simple graphical interpretation in which the endmembers are the most extreme pixels defining a simplex which encloses all the other pixels in the data, so that we can express every pixel inside the simplex as a linear combination of the endmembers. As a result, a key aspect when considering the linear mixture model is the correct identification of the endmembers, which are extreme points in the l-dimensional space.

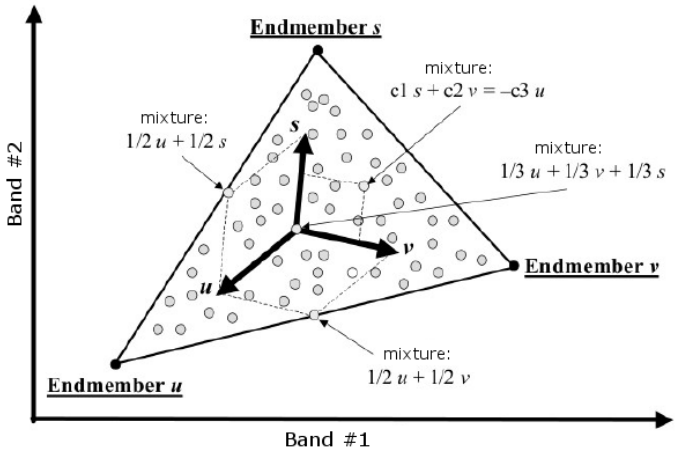

Figure 2.5: Graphical interpretation of the linear mixture model.

The solution of the linear spectral mixture problem described in (2.1) relies on two major requirements:

1. A successful estimation of how many endmembers, p, are present in the input hyperspectral scene $\mathbf{Y}$, and

2. The correct determination of a set $\mathbf{M}$ of p endmembers and their correspondent abundance fractions at each pixel.

In order to address these issues, a standard spectral unmixing chain consisting of three steps is generally applied. In a first step, an (optional) dimensionality reduction step is conducted. This step is strongly connected with the estimation of the number of endmembers present in the hyperspectral scene, p. Once the number of endmembers has been determined, an endmember extraction step identifies the pure spectral signatures present in a scene. Finally, the abundance estimation step requires as input the endmember signatures obtained in the endmember extraction process and produces as output the set of abundance maps associated to each endmember. Fig. 2.6 shows the different steps involved in the processing chain, which are briefly summarized next and described in more detail (discussing specific implementation options for each step) in the following subsections.

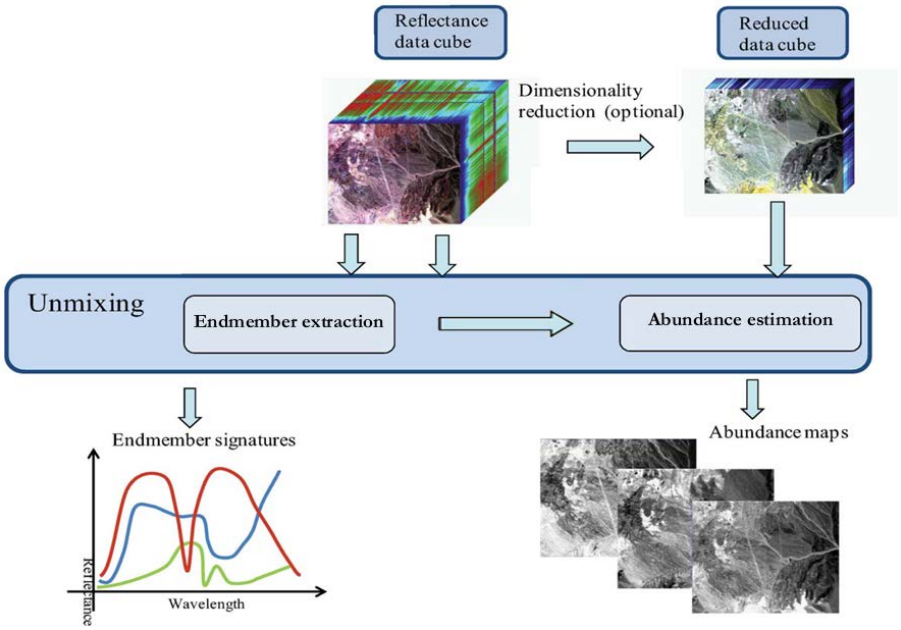

Figure 2.6: Spectral unmixing chain.

1. **Dimensionality reduction**. The dimensionality of the space spanned by spectra from an image is generally much lower than available number of bands. Identifying appropriate subspaces facilitates dimensionality reduction, improving algorithm performance and complexity and data storage. Furthermore, if the linear mixture model is accurate, the signal subspace dimension is one less than equal to the number of endmembers, a crucial figure in hyperspectral unmixing.

2. **Endmember extraction**. This step consists of identifying the endmembers in the scene. *Geometrical* approaches exploit the fact that linearly mixed vectors are in a simplex set or in a positive cone. *Statistical* approaches focus on using

parameter estimation techniques to determine endmembers. Techniques may or may not include spatial information and assume (or not) the presence of pure pixels in the original data set.

3. **Abundance estimation**. Given the the identified endmembers, the abundance estimation step consists of solving a constrained optimization problem which minimizes the residual between the observed spectral vectors and the linear space spanned by the inferred endmembers in order to derive fractional abundances which are, very often, constrained to be nonnegative and to sum to one (*i.e.*, they belong to the probability simplex). There are, however, some hyperspectral unmixing approaches in which the endmember determination and inversion steps are implemented simultaneously.

2.2.1 Dimensionality reduction

The number of endmembers p present in a given scene is, very often, much smaller than the number of bands l. Therefore, assuming that the linear model is a good approximation, spectral vectors lie in or very close to a low-dimensional linear subspace. The identification of this subspace enables low-dimensional yet accurate representation of spectral vectors. It is usually advantageous and sometimes necessary to operate on data represented in the signal subspace. Therefore, a signal subspace identification algorithm is often required as a first processing step in the spectral unmixing chain. Unsupervised subspace identification has been approached in many ways. Projection techniques seek for the best subspaces to represent data by optimizing objective functions. For example, PCA maximizes the signal variance; SVD maximizes power; MNF and NAPC minimize the ratio of noise power to signal power. NAPC is mathematically equivalent to MNF [11] and can be interpreted as a sequence of two principal component transforms: the first applies to the noise and the second applies to the transformed data set.

The identification of the signal subspace is a model order inference problem to which information theoretic criteria like the MDL or the AIC come to mind. These criteria have in fact been used in hyperspectral applications [65] adopting the approach introduced by Wax and Kailath in [66]. In turn, Harsanyi, Farrand, and Chang [67] developed a Neyman-Pearson detection theory-based thresholding method to determine the number of spectral endmembers in hyperspectral data, referred to as VD. This method is based on a detector built on the eigenvalues of the sample correlation and covariance matrices. A modified version includes a noise-whitening step [65]. HYSIME adopts a minimum mean squared error based approach to infer the signal subspace. The method is eigendecomposition based, unsupervised, and fully-automatic (*i.e.*, it does not depend on any tuning parameters). It first estimates the signal and noise correlation matrices and then selects the subset of eigenvalues that best represents the signal subspace in the least square error sense.

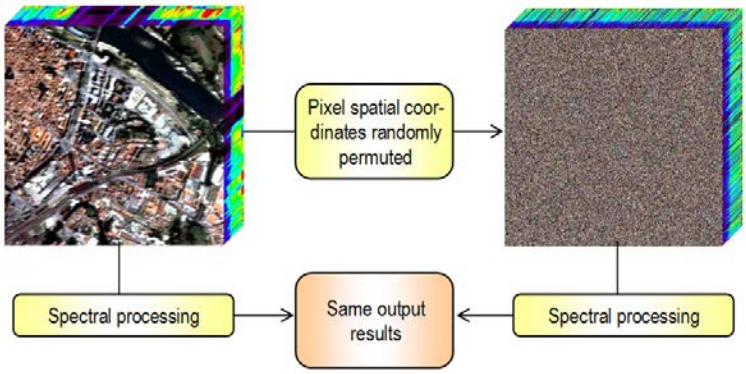

Figure 2.7: Example illustrating the importance of spatial information in hyperspectral analysis.

2.2.2 Endmember extraction

Over the last decade, several algorithms have been developed for automatic or semi-automatic extraction of spectral endmembers by assuming the presence of pure pixels in the hyperspectral data [41]. Classic techniques include the PPI, N-FINDR, IEA, ORASIS, CCA, VCA, and OSP (see Table 2.1). Other advanced techniques for endmember extraction have been recently proposed [68, 69, 70, 71, 72, 73, 74, 75], but none of them considers spatial adjacency. However, one of the distinguishing properties of hyperspectral data is the multivariate information coupled with a two-dimensional (pictorial) representation amenable to image interpretation. Subsequently, most endmember extraction algorithms listed above could benefit from an integrated framework in which both the spectral information and the spatial arrangement of pixel vectors are taken into account. An example of this situation is given in Fig. 2.7, in which a hyperspectral data cube collected over an urban area (high spatial correlation) is modified by randomly permuting the spatial coordinates of the pixel vectors, thus removing the spatial correlation. In both scenes, the application of a spectral-based endmember extraction method would yield the same analysis results while it is clear that a spatial-spectral technique could incorporate the spatial information present in the original scene into the endmember searching process.

To the best of our knowledge, only a few attempts exist in the literature aimed at including the spatial information in the process of extracting spectral endmembers. Extended morphological operations [76] have been used as a baseline to develop the AMEE algorithm for spatial-spectral endmember extraction. Also, spatial averaging of spectrally similar endmember candidates found via SVD was used in the development of the SSEE algorithm. In the following, we describe in more detail three selected spectral-based algorithms (N-FINDR, OSP and VCA) and two spatial-spectral endmember extraction algorithms (AMEE and SSEE) that will be used in our comparisons in this thesis. The reasons for our selection are: 1) these algorithms are representative of the class of convex geometry-based and spatial processing-based techniques which have been successful in endmember extraction; 2) they are fully automated; 3) they always produce

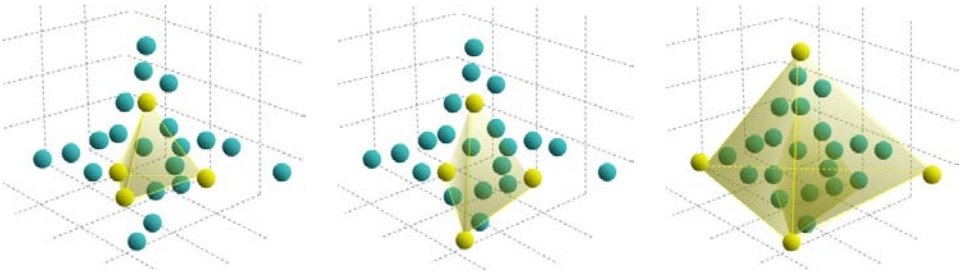

(a) Initialization (b) Replacement (c) Final result

Figure 2.8: Graphical representation of the N-FINDR algorithm.

the same final results for the same input parameters; and 4) the number of endmembers to be extracted, p, is an input parameter for all algorithms, while the AMEE and SSE have additional input parameters related with the definition of spatial context around each pixel in the scene. This section concludes with a description of algorithms that, as opposed to the previously mentioned ones, do not assume the presence of pure pixels in the hyperspectral data. Techniques in this category comprise MVSA and SISAL.

2.2.2.1 N-FINDR

This algorithm looks for the set of pixels with the largest possible volume by *inflating* a simplex inside the data. The procedure begins with a random initial selection of pixels [see Fig. 2.8(a)]. Every pixel in the image must be evaluated in order to refine the estimate of endmembers, looking for the set of pixels that maximizes the volume of the simplex defined by selected endmembers. The volume of simplex is calculated with every pixel in place of each endmember. The corresponding volume is calculated for every pixel in each endmember position by replacing that endmember and finding the resulting volume [see Fig. 2.8(b)]. If the replacement results in a an increase of volume, the pixel replaces the endmember. This procedure is repeated until there are no more endmember replacements [see Fig. 2.8(c)]. The mathematical definition of the volume of a simplex formed by a set of endmember candidates is proportional to the determinant of the set augmented by a row of ones. The determinant is only defined in the case where the number of features is $p - 1$, p being the number of desired endmembers [77]. Since in hyperspectral data typically $l \gg p$, a transformation that reduces the dimensionality of the input data, is required. Often, the PCA transform has been used for this purpose, although another widely used alternative that decorrelates the noise in the data is the MNF. A possible shortcoming of this algorithm is that different random initializations of N-FINDR may produce different final solutions. In this work, we consider an N-FINDR algorithm implemented in iterative fashion, so that each sequential run was initialized with the previous algorithm solution, until the algorithm converges to a simplex volume that cannot be further maximized.

2.2.2.2 Orthogonal subspace projection (OSP)

This algorithm starts by selecting the pixel vector with maximum length in the scene as the first endmember. Then, it looks for the pixel vector with the maximum absolute projection in the space orthogonal to the space linearly spanned by the initial pixel, and labels that pixel as the second endmember. A third endmember is found by applying an orthogonal subspace projector to the original image [78], where the signature that has the maximum orthogonal projection in the space orthogonal to the space linearly spanned by the first two endmembers. This procedure is repeated until the desired number of endmembers, p, is found [15]. A shortcoming of this algorithm is its sensitivity to noise, since outliers are good candidates to be selected in the iterative process adopted by OSP. The VCA method discussed in the following subsection addresses this issue.

2.2.2.3 Vertex component analysis (VCA)

This algorithm also makes use of the concept of orthogonal subspace projections. However, as opposed to the OSP algorithm described above, the VCA exploits the fact that the endmembers are the vertices of a simplex, and that the affine transformation of a simplex is also a simplex [26]. As a result, VCA models the data using a positive cone, whose projection onto a properly chosen hyperplane is another simplex whose vertices are the final endmembers. After projecting the data onto the selected hyperplane, the VCA projects all image pixels to a random direction and uses the pixel with the largest projection as the first endmember. The other endmembers are identified in sequence by iteratively projecting the data onto a direction orthogonal to the subspace spanned by the endmembers already determined, using a procedure that is quite similar to that used by the OSP. The new endmember is then selected as the pixel corresponding to the extreme projection, and the procedure is repeated until a set of p endmembers is found [26]. For illustrative purposes, Fig. 2.9 shows a toy example depicting an image with three bands and three endmembers. Due to the mixing phenomenon all the data is in the plane $\mathbf{S}$. If we project the data onto that plane we can represent the same data in two dimensions instead of three. Then we can apply the OSP to the projected dataset in order to obtain the endmembers.

A possible shortcoming of the VCA algorithm can be illustrated by the following example: if there are two endmembers with similar spectral signatures and the power of the noise is high, then the subspace identification step could miss one of the two similar endmembers. This problem could be avoided by using spatial information as follows. The idea is that, although the endmembers are very similar in the spectral domain, they may be located in different areas in the spatial domain. As a result, spatial information could help in the distinction of the endmembers. In the following subsections we describe different algorithms which make use of spatial information in order to solve some of these potential problems in the endmember identification process.

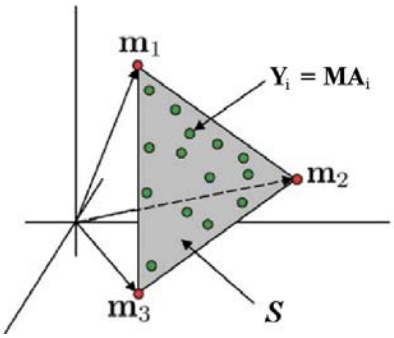

Figure 2.9: Toy example illustrating the impact of subspace projection on endmember identification.

2.2.2.4 Automatic Morphological Endmember Extraction (AMEE)

The automatic morphological endmember extraction (AMEE) [2] algorithm runs on the full data cube with no dimensional reduction, and begins by searching spatial neighborhoods around each pixel vector in the image for the most spectrally pure and mostly highly mixed pixel. This task is performed by using extended mathematical morphology operators [76] of dilation and erosion, which are graphically illustrated on Fig. 2.10. Here, dilation selects the most spectrally pure pixel in a local neighborhood around each pixel vector, while erosion selects the most highly mixed pixel in the same neighborhood. Each spectrally pure pixel is then assigned an *eccentricity* value, which is calculated as the SA [19, 43] between the most spectrally pure and mostly highly mixed pixel for each given spatial neighborhood. This process is repeated iteratively for larger spatial neighborhoods up to a maximum size that is pre-determined. At each iteration the eccentricity values of the selected pixels are updated. The final endmember set is obtained by applying a threshold to the resulting greyscale eccentricity image, which results in a large set of endmember candidates. The final endmembers are extracted after applying the OSP method to the set of candidates in order to derive a final set of spectrally distinct endmembers $\mathbf{M}$, where p is an input parameter to the OSP algorithm.

2.2.2.5 Spatial Spectral Endmember Extraction (SSEE)

The spatial-spectral endmember extraction tool (SSEE) uses spatial constraints to improve the relative spectral contrast of endmember spectra that have minimal unique spectral information, thus improving the potential for these subtle, yet potentially important endmembers, to be selected. With SSEE, the spatial characteristics of image pixels are used to increase the relative spectral contrast between spectrally similar, but spatially independent endmembers. The SSEE algorithm searches an image with a local search window centered around each pixel vector and comprises four steps [23]. First, the singular value decomposition (SVD) transform is applied to determine a set of eigenvectors that describe most of the spectral variance in the window or partition (see Fig. 2.11). Second, the entire image data are projected onto the previously extracted eigenvectors to determine a set of candidate endmember pixels (see Fig. 2.12).

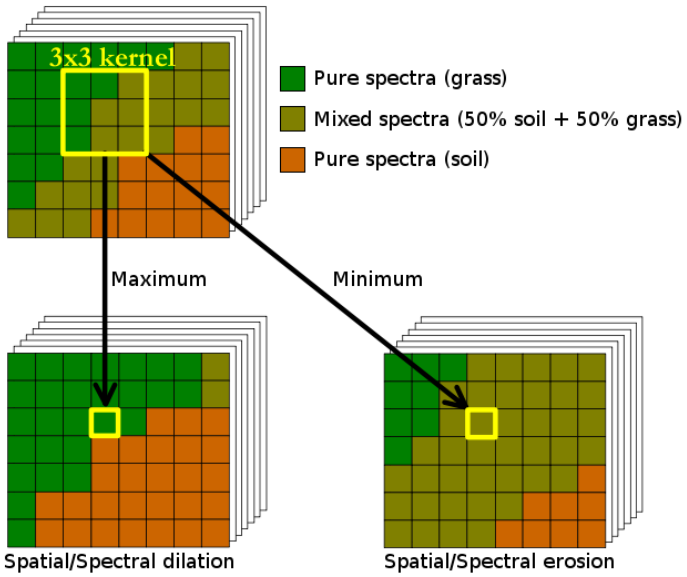

Figure 2.10: Extended morphological operations of erosion and dilation.

Then, spatial constraints are used to combine and average spectrally similar candidate endmember pixels by testing, for each candidate pixel vector, which other pixel vectors are sufficiently similar in spectral sense (see Fig. 2.13). Instead of using a manual procedure as recommended by the authors in [23], we have used the OSP technique in order to derive a final set of spectrally distinct endmembers $\mathbf{M}$, where p is an input parameter to the OSP algorithm.

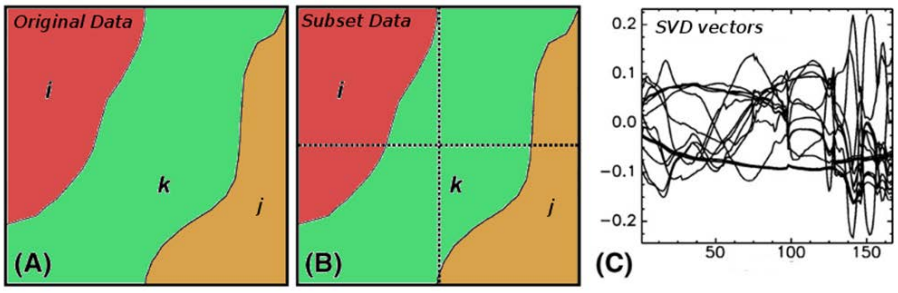

Figure 2.11: First step of the SSEE algorithm. (A) Original data. (B) Subset data after spatial partitioning. (C) Set of representative SVD vectors used to describe spectral variance. (Figure reproduced from [23].)

At this point, it is important to note that SSEE includes spatial information in a different way as AMEE does. The SSEE method uses first a spectral SVD method to extract some candidate endmembers and then includes the spatial information. On the other hand the AMEE combines the spatial and spectral information at the same time using extended morphological operations, and then uses a spectral endmember extraction technique in order to select the final endmember set. In both cases (as it is also the case

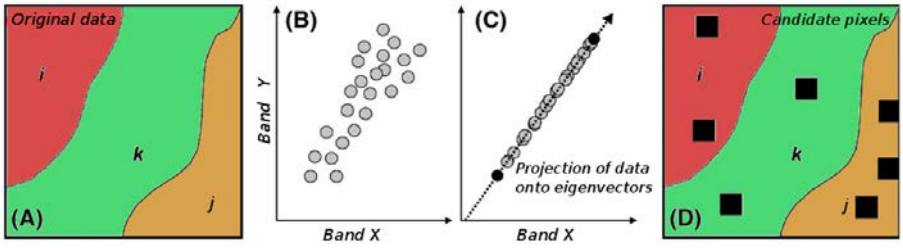

Figure 2.12: Second step of the SSEE algorithm. (A) Original data. (B) Spectral distribution in 2-dimensional space. (C) Projection of data onto eigenvectors. (D) Set of candidate pixels.(Figure reproduced from [23].)

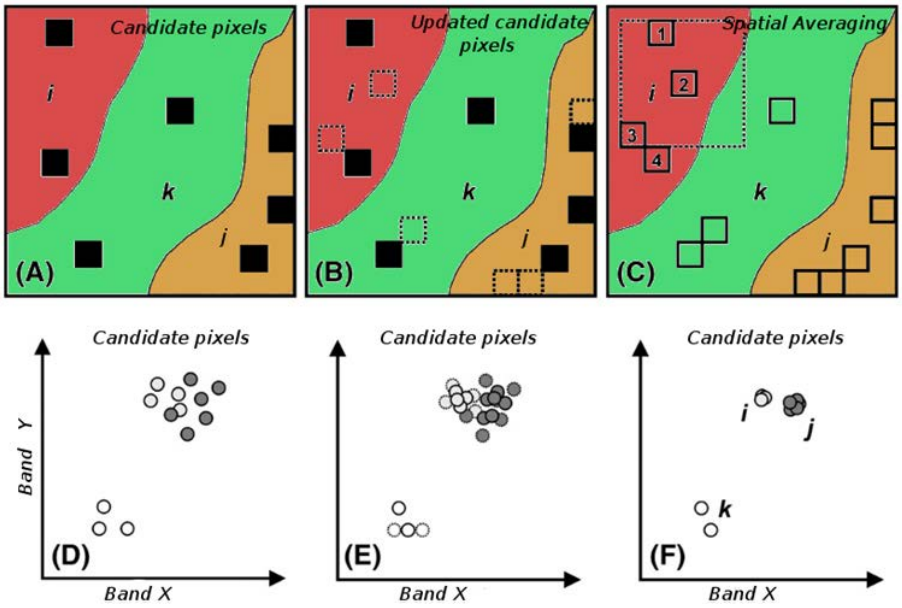

Figure 2.13: Third step of the SSEE algorithm. (A) Set of candidate pixels. (B) Updated candidate pixels after including pixels which are spectrally similar to those in the original set. (C) Spatial averaging process of candidate endmember pixels using a sliding window centered on each candidate. (D) First iteration of spatial-spectral averaging. Averaged pixels shown as thick lines, with original pixels shown as thinner lines. (E) Second iteration of spatial-spectral averaging. (F) Continued iterations compress endmembers into clusters with negligible variance.(Figure reproduced from [23].)

of all endmember identification algorithms discussed thus far) the assumption is that pure spectral signatures are present in the original hyperspectral data. In the following subsection we describe methods which operate under the assumption that pure spectral signatures may not be present at all in the original hyperspectral scene.

2.2.2.6 Algorithms without the pure pixel assumption

This section describes endmember identification techniques which do not operate under the pure pixel assumption [79, 80]. In this case the algorithms do not need the presence

scriptsize

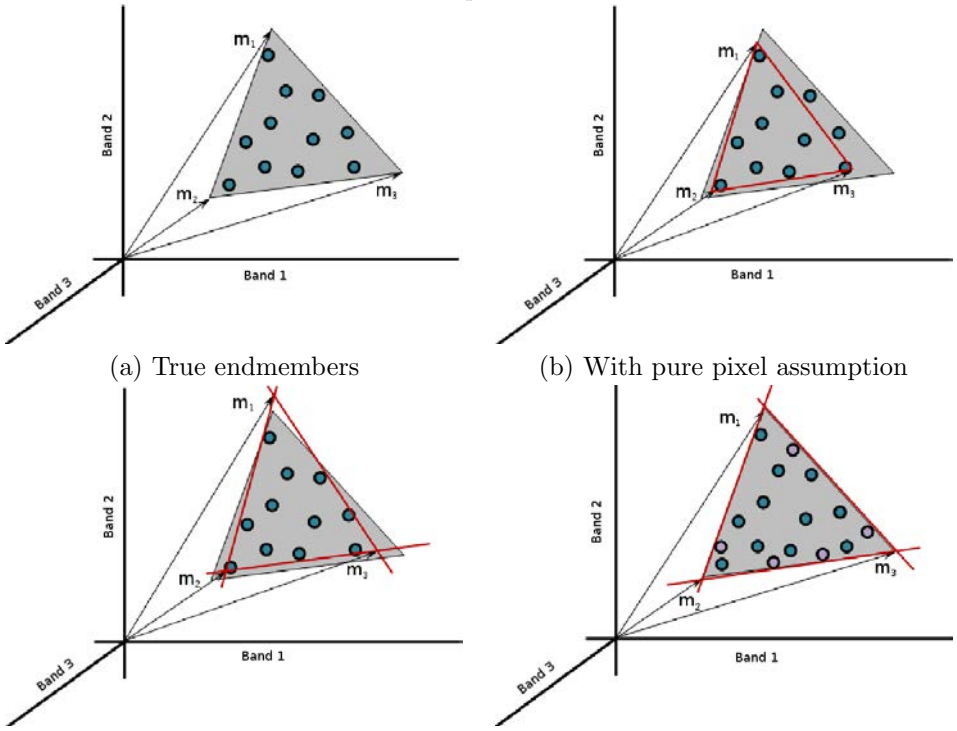

(a) True endmembers (b) With pure pixel assumption

(c) Without pure pixel assumption (d) With pixels at the simplex facets

Figure 2.14: Illustration of different strategies for endmember extraction.

of pure pixels in the dataset in order to generate the endmembers. Fig. 2.14 shows a graphical interpretation of the difference between algorithms that assume and do not assume the presence of pure pixels in the dataset. Specifically, Fig. 2.14(a) represents the true endmembers. In this case, there is no pixel at the simplex vertices so the endmembers are not present in the original data. Fig. 2.14(b) represents a possible solution for an algorithm which does not assume the presence of pure pixels in the dataset. As we can see in Fig. 2.14(b), there are two pixels outside of the simplex, which are outliers in this particular case. Fig. 2.14(c) represents a possible solution of a method which does not assume the presence of pure pixels in the data. In this case, the algorithm tries to estimate a set of endmembers by enclosing the whole dataset. This approach does not guarantee the correct identification of endmembers in the case that the data are highly mixed and there are no pixels in the facets of the simplex. However, if there are pixels in the simplex facets, the true endmembers can be correctly identified even if there are no pixels at the simplex vertex, as depicted in Fig. 2.14(d).

Most of the techniques in this category adopt a minimum volume strategy aimed at finding the endmember matrix $\mathbf{M}$ by minimizing the volume of the simplex defined by its columns and containing the endmembers. This is a non-convex optimization problem much harder than those considered in the previous subsection in which the endmembers are assumed to belong to the input hyperspectral image.

Craig's seminal work [81] established the concepts regarding the algorithms of minimum volume type. Most of these algorithms formulate the endmember estimation as the nonnegative matrix factorization of the mixing and abundance matrices [69, 68, 82, 83, 84, 85], with minimum volume constraint imposed on $\mathbf{M}$. Nonnegative matrix factorization is a hard non-convex optimization prone to get stuck into local minima. Aiming at obtaining lighter algorithms with more desirable convergence properties, the works [10, 20, 86, 87] sidestep the matrix factorization by formulating the endmember estimation as an optimization problem with respect to $\mathbf{Q} = \mathbf{M}^{-1}$. The MVSA and SISAL algorithms implement a robust version of the minimum volume concept. The robustness is introduced by allowing the ANC to be violated. These violations are weighted using a soft constraint given by the hinge loss function ($\text{hinge}(\mathbf{x}) = 0$ if $\mathbf{x} \geq 0$ and $-\mathbf{x}$ if $\mathbf{x} < 0$). After reducing the dimensionality of the input data from l to $p-1$, MVSA/SISAL aim at solving the following optimization problem:

$$\begin{aligned} \widehat{\mathbf{Q}} \quad &= \arg\max_{\mathbf{Q}} \log\left(|\det(\mathbf{Q})|\right) - \lambda 1_p^T \text{hinge}\left(\mathbf{Q}\mathbf{Y}\right) 1_n \\ \text{s.t.:} \quad & 1_p^T \mathbf{Q} = \mathbf{q}_m, \end{aligned} \tag{2.2}$$

where $\mathbf{Q} \equiv \mathbf{M}^{-1}$, $\mathbf{1}_p$ and $\mathbf{1}_n$ are column vectors of ones of sizes p and n, respectively, $\mathbf{q}_m \equiv \mathbf{1}_p^T \mathbf{Y}_p^{-1}$ with $\mathbf{Y}_p$ being any set of linearly independent spectral vectors taken from the hyperspectral data set $\mathbf{Y}$, and λ is a regularization parameter. Here, maximizing $\log(|\det(\mathbf{Q})|)$ is equivalent to minimizing the volume of $\mathbf{M}$.

2.2.3 Abundance estimation

Once a set of endmembers $\mathbf{M}$ have been extracted, their correspondent abundance fractions $\mathbf{A}$ can be estimated (in least squares sense) by the following unconstrained expression [43]:

$$\mathbf{A} \approx (\mathbf{M}^T\mathbf{M})^{-1}\mathbf{M}^T\mathbf{Y}. \tag{2.3}$$

However, it should be noted that the fractional abundance estimations obtained by means of Eq. (2.3) do not satisfy the ASC and ANC constraints. As indicated in [25], a non-negative constrained least squares (NCLS) algorithm can be used to obtain a solution to the ANC-constrained problem in iterative fashion [3]. In order to take care of the ASC constraint, we replace the hard constraint $\mathbf{1}^T\mathbf{A} = 1$ by the soft constraint $\sqrt{\delta}||\mathbf{1}^T\mathbf{A} - 1||_2^2$ added to the quadratic data term $||\mathbf{Y} - \mathbf{M}\mathbf{A}||_2^2$. This is equivalent to use a new endmember signature matrix, denoted by $\mathbf{M}'$, and a modified version of the abundance estimates $\mathbf{A}$, denoted by $\mathbf{A}'$, are introduced as follows:

$$\mathbf{M}' = \begin{bmatrix} \mathbf{M} \\ \delta\mathbf{1}^T \end{bmatrix}, \mathbf{A} = \begin{bmatrix} \mathbf{A} \\ \delta\mathbf{1} \end{bmatrix}, \tag{2.4}$$

where $\mathbf{1} = (\underbrace{1, 1, \cdots, 1}_{p})^T$ and δ controls the impact of the ASC constraint. Using the two expressions in (2.4), a fully constrained estimate can be directly obtained from the NCLS algorithm by replacing $\mathbf{M}$ and $\mathbf{A}$ used in the NCLS algorithm with $\mathbf{M}'$ and $\mathbf{A}'$. Hereinafter, we will refer to the fully constrained (i.e. ASC-constrained and ANC-constrained) linear spectral unmixing model by the acronym FCLSU (see Table 2.1).

Chapter 3

Spatial pre-processing

In the previous chapter we described the mixture problem and also the most important techniques in the literature for linear spectral unmixing. Although there are a few algorithms exploiting the spatial contextual information [83, 88, 89], most of techniques for hyperspectral unmixing just use the spectral information in order to conduct the unmixing process. This means that these techniques consider the hyperspectral data set as a set of unordered spectral signatures. However the pixels in a hyperspectral data set exhibit spatial correlation, and this spatial arrangement. One of the goals of this thesis work is to explore if spatial information could assist in the spectral unmixing process. For instance, one of the problems of traditional endmember extraction techniques is that they look for extreme pixels in the data set, which could also be outliers in real data. These outliers are not representative and often do not qualify as good endmembers. In turn, the selection of endmembers in areas in which there are other similar pixels has the potential to remove the impact of outliers in the endmember identification process. In this chapter, we describe our efforts towards the incorporation of spatial information in spectral unmixing techniques. The remainder of the chapter is organized as follows. First, we provide a more detailed motivation for the inclusion of spatial information in spectral unmixing techniques. Then, we describe three methodologies specifically designed to include spatial information in the form of a pre-processing. This offers the advantage that available techniques for spectral unmixing (e.g., those based on spectral information) do not need to be modified since the inclusion of spatial information comes as an (optional) pre-processing mode that the end-user can decide to use (or not) in combination with classic techniques for spectral unmixing.

3.1 Motivation

As mentioned in the previous chapter of this document, only a few attempts exist in the literature aimed at including the spatial information in the process of extracting spectral endmembers. For instance, previous work has shown that extended morphological operations can effectively integrate spatial and spectral information in the search for endmembers [2], but these operations are sensitive to the shape and size of the

morphological structuring element (spatial window) used as an input parameter to define a spatial context around each pixel vector in the scene [41]. Another approach has recently explored the use of spectral contrast enhancement techniques for averaging spectrally similar endmembers [23]. In both cases, the final endmembers are obtained after a region growing procedure in which spectrally similar endmember candidates, located in the same spatial region, are averaged to produce a single representative signature for each region. Although such procedure generates signatures which can represent bundles of spectrally similar signatures located in the same spatial region, there is a risk that the averaging process conducted inside such region may ultimately degrade the spectral purity of the representative endmember. As a result, there is a need for techniques able to incorporate the spatial information into the endmember search process but which, at the same time, can also satisfy the following desirable features:

1. The incorporation of spatial information should not degrade the spectral quality of the final endmembers; quite opposite, the spatial information may be used as a *guide* to exploit spectral information more effectively.

2. The choice of the size and shape of the spatial context around each pixel vector should not be a critical parameter requiring fine-tuning; ideally, a spatial-spectral endmember extraction algorithm should behave effectively with different spatial window shapes and sizes.

3. Finally, it is highly desirable that the integration of spatial and spectral information does not include significant modifications in the implementation of available endmember extraction algorithms, which are in most cases fully automated in nature.

With the above features in mind, this chapter develops several strategies for the integration of spatial and spectral information in the process of endmember extraction and spectral unmixing. The proposed approaches are presented as preprocessing modules which can be used in combination with available endmember extraction algorithms. The preprocessing takes advantage of a particular characteristic of remotely sensed scenes, in which spatially adjacent pixel vectors are expected to share similar information, from a spectral point of view. Thus, a possible approach to take advantage of such knowledge when searching for image endmembers is to exploit the spatial similarity between adjacent pixels by defining a criterion which is sensitive to the nature of both *homogeneous* and *transition* areas between different land-cover classes. Intuitively, the transition areas between two or more different land-cover types would likely contain some mixed pixels. Conversely, by definition, an endmember is an idealized pure signature for a class [29]. Thus, it would be reasonable to assume that pure pixels are less likely to be found in such transition areas. In other words, our assumption for the development of our preprocessing methods is that it is more likely in practice that such homogeneous areas may be dominated by pure pixels instead of mixed pixels. For instance, in the Fig. 3.1 we can see an example of the real scenario of the Cuprite mining district in Nevada (CA), in which we can clearly see a homogeneous region at the bottom-right which corresponds

to a region dominated by the mineral *montmorillonite* which is and endmember in this scenario. It is clear in this example that the most pure pixel of *montmorillonite* is inside this region. If homogeneous areas can be generally expected to provide best candidate pixel vectors for endmember extraction algorithms, then it is also possible to use the spatial information to intelligently direct the spectral-based endmember search process to these spatially homogeneous regions. In order to accomplish this goal, our approaches rely on the introduction of a spatial-based pixel similarity metric which is used to weight the spectral signature associated to each pixel vector in the scene according to its spatial context.

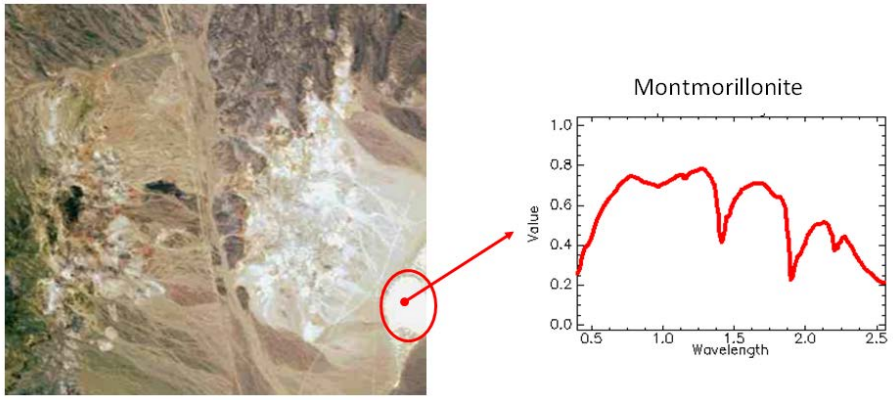

Figure 3.1: Montmorillonite spatially homogeneous region inside the Cuprite mining district.

3.2 Techniques for spatial pre-processing

In this section, we describe three different strategies for inclusion of spatial information in the classic spectral unmixing chain. These methods would be placed right before the endmember identification stage of the chain. For each method we discuss the specific implementation adopted in this work as well as the rationale and expected performance, which will be later illustrated via extensive experiments in this document.

3.2.1 Spatial pre-processing (SPP)

The SPP introduces the spatial information in the endmember extraction process [21], so that the pre-processing can be combined with classic methods for endmember extraction. In this way, the endmembers can be obtained based on spatial and spectral features. Fig. 3.2 shows a flowchart illustrating the different steps involved in the SPP.

The main idea behind the SPP framework is to estimate, for each input pixel vector, a scalar factor ρ which is intimately related to the spatial similarity between the pixel and its spatial neighbors, and then use this scalar factor to spatially weight the spectral information associated to the pixel. Then the spectral information is weighted by this factor. In order to define the SPP method in mathematical terms, we use a formulation

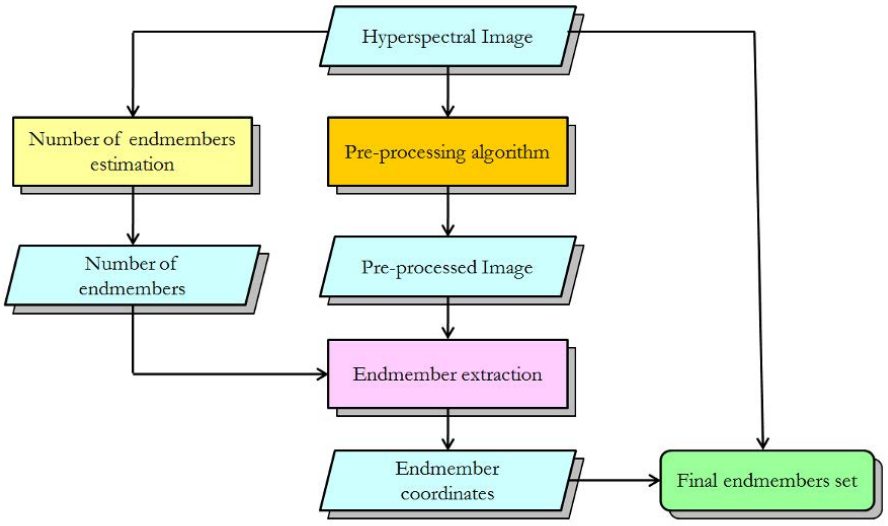

Figure 3.2: Flowchart describing the SPP method.

in which $\mathbf{y}_{i,j}$ represents the pixel in spatial coordinates i, j. Here, we need to introduce the spatial location of the pixel with regards to the previous formulation used in this work. With this notation in mind, the scalar factor is calculated as follows:

$$\alpha(i,j) = \sum_{r=i-d}^{i+d} \sum_{s=j-d}^{j+d} \beta[r-i, s-j] \cdot \gamma[\mathbf{y}_{i,j}, \mathbf{y}_{r,s}], \tag{3.1}$$

where $\mathbf{y}_{i,j}$ is the pixel at spatial coordinates i, j for which we are calculating the scalar factor, and $\mathbf{y}_{r,s}$ are the spatial neighbours. The γ function computes the SA between the pixel and the neighbours and finally the β function computes a weight factor basing on the distance between the pixel and the neighbour. As we can see in (3.2) the closest neighbours are given more relevance. Also the β function is normalized to sum to one as follows:

$$\beta(a,b) \propto \frac{1}{a^2+b^2}. \tag{3.2}$$

Once the scalar factor have been computed, every pixel is displaced to the simplex centroid depending on the scalar factor. The expression (3.3) and (3.4) shows how to displace the image pixels depending on the scalar factor:

$$\rho(i,j) = (1 + \sqrt[2]{\alpha(i,j)})^2 \tag{3.3}$$

$$\mathbf{y}_{i,j}{}' = \frac{1}{\rho(i,j)}(\mathbf{y}_{i,j} - \overline{\mathbf{c}}) + \overline{\mathbf{c}}, \tag{3.4}$$

where $\overline{\mathbf{c}}$ is the simplex centroid, computed as the average of all the image pixels. $\mathbf{y}_{i,j}{}'$ is the new displaced pixel and $\mathbf{y}_{i,j}$ is the original pixel at the coordinates i, j. As we can see

in (3.4), the higher the scalar factor the higher the displacement to the centroid and the lower the scalar factor the lower the displacement to the centroid. As a result, the pixels in homogeneous areas with low scalar factors will be not very displaced to the centroid. On the other hand, the pixels which are different with regards to its neighbours will have a high scalar factor and they will be highly displaced to the simplex centroid so that it is not likely that these will be selected as endmembers in the endmember extraction process.

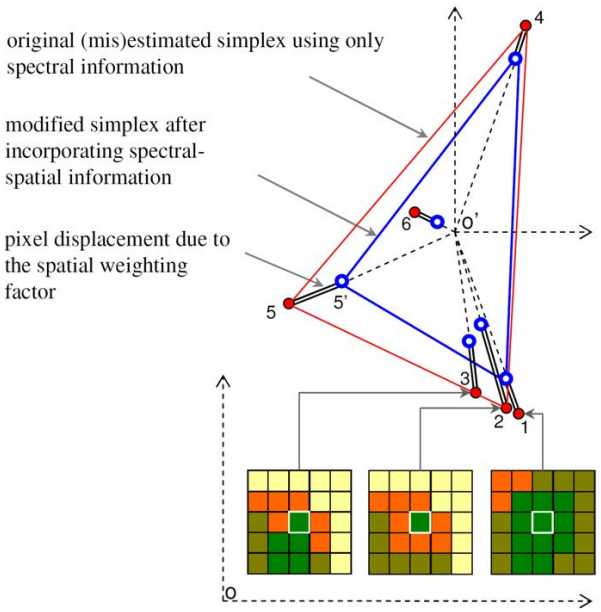

Figure 3.3: Geometric interpretation of the SPP framework.

A simple geometric interpretation of the weighting factor described in (3.3) is illustrated in Fig. 3.3, given as a toy example in which only two spectral bands of an input hyperspectral scene are represented against each other for visualization purposes. As shown by Fig. 3.3, the idea behind the SPP framework is to center each spectral feature in the data cloud around its mean value, and then shift each feature straight towards the centroid of the data cloud (denoted by $\overline{\mathbf{c}}$ in Fig. 3.3) using a spatial-spectral factor given by (3.3). The shift of each spectral feature in the data cloud is proportional to a similarity measure calculated using both the spatial neighborhood around the pixel under consideration and the spectral information associated to the pixel, but without averaging the spectral signature of the pixel. The correction is performed so that pixels located in spatially homogeneous areas (such as the pixel vector labeled as '1' in Fig. 3.3) are expected to have a smaller displacement with regards to their original location in the data cloud than pure pixels surrounded by spectrally distinct substances (e.g., the pixel vector labeled as '3' in Fig. 3.3). Resulting from the above operation, a modified simplex is formed, using not only spectral but also spatial information. It should be noted that the vertices of the modified simplex are more likely to be pure pixels located in spatially homogeneous areas. Although the proposed method is expected to

privilege homogeneous areas for the selection of endmembers, no pixel is excluded from the competitive endmember extraction process that follows the preprocessing. As it can be inferred from Fig. 3.3, the proposed method is also expected to be robust in the presence of outliers.

It is important to notice that the modified simplex in Fig. 3.3 is mainly intended to serve as a guide for a subsequent competitive endmember extraction process, conducted using a user-defined algorithm. However, such modified simplex is not intended to replace the simplex in the input hyperspectral scene. To achieve this, the spatial coordinates of the endmembers extracted from the preprocessed image are retained, but the spectral signatures associated to those spatial coordinates are obtained from the original hyperspectral scene. Then, a spectral unmixing process is conducted using the original hyperspectral image. As a result, no artifacts are introduced in the process of estimating abundance fractions.

Before concluding our description of the SPP framework it is important to emphasize that there are some unresolved issues that may present challenges over time. Prior to addressing some potential limitations of our approach, we first categorize four types of pixels (vectors) that can be found in a hyperspectral scene, along the lines of the definitions given in [29]. A *pure* pixel is a pixel which is made up by a single spectral signature, as opposed to a *mixed* pixel, whose associated spectral signature is given by several different underlying material substances. On the other hand, a *homogeneous* pixel is a pixel whose spectral signature is similar to the signatures of its surrounding pixels and can be considered as the opposite of an anomalous pixel, whose signature is spectrally distinct from the signatures of its neighboring pixels. With the above categories in mind, it is important to note that our preprocessing framework may penalize the selection of anomalous pixels, and increase the probability that an endmember extraction algorithm applied after the preprocessing ends up selecting a majority of pixels which are both pure and homogeneous in nature. As a result, we expect the proposed approach to be less effective in specific tasks such as detection of *small* targets or anomalous areas. Although these areas are not theoretically excluded after the preprocessing, such regions would be more penalized by our proposed spatial-spectral homogeneity criteria. It is also worth noting that, in any event, the term *small* in the previous sentence relates to the size of a processing window that can be controlled and defined in advance by the end-user. A final limitation of the SPP (and of all spatial pre-processing strategies discussed in this work) is that the concept of homogeneous pixel is not necessarily linked to the concept of pure pixel. For instance, there may be homogeneous areas in a scene which are dominated by mixed pixels (for instance, due to the limited spatial resolution available to separate trees equally distributed in a homogeneous background). However, our assumption for the development of the SPP and other pre-processing methods is that it is more likely in practice that such homogeneous areas may be dominated by pure pixels instead of mixed pixels.

3.2.2 Region Based Spatial pre-processing (RBSPP)

In the previous subsection we described the SPP which estimates, for each pixel vector in the scene, a spatially-derived factor that is used to weight the importance of the spectral information associated to each pixel in terms of its spatial context. The SPP relies on a spatial window (of fixed or variable size) which is translated over the spatial domain of the scene in order to analyze contextual information around each image pixel. This strategy is feasible when spectral variation is smooth and relatively constant over the image but, in order to better model natural scenes with step discontinuities and multi-scale features and regions, techniques able to model such regions in spatially-adaptive fashion are needed. For this purpose, in this section we develop a novel region-based spatial preprocessing (RBSPP) [18, 90] strategy which uses spatial information as a *guide* to exploit spectral information more effectively by adequately exploiting spatial context in adaptive fashion. Our proposed approach first adaptively searches for the most spectrally pure regions (understood as groups of several contiguous pixel vectors with similar spectral content) by using a hybrid procedure that combines unsupervised clustering and orthogonal subspace projection concepts. This process is then followed by a spectral-based endmember extraction process conducted using only the pixels located in such regions. In other words, the RBSPP assumes that pure signatures are less likely to be found in transition areas, and more likely to be present in well-defined, spatially homogeneous regions. If we assume that homogeneous areas are more likely to provide good candidate pixel vectors for endmember extraction algorithms, then it is also possible to use spatial information to intelligently direct the spectral-based endmember search process to these regions. However, such regions should also be spectrally pure when compared to others, since there is a possibility that a spatially homogeneous region is also made up of mixed pixels (e.g., a large agricultural field in which the canopy has a small coverage of the soil). In order to accomplish the aforementioned goals, with the aforementioned design principle in mind, our pre-processing approach incorporates the following properties:

1. The inclusion of spatial information is performed in the form of an adaptive and fully automated pre-processing module which uses a region-based approach to reduce the sensitivity of the method to different spatial window shapes and sizes [21, 2, 23].

2. At the pre-processing level, spatial information is used as a guide to exploit spectral information more effectively by directing the endmember searching process to image areas which are both spatially homogeneous and spectrally pure, as opposed to previous developments which mainly accounted for the spatially homogeneous nature of the regions instead of their spectral purity [21].

3. The integration of spatial and spectral information is performed at the pre-processing level and, hence, it does not require any modifications in the endmember extraction stage conducted afterwards. This feature is available in the SPP framework [21] but not in other spatial-spectral developments [2, 23].

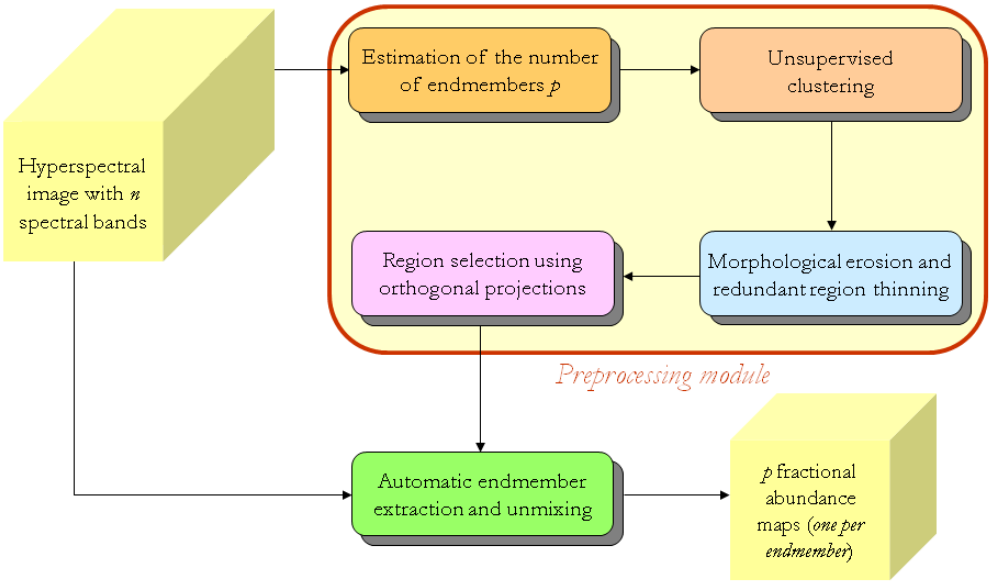

Figure 3.4: Flowchart describing the RBSPP method.

Fig. 3.4 provides a flowchart describing the main stages involved in the RBSPP framework. As shown by Fig. 3.4, the pre-processing consists of several stages which are applied prior to the endmember extraction stage of the standard spectral unmixing chain, and which are intended to provide more spatially relevant endmembers for spectral unmixing purposes. In the following subsections, we describe in more detail the individual stages sequentially applied by the proposed RBSPP method.

3.2.2.1 Estimation of the number of endmembers

Two different methods have been used in this thesis work to estimate the number of endmembers, p, in the original hyperspectral image within the RBSPP framework: the HYSIME method [7], and the VD concept [25]. The former does not have any input parameters, while the latter is a Neyman-Pearson detector based on a prescribed parameter P_F (i.e., false alarm probability). In spite of different criticisms to these methods, these are the two most widely used approaches for estimating the number of endmembers available in the literature. In this thesis work, we have tried to adopt the value of p which results in a consensus for both HYSIME and VD. This is accomplished by first calculating the value of p using the HYSIME method and then calculating the VD with different values of P_F in order to test if this method can reach the same value of p as the one provided by HYSIME. In our experiments, we could always find a consensus between both methods for values of $P_F = 10^{-3}$ or smaller (recommended by the authors), which indicates that the two methods produce similar results.

3.2.2.2 Unsupervised clustering and segmentation

Clustering aims at grouping pixels in feature space, so that pixels belonging to the same cluster are spectrally similar. In this thesis work, we have used three different clustering algorithms within the RBSPP framework:

1. The first one is the ISODATA algorithm [91]. It starts with a random initial partition of the set of available pixel vectors in the original hyperspectral image into g candidate clusters. It then iteratively optimizes this initial partition using least squares [91]. A relevant issue for this algorithm is how to set the number of clusters g in advance. Specifically, in order for the algorithm to automatically determine the value of g, we can define a minimum number of clusters g_{min} and a maximum number of clusters g_{max} based on the information about the considered image (i.e., how many groups of materials with similar spectra are present).

2. The second one is the k-means algorithm [92]. Its goal is to determine a set of g points, called centers, so as to minimize the mean squared distance from each pixel vector to its nearest center. The algorithm is based on the observation that the optimal placement of a center is at the centroid of the associated cluster. It starts with a random initial placement. At each stage, the algorithm moves every center point to the centroid of the set of pixel vectors for which the center is a nearest neighbor according to the euclidean distance [19], and then updates the neighborhood by recomputing the euclidean distance from each pixel vector to its nearest center. These steps are repeated until the algorithm converges to a point that is a minimum for the distortion [92].

3. The third one is the hierarchical segmentation (HSEG) algorithm [93]. It is a segmentation technique based on an iterative hierarchical step-wise optimization region growing method. Furthermore, it allows merging of non-adjacent regions by means of spectral clustering. The algorithm starts by labeling each pixel as a separate region. It then calculates a dissimilarity criterion (in our case, the euclidean distance) between all pairs of spatially adjacent regions. Then it finds the smallest distance value $dist\_val$ and sets $thres\_val$ equal to it, merging all pairs of spatially adjacent regions with $dist\_val = thres\_val$. If a parameter $spectral\_wght > 0$, the algorithm merges all pairs of spatially non-adjacent regions with $dist\_val \leq spectral\_wght \times thres\_val$ and iterates until g clusters are obtained [93]. In order to reduce computational demands, a recursive divide-and-conquer approximation of HSEG (RHSEG) has been used [94].

After the spectral clustering we group the pixels of each cluster in spatially conex regions (using the 8-connectivity criterion), and we remove those regions which size is lower than the mean size of the regions of its cluster. In all cases, the output is a set of spectral clusters, each made up of one or more spatially connected regions. This set can also be seen as a set of e connected regions $\{\mathbf{R}_k\}_{k=1}^{e}$.

3.2.2.3 Region selection using orthogonal projections

The main goal of this stage is to select, out of the set of e regions $\{\mathbf{R}_k\}_{k=1}^{e}$ resulting from the previous stage, a subset of $\{\mathbf{R}_o\}_{o=1}^{p}$ regions which are spectrally distinct, where p is the estimated number of endmembers, with $e \geq p$. For this purpose, we first select a representative spectral signature for each connected region (in this work, the mean spectrum $\bar{\mathbf{R}}_k$, with $k = 1, 2, \cdots, e$). Then, we apply the OSP algorithm to find a set of p spatially representative regions [95]. For this purpose we follow closely the procedure described in the OSP algorithmic description using $\{\bar{\mathbf{R}}_k\}_{k=1}^{e} \equiv \mathbf{Y}$ as the input data in this case. The procedure is terminated at the iteration p, once a predefined number of p spatially connected regions $\{\mathbf{R}_o\}_{o=1}^{p}$ has been identified from the initial set of e regions $\{\mathbf{R}_k\}_{k=1}^{e}$.

3.2.2.4 Automatic endmember extraction

Once the spatial pre-processing has been completed, a spectral-based endmember extraction algorithm is applied to the set of pixels associated to the p spatially connected regions $\{\mathbf{R}_o\}_{o=1}^{p}$ retained after the pre-processing in order to select p endmembers. At this point, it is important to emphasize that the endmember extraction procedure is conducted using only the pixels in the retained regions. The reason for not conducting the search on the mean spectra $\{\bar{\mathbf{R}}_o\}_{o=1}^{p}$ associated to these regions is that spectral averaging generally reduces endmember signature purity. As a result, we conduct the final endmember search in the original image space, regardless of the fact that spectral averaging was used in the previous step as a mechanism to select representative spectra for spatially connected region. In order to perform automatic endmember extraction from the pixels associated to the retained regions $\{\mathbf{R}_o\}_{o=1}^{p}$, we used classic endmember extraction algorithms such as those described in the previous chapter. To make sure that only one representative endmember is extracted from each of the p regions, every time that the considered algorithm identifies a pixel in a certain region, all the pixels labeled as belonging to the same region are removed from the original scene. As a result, in the next algorithm iteration only the pixels associated to the $p - 1$ remaining clusters will be considered as input to the algorithm. At this point, we reiterate that our spectral-based endmember search is conducted in the original image space (from which the pixels associated to regions that are not sufficiently pure have been removed). The output of this step is a set of p endmembers, which have been intelligently selected taking into account the spatial and the spectral properties of hyperspectral data.

To conclude this subsection, it is important to emphasize that our RBSPP pre-processing framework (as it was already the case with the SPP) is expected to penalize the selection of anomalous pixels (associated to very small connected regions or to non-connected pixels) and increase the probability that an endmember extraction algorithm applied after the pre-processing ends up selecting a majority of pixels which are spatially homogeneous in nature. As a result, we expect the proposed approach to be less effective in specific tasks such as detection of small targets or anomalous areas. While we are perfectly aware of the implications of our design choice (which is mainly intended to

promote the selection of spatially relevant pixels), a possible solution to overcome the possible loss of anomalous endmembers could be the definition of a second filter that looks for single pixels distinct from their surroundings, with both homogeneous (the current implementation) and anomalous regions having increased weight in the search for endmembers. This solution is considered as one of the topics deserving attention in future developments.

3.2.3 Spatial-spectral pre-processing (SSPP)

In the previous section we have described the RBSPP, which uses spatial information as a guide to exploit spectral information more effectively by adequately exploiting spatial context in adaptive fashion. This approach first adaptively searches for the most spectrally pure regions (understood as groups of several contiguous pixel vectors with similar spectral content) by using a hybrid procedure that combines unsupervised clustering and orthogonal subspace projection concepts. Then the method performs unsupervised clustering using the ISODATA algorithm [96], and finally applies the OSP algorithm to the mean spectra of the resulting regions in order to find a set of spatially representative regions with associated spectra which are both spectrally pure and orthogonal between them. In this section, we develop a joint spatial-spectral pre-processing (SSPP) [22, 97] module which integrates spatial and spectral information at the preprocessing level. This pre-proccesing method uses a pixel based aproach instead of the region based approach used in the RBSPP. In the RBSPP we selected entire regions so that, if a pure pixel was located in a non pure region, this pixel was discarded due to the fact that the region was discarded. Furthermore, if a mixed pixel was located in a pure region, the RBSPP would retain this pixel due to the fact that the entire region was selected. With a pixel-based approach we can avoid these problems, so that in a pure region we will just select the pure pixels which are relevant to the analysis, thus discarding the mixed pixels inside this region. Also with the proposed pixel-based approach can select pure pixels located in mixed regions if they are spatially homogeneous with regards to its neighbours. In addition to the aforementioned properties, the SSPP intends also to address issues related with sensitivity to noise observed in both SPP and RBSPP [98]. In other words, we have designed the SSPP so that it is relatively insensitive to the noise present in the data. On the other hand, SSPP performs a spectral-based unsupervised clustering coupled with spectral purity indexing to identify a subset of spatially homogeneous and spectrally pure pixels from the scene. These pixels constitute the new set of endmember candidates. The method is quite efficient in computational terms and its application in combination with an endmember extraction algorithm does not increase the computational complexity of the latter. This is due to the fact that the SSPP module discards those pixels which are not sufficiently homogeneous (in spatial sense) or pure (in spectral sense), thus substantially reducing the pool of candidates that the endmember extraction algorithm needs to evaluate when selecting the endmembers.

Fig. 3.5 shows a flowchart describing the SSPP method. As shown by Fig. 3.5, the method consists of five main stages which are described next.

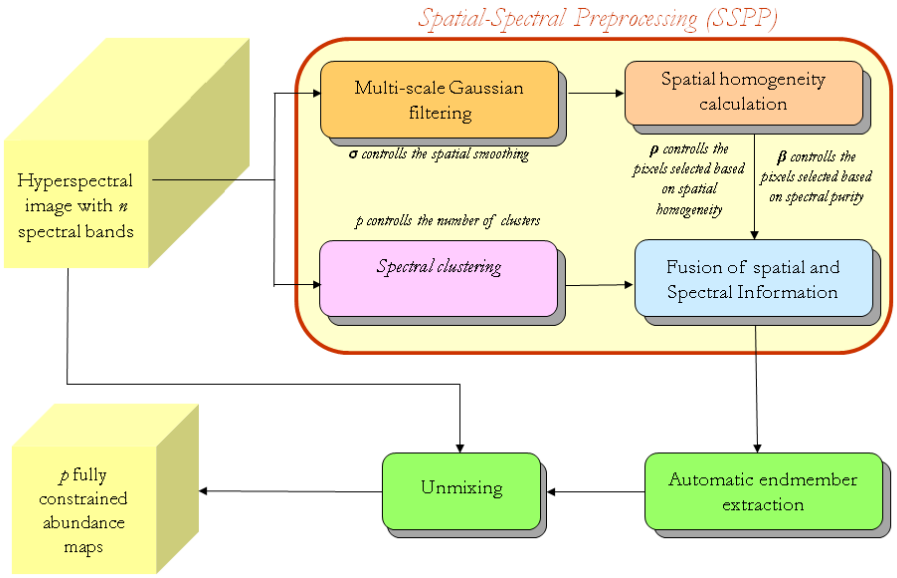

Figure 3.5: Flowchart describing the SSPP method.

3.2.3.1 Multi-scale Gaussian filtering.

This step takes as input the original hyperspectral image $\mathbf{Y}$ and returns a set of filtered hyperspectral images $\{\mathbf{Y}^1, \mathbf{Y}^2, \cdots, \mathbf{Y}^h\}$, where h controls the number of decomposition levels. To perform this step, we first apply Gaussian filtering to each of the l spectral bands of the original hyperspectral image using different values of σ in the Gaussian filter, which results in different filtered versions of the original hyperspectral image $\mathbf{Y}$. Eq. (3.5) shows the pixel-level operation that we apply for performing Gaussian filtering of the k-th spectral band of the hyperspectral image, with $1 \leq k \leq l$:

$$F_k[\mathbf{y}_{i,j}(k)] = \sum_{i'=1}^{r} \sum_{j'=1}^{c} G(i-i', j-j') \cdot \mathbf{y}_{i',j'}(k), \text{ with } G(i', j') = \frac{1}{2\pi\sigma^2} e^{-\frac{i'^2+j'^2}{2\sigma^2}}, \quad (3.5)$$

where $y_{i,j}(k)$ is the reflectance value for the pixel located in the coordinates i, j for the band k. Here, higher σ values lead to more spatial smoothing and the number of σ values considered defines the number of decomposition levels, h. As a result, σ controls the relevance of the spatial context for a given pixel. The lower the σ value, the higher the importance of the closest neighbors. According to our experiments with a variety of hyperspectral scenes, the number of decomposition levels does not need to be very high in order to obtain a good representation of the scene in terms of spatial information (in this thesis work, we always use $h = 3$, with values of $\sigma = \{1.0, 1.5, 2.0\}$).

3.2.3.2 Spatial homogeneity calculation.

This step takes as input the set of h hyperspectral images $\{\mathbf{Y}^1, \mathbf{Y}^2, \cdots, \mathbf{Y}^h\}$ obtained in the previous step and produces a spatial homogeneity index for each pixel in the

original image $\mathbf{Y}$. To perform this step, we first calculate the RMSE [19] between the original hyperspectral image and each of the filtered images $\{\mathbf{Y}^1, \mathbf{Y}^2, \cdots, \mathbf{Y}^h\}$. Eq. (3.6) indicates the pixel-level operation that we use to calculate the RMSE between the pixel $\mathbf{y}_{i,j}$ in the original image and the pixel at the same spatial coordinates $\mathbf{y}'_{i,j}$ in one of the filtered images:

$$\mathrm{RMSE}[\mathbf{y}_{i,j}, \mathbf{y}'_{i,j}] = \left(\frac{1}{l} \sum_{k=1}^{l} \left(\mathbf{y}_{i,j}(k) - \mathbf{y}'_{i,j}(k) \right)^2 \right)^{\frac{1}{2}}. \tag{3.6}$$

In other words, in this step we calculate a set $\{\Delta_1, \Delta_2, \cdots, \Delta_h\}$, where $\Delta_f = \mathrm{RMSE}(\mathbf{Y}, \mathbf{Y}^f)$ and $1 \leq f \leq h$. Note that, the lower the RMSE, the higher the similarity between a pixel in the original image and its neighbours. Quite opposite, the higher the RMSE, the lower the similarity of the pixel in the original image with regards to its neighbours. As a result, the RMSE in Eq. (3.6) can be used as a spatial homogeneity index for each pixel $\mathbf{y}_{i,j}$ in the hyperspectral image $\mathbf{Y}$.

3.2.3.3 Spectral purity index calculation.

For this step we use a PCA-reduced version of the original hyperspectral image. First, we calculate the $p-1$ first components and then calculate the maxima and minima projection values by means of a dot product computation, using the first principal components as the directions for which we identify the pixels with maxima and minima projection values. The pixels with maxima and minima projection are assigned a weight of 1. The weight of the mean value between the maxima and minima projection value is 0. We also apply a threshold value so that the weights lower than θ are assigned the value 0. Finally the spectral purity index will be the sum of all the weights over the first $p-1$ principal components.

3.2.3.4 Spectral clustering.

In parallel to the previous steps, we perform a spectral-based unsupervised clustering of the original hyperspectral image. This step, which is applied in parallel to the first two steps, takes as input the original hyperspectral image $\mathbf{Y}$ and returns a set of clusters in which the original image is partitioned. Here, we used the spectral-based unsupervised ISODATA algorithm [96]. The algorithm is applied to a transformed version of the original image obtained using the PCA [16], where the number of components retained after computing the PCA was set to the number of endmembers in the input data, p, estimated using a consensus between the VD concept [25] and HYSIME [7]. For the ISODATA algorithm, the minimum number of classes was set to p and the maximum number of classes was set to $2p$, which empirically resulted in good results according to our tests (similar results were obtained using the well-known k-means clustering algorithm [96]). Resulting from this step, a number of clusters (comprised between p and $2p$) are identified in the original hyperspectral image $\mathbf{Y}$.

3.2.3.5 Fusion of spatial and spectral information.

This step takes as input the spatial homogeneity index calculated in step 2 and the clusters calculated in step 3, and returns a subset of pixels in the original hyperspectral image $\mathbf{Y}$ which will be used for endmember identification purposes. In fact, this step combines the spatial and the spectral information obtained in the previous steps. For each cluster in the spectral classification map, a subset of spatially homogeneous pixels are selected. Parameter $\rho \in [0, 100]$ defines the percentage of pixels that will be selected per cluster. On the other hand, a subset of spectrally pure pixels are selected for each cluster based on parameter $\beta \in [0, 100]$, which defines the percentage of pixels that will be selected per cluster due to its spectral purity. For selection, pixels are ranked according to increasing values of their spatial homogeneity and spectral purity as calculated in the previous step. The main purpose of ranking pixels is to ultimately select those pixels with are both spatially homogeneous and spectrally pure in nature in the subsequent endmember identification step. Finally we merge the spatial and spectral information selecting those pixels that were selected in both cases.

Finally, endmember extraction can be applied to the pixels retained after the procedure above. The outcome of the process is a set of p endmembers and their corresponding fractional abundance maps (one per endmember). In the following chapters we conduct an experimental validation of the SPP, SSPP and RBSPP methods using synthetic and real hyperspectral data sets. It should be noted that Matlab implementations of all these spatial pre-processing frameworks are available online[1]. These algorithms can be combined with classic endmember extraction algorithms with the pure pixel assumption such as N-FINDR or OSP, which are also available online[2] or VCA[3]. Finally, pre-processing algorithms can also be combined with endmember identification algorithms without the pure pixel assumption [99], such as MVSA[4] and SISAL[5]. These algorithms have been made available online in order to guarantee the repeatability of our obtained results and also to allow interested readers to download the source code of these algorithms for their own experiments. Most importantly, efficient implementations of most of the algorithms and data sets developed in this thesis work are available as open-source implementations (in C++ language) in the form of a tool called HyperMix[6].

[1] http://www.umbc.edu/rssipl/people/aplaza/preprocessing.zip
[2] http://www.umbc.edu/rssipl/people/aplaza/codes.zip
[3] http://www.lx.it.pt/~bioucas/code/demo_vca.zip
[4] http://www.lx.it.pt/~bioucas/code/mvsa_demo.zip
[5] http://www.lx.it.pt/~bioucas/code/sisal_demo.zip
[6] http://www.hypercomp.es/hypermix

Chapter 4

Compressive sensing

In the previous chapter we have seen how spatial information may assist in the spectral unmixing process. In this chapter we illustrate how the spectral unmixing concept and the use of spatial information can also assist with another important problem in hyperspectral imaging: the very large dimensionality of hyperspectral data sets. Due to the extremely large volumes of data collected by imaging spectrometers, hyperspectral data compression has received considerable interest in recent years [100, 101, 102]. Hyperspectral data are usually collected by a satellite or an airbone instrument and sent to a ground station on Earth for subsequent processing. Usually the bandwidth connection between the satellite/airborne platform and the ground station is reduced, which limits the amount of data that can be transmitted. As a result, there is a clear need for (either lossless or lossy) hyperspectral data compression techniques that can be applied onboard the imaging instrument [103, 104, 105]. In this chapter, we develop a new compressive sensing (CS) framework [106, 107] for hyperspectral images, termed hyperspectral coded aperture (HYCA)[108, 109], and its constrained version (called C-HYCA)[110]. The remainder of the chapter is organized as follows: first we briefly introduce the concept of CS and random sampling in the spectral domain. Then we describe a novel CS framework that we have developed for this thesis work in which we use the unmixing concept and also we exploit the rich spatial correlation of the hyperspectral images in order to perform a very accurate image reconstruction. Two versions of the reconstruction algorithm have been developed, in the first version (called HYCA) there is a parameter which have to be tuned by hand which is difficult in real applications due to usually there is not a priori information in order to tune the parameter. As a result, later we propose an unconstrained version (called C-HYCA) which computes all the parameters automatically.

4.1 Compressive Sensing and random sampling in the spectral domain

Contrarily to the conventional compression schemes, which first acquire the full data set and then implements some compressing technique, CS acquires directly the compressed

signal. In fact, CS exploits two main characteristics of hyperspectral images:

1. Due to the mixing phenomenon the hyperspectral vectors belong to a low dimensional subspace.

2. The data cube components display very high correlation in the spatial domain.

These two characteristics lead to the conclusion that the hyperspectral data cubes are compressible, *i.e.,* they admit a representation in a given basis or frame in which most of the coefficients are small, and thus, the data is well approximated with just a small number of large coefficients. Compressibility, or *sparsity*[1], is a necessary condition for success of compressive sensing. In our approach, and having in mind the two aforementioned characteristics, it is possible to represent the spectral vectors on a basis of the signal subspace and model the spatial correlation by promoting small local differences on the images of coefficients by minimizing their total variation [111]. Under the linear mixing model [35], if we use the spectral signatures of the endmembers to represent the spectral vectors, then the representation coefficients are the abundance fractions of the pure materials. In this way, the proposed approach is strongly connected with unmixing. To be more precise, and assuming we use the spectral signatures of the endmembers to represent the spectral vectors, our methodology implements hyperspectral unmixing in addition to hyperspectral compressive sensing. This process is achieved by computing inner products, also termed measurements, between known vectors and the original data. This process is sometimes called "coded aperture" because we can conceive the inner products as the total light that is transmitted trough masks acting on the aperture of the instrument. The single-pixel camera [112] is a paradigmatic illustration of this concept. The number of measurements is usually much smaller than the number of components of the original data (see Fig. 4.1).

In order to define the problem in mathematical terms, let $\mathbf{z} \in \mathbb{R}^m$ denote the CS measurements modeled as

$$\mathbf{z} = H(\mathbf{Y}) + \mathbf{w}, \tag{4.1}$$

where $H : \mathbb{R}^{l \times n} \to \mathbb{R}^m$ is a linear operator which computes m inner products between known m vectors and the elements of $\mathbf{Y}$ and $\mathbf{w}$ models additive perturbation, hereafter termed noise, accounting for, *e.g.*, modeling errors and system noise. Since H is a linear operator, then we have $H(\mathbf{Y}) = \mathbf{H}\mathbf{y}$, where $\mathbf{y} := \text{vec}(\mathbf{Y})$ is the vectorization of matrix $\mathbf{Y}$ by stacking its columns and $\mathbf{H} \in \mathbb{R}^{m \times ln}$ is the matrix representation of the linear operator H.

The objective of CS is to recover $\mathbf{y}$ from $\mathbf{z}$ with $m \ll ln$, in order to have compression in the acquisition. Without any further information, this recovering is impossible even in the absence of noise because the matrix $\mathbf{H}$ is undetermined. If, however, vector $\mathbf{y}$ admits a sparse representation with respect to a given frame $\mathbf{\Phi}$, *i.e.,* $\mathbf{y} = \mathbf{\Phi}\boldsymbol{\theta}$ with $\boldsymbol{\theta}$ sparse, then the solution of the optimization problem

$$\min_{\boldsymbol{\theta}} \|\boldsymbol{\theta}\|_0 \quad \text{subject to: } \|\mathbf{z} - \mathbf{H}\mathbf{\Phi}\boldsymbol{\theta}\| \leq \delta \tag{4.2}$$

[1] A vector is k-sparse is only k of its components are diffract from zero.

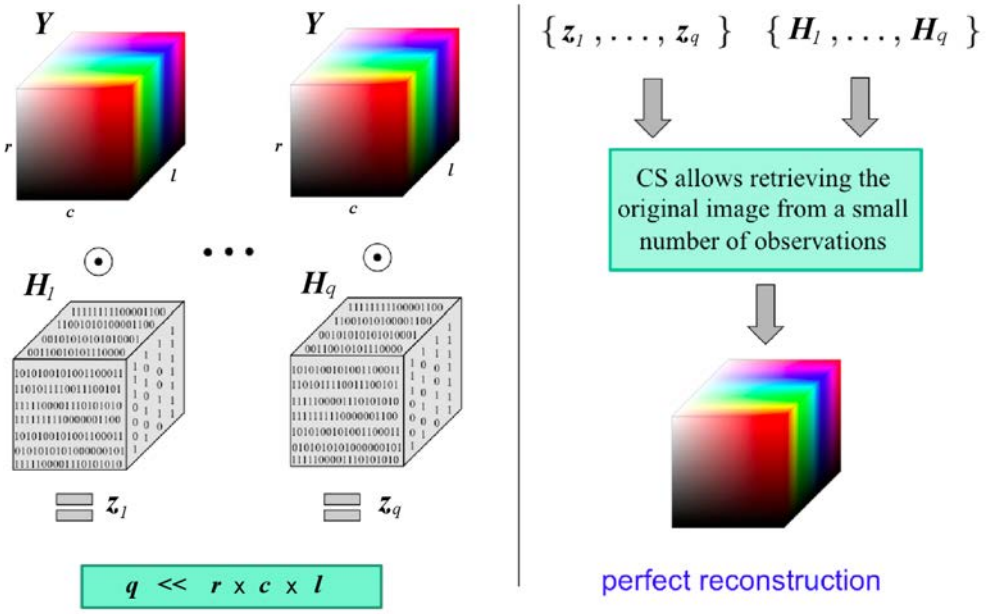

Figure 4.1: Concept of compressive sensing for hyperspectral imaging.

yields, in given conditions, a good approximation for $\mathbf{y}$. In (4.2), the notation $\|\mathbf{y}\|_0$, abusively termed the ℓ_0 norm of $\mathbf{y}$, denotes the number on non-null components of $\mathbf{y}$ and $\delta \geq 0$ is a parameter depending on the "size" of the noise.

For $\delta = 0$, if the system of linear equations $\boldsymbol{z} = \mathbf{H}\boldsymbol{\Phi}\boldsymbol{\theta}$ has a solution satisfying $2\|\boldsymbol{\theta}\|_0 < \text{spark}(\mathbf{H}\boldsymbol{\Phi})$, where where $\text{spark}(\mathbf{H}) \leq \text{rank}(\mathbf{H}) + 1$ is the smallest number of linearly dependent columns of $\mathbf{H}\boldsymbol{\Phi}$, it is necessarily the unique solution of (4.2) [113, 114]. For $\delta > 0$, the concept of uniqueness of the sparsest solution is now replaced with the concept of stability [115, 116, 117]. For example in [116], it is shown that, given a solution vector $\boldsymbol{\theta}$ of the noiseless ($\delta = 0$) problem (4.2), satisfying the sparsity constraint $\|\boldsymbol{\theta}\|_0 < (1/\mu(\mathbf{H}\boldsymbol{\Phi}) + 1)/2$, where $\mu(\mathbf{H}\boldsymbol{\Phi})$ is the mutual coherence of matrix $\mu(\mathbf{H}\boldsymbol{\Phi})$, then $\boldsymbol{\theta}$ is unique and any solution $\boldsymbol{\theta}^\delta$ of (4.2) for a given $\delta > 0$ such that $\|\mathbf{z} - \mathbf{H}\boldsymbol{\Phi}\boldsymbol{\theta}^\delta\| \leq \delta$ satisfies

$$\|\boldsymbol{\theta}^\delta - \boldsymbol{\theta}\|^2 \leq \frac{4\delta^2}{1 - \mu(\mathbf{H}\boldsymbol{\Phi})(2\|\boldsymbol{\theta}\|_0 - 1)}.$$

CS [106, 118] have recently emerged as an important research area in image sensing and processing, both in terms of the hardware and signal processing algorithms [119, 120, 121, 122, 123, 124]. CS has been successfully applied in multidimensional imaging applications, including magnetic resonance [125], projection [126] and diffraction tomography [127], spectral imaging [128] and video [129]. Works [119, 120] introduce two variants of the coded aperture snapshot spectral imager (CASSI). In [119], the measurement of the input scene is equivalent to projective measurement in the spectral domain. The reconstruction algorithm computes an optimal solution to this CS underdetermined problem using an the expectation maximization algorithm combined with a wavelet based denoising technique. In [120] the measurements is a sum over

the wavelength dimension of a mask-modulated and later sheared data cube. The reconstruction algorithm solves an $\ell_2 - \ell_1$ optimization problem to determine the wavelet coefficients of the original data cube.

The CASSI systems take only a single snapshot from which the original hyperspectral is inferred. In most cases, even assuming that the be reconstructed is sparse in some basis or frame, this inference problem is a highly underdetermined and ill-posed inverse problem. Aiming at improving the conditioning of that inverse problem, the paper [122] adopts the linear mixing model and proposes a joint segmentation and reconstruction of the original dual disperser CASSI measurements described in [119]. In addition, the mixing matrix containing the signatures of the spectral endmembers is also estimated.

The paper [121, 124] introduces a methodology with similarities to ours, but with two major differences: our subspace representation is more flexible, in the same that we just need to know a basis for it and not necessarily the mixing matrix, and our measurement matrix acts on the spectral domain, whereas [121] acts on the spatial domain. This has strong implications in the reconstruction algorithm and in the quality of the reconstructions. In [123], the authors reconstruct the hyperspectral data cube by minimizing a convex functional which penalizes both the trace norm and the sum total variation norms of the all image bands. These two regularizers promote, respectively, low-rank and piecewise smoothness on the reconstructed data cube. The measurement matrix acts independently over the channels.

4.2 Hyperspectral coded aperture (HYCA)

In CS the data is compressed in the acquisition process. In the case of hyperspectral imaging the compressed image is then sent to Earth. Later the original image is recovered by taking advantage of the hyperspectral image properties. Here we work under the assumption that we have the original image, due to we need to estimate the endmembers. We note that the application of CS techniques still make sense in this scenario: the sensor acquires the complete image cube and then run a light endmember identification algorithm such as VCA [7] and computes the CS measurements. It should be noted that many current efforts are intended towards the implementation (in real-time) of endmember extraction algorithms onboard the imaging instrument [130, 35]. These efforts support the operability of our proposed approach.

The HYCA algorithm can be briefly summarized as follows. First, we partition the original hyperspectral data cube $\mathbf{Y}$ in the spatial domain into contiguous squares of size $k = ws \times ws$ (see Fig. 4.2). If we order the pixels in a window from 1 to $k = w_s^2$, then for all windows we can collect the spectral vectors in the ith position in matrix $\mathbf{Y}^i$ (one per column). As a result, depending on the size ws of the window, we obtain collection of k sub-sampled versions of the original image. We assume that the original data is partitioned as $\mathbf{Y} := [\mathbf{Y}^1, \mathbf{Y}^2, \cdots, \mathbf{Y}^k]$.

In order to compress the original hyperspectral image, we apply a linear operator $\mathbf{H}$ to $\mathbf{Y}$ obtaining $\mathbf{Z} = \mathbf{H}(\mathbf{Y}) \in \mathbb{R}^{q \times n}$ as follows:

$$\mathbf{Z} = \mathbf{H}(\mathbf{Y}) := [\mathbf{H}^1\mathbf{Y}^1, \cdots, \mathbf{H}^k\mathbf{Y}^k], \tag{4.3}$$

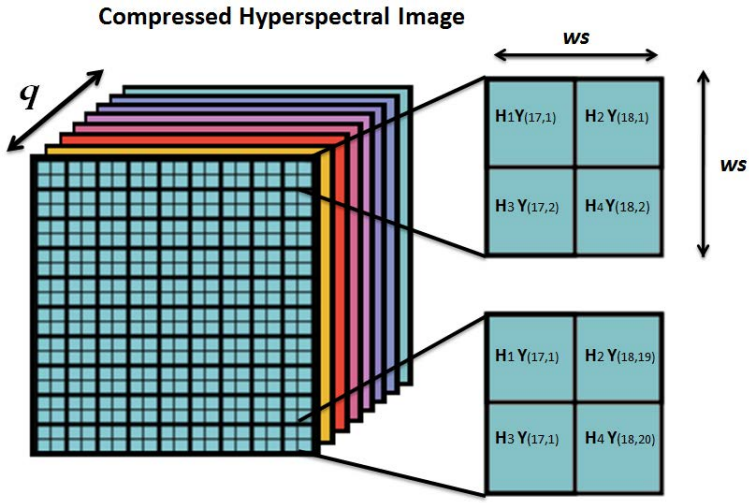

Figure 4.2: Illustration of the proposed strategy for compressive sensing of hyperspectral data.

where $\mathbf{H}^1, \mathbf{H}^2, \ldots, \mathbf{H}^k \in \mathbb{R}^{q \times l}$ are i.i.d. Gaussian random matrices. We have then q measurements per pixel, thus achieving a compression ratio of l/q. Let us now define the linear operator $\mathbf{K}(\mathbf{A}) := \mathbf{H}(\mathbf{MA})$. The HYCA algorithm infers $\mathbf{A}$ by solving the convex optimization

$$\min_{\mathbf{A} \geq 0} \quad \frac{1}{2}||\mathbf{Z} - \mathbf{K}(\mathbf{A})||_F^2 + \lambda_{TV}\mathrm{TV}(\mathbf{A}), \tag{4.4}$$

where $||\mathbf{X}||_F := \sqrt{\mathrm{tr}(\mathbf{X}\mathbf{X}^T)}$ is the Frobenius norm of $\mathbf{X}$ and $\mathrm{TV}(\mathbf{A}) := \sum_{i=1}^{p} \mathrm{TV}(\mathbf{A}_i)$ is the sum of non-isotropic TV [131] of the abundance images $\mathbf{A}_i = \mathbf{A}_{i,:}$, for $i = 1, \ldots, p$. In Eq. (4.4), the first term measures the data misfit and the second term promotes piecewise smooth abundance images. From $\widehat{\mathbf{A}}$, the estimate of $\mathbf{A}$, we infer the original hyperspectral data set by computing $\mathbf{M}\widehat{\mathbf{A}}$. Under the linear mixing model assumption, the hyperspectral vectors belong to a subspace of dimension p. In this case, and if $p \ll l$, what is very often the case, taking CS measurements on the spectral domain is perhaps the best strategy. To shed light into this issue, lets assume that the number of measurements per pixel, q, is no smaller than the number of endmembers, p, and matrices $\mathbf{M}$ and $\mathbf{H}^1, \mathbf{H}^2, \ldots, \mathbf{H}^m$ are full rank. Then the system $\mathbf{Y} = \mathbf{K}(\mathbf{A})$ is determined if $q = p$ or overdetermined if $q > p$), rendering a recovering problem much simpler then the usual underdetermined systems we have in CS. Of course, we are interested in pushing the compression rate to the limits, and thus, we are interested in the underdetermined measurement regime, corresponding to $q < p$.

To solve the problem in Eq. (4.4), we follow closely the methodology introduced in [132]. The core idea is to introduce a set of new variables per regularizer and then use the alternating direction method of multipliers (ADMM, [133] also see appendix A for more details) to solve the resulting constrained optimization problem. By a careful choice of the new variables, the initial problem is converted into a sequence of much simpler

problems. With this in mind, an equivalent way of writing the optimization problem in Eq. (4.4) is:

$$\min_{\mathbf{A}} \frac{1}{2}\|\mathbf{Y} - \mathbf{K}(\mathbf{A})\|_F^2 + \lambda_{TV}\|\mathbf{L}(\mathbf{A})\|_{1,1} + \iota_{R+}(\mathbf{A}), \tag{4.5}$$

where $\mathbf{L}(\mathbf{A}) \equiv [\mathbf{L_h}^T \mathbf{L_v}^T]^T$ is a linear operator computing the horizontal and vertical differences between the components of $\mathbf{A}$ corresponding to neighboring pixels and $\iota_{R+}(\mathbf{A}) = \sum_{i=1}^{n} \iota_{R+}(\mathbf{a}_i)$ is the indicator function ($\mathbf{a}_i$ represents the i-th column of $\mathbf{A}$ and $\iota_{R+}(\mathbf{a}_i)$ is zero if $\mathbf{a}_i$ belongs to the nonnegative orthant and $+\infty$ otherwise). Given the objective function in Eq. (4.5), we write the following equivalent formulation:

$$\begin{aligned} \min_{\mathbf{A},\mathbf{V}_1,\mathbf{V}_2,\mathbf{V}_3,\mathbf{V}_4} \quad & \frac{1}{2}||\mathbf{Y} - \mathbf{K}(\mathbf{V}_1)||_F^2 + \iota_{R+}(\mathbf{V}_2) + \lambda_{TV}||(\mathbf{V}_3, \mathbf{V}_4)||_1 \\ \text{subject to} \quad & \mathbf{A} = \mathbf{V}_1 \\ & \mathbf{A} = \mathbf{V}_2 \\ & \mathbf{L}(\mathbf{A}) = (\mathbf{V}_3, \mathbf{V}_4) \end{aligned} \tag{4.6}$$

To conclude this section note that the λ_{TV} must be tunned by hand, but in practical applications this may be difficult since no reference information is generally available a priori. In the following section we develop a constrained implementaion of the HYCA algorithm (called C-HYCA) which circumvents this problem.

4.3 Constrained HYCA (C-HYCA)

To circumvent the need to tune the regularization parameter λ_{TV} in Eq. (4.4), we herein infer $\mathbf{A}$ by minimizing the following constrained version thereof:

$$\min_{\mathbf{A}\geq 0} \mathrm{TV}(\mathbf{A}) \quad \text{subject to:} \quad \|\mathbf{Z} - \mathbf{K}(\mathbf{A})\|_F^2 \leq \sigma, \tag{4.7}$$

where σ is a scalar value linked to the noise statistics. To solve the problem Eq. (4.7), we also follow closely the C-SALSA methodology introduced in [132] as in the case of HYCA. Let us now define $\iota_{B(\epsilon)}$ as the indicator on a ball of radius ϵ, i.e., $\iota_{B(\epsilon)}(\mathbf{A}) = 0$ if $\|\mathbf{A}\|_F \leq \varepsilon$ and $+\infty$ otherwise. With these definition in place, an equivalent way of writing the optimization problem in Eq. (4.7) is

$$\min_{\mathbf{A}} \|\mathbf{L}(\mathbf{A})\|_{1,1} + \iota_{B(\sigma)}(\mathbf{Z} - \mathbf{K}(\mathbf{A})) + \iota_{R+}(\mathbf{A}). \tag{4.8}$$

Given the objective function in Eq. (4.8), we write the following convex constrained equivalent formulation:

$$\begin{aligned} \min_{\mathbf{A},\mathbf{V}_1,\mathbf{V}_2,\mathbf{V}_3,\mathbf{V}_4} \quad & ||\mathbf{V}_1||_1 + \iota_{B(\sigma)}(\mathbf{V}_2) + \iota_{R+}(\mathbf{V}_4) \\ \text{subject to:} \quad & \mathbf{L}(\mathbf{A}) = \mathbf{V}_1 \\ & \mathbf{A} = \mathbf{V}_2 \\ & \mathbf{Z}\text{-}\mathbf{K}(\mathbf{V}_2) = \mathbf{V}_3 \\ & \mathbf{A} = \mathbf{V}_4, \end{aligned} \tag{4.9}$$

which we solve via ADMM as described in [134] (see appendix A for more details). The minimization of the augmented Lagrangian (see [134] for details) with respect to $\mathbf{A}$ is a quadratic problem with a block cyclic system matrix, thus effectively solved in the Fourier domain. The minimization of the augmented Lagrangian with respect to $\mathbf{V} = (\mathbf{V}_1, \mathbf{V}_2, \mathbf{V}_3, \mathbf{V}_4)$ is decoupled with respect to $\mathbf{V}_1$, $(\mathbf{V}_2, \mathbf{V}_3)$, and $\mathbf{V}_4$. The minimization with respect to $\mathbf{V}_1$ is a componentwise soft-threshold and the the minimization with respect to $\mathbf{V}_4$ is a componentwise projection on the first orthant. The minimization with respect to $(\mathbf{V}_2, \mathbf{V}_3)$ is carried out by a block minimization with respect to $\mathbf{V}_2$ and to $\mathbf{V}_3$. The minimization with respect to $\mathbf{V}_2$ is a quadratic problem involving the inverse of the operator $(\mathbf{I} + \mathbf{K})$ ($\mathbf{I}$ stands for identity operator) which, given the structure of the linear operator $\mathbf{H}$, can be precomputed. Finally, the minimization with respect to $\mathbf{V}_3$ is a projection on a ball of radius σ.

To conclude this section we emphasize that the only parameter involved here is σ which, as mentioned before, is related with the noise statistics and can be estimated automatically. As a result, in this constrained version of the HYCA algorithm all the parameters can be estimated automatically which is indeed the main contribution of the C-HYCA algorithm.

Chapter 5

Validation and discussion

In this chapter we conduct a quantitative and comparative experimental validation of the main innovative contributions of this thesis work introduced in previous chapters: spatial pre-processing prior to spectral unmixing and compressive sensing of hyperspectral data using unmixing concepts and spatial information. The chapter is structured as follows. First, we introduce the quantitative metrics that will be used to carry the experimental validation. Then, we present different data sets used for the experiments. These data comprise both synthetic and real hyperspectral data sets, where the procedure for generating the synthetic data is described in detail in this chapter. Then, we present the results obtained by the innovative appropaches presented in this work with the considered data. The chapter concludes with a discussion on the main observations resulting from the conducted experiments and also on the synergies and innovative aspects introduced by these techniques, which are highly inter-related and can be exploited in combined fashion in a common framework for spectral unmixing and compressive sensing.

5.1 Quantitative metrics

In this section we describe the different metrics and measurements used in order to validate the results provided by the new techniques presented in this thesis work. In order to validate the accuracy of the spectral unmixing process (with and without pre-processing) we use two different metrics: the spectral angle (SA) –intended to evaluate the quality of extracted endmembers– and the root mean square error (RMSE) –intended to evaluate the quality of both the extracted endmembers and the derived fractional abundances–. A variation of this metric, called normalized mean square error (NMSE) is used to evaluate the error in the case of compressive sensing approaches. The use of this metrics and their definition is described in the following three subsections.

5.1.1 Spectral angle (SA)

The SA measures the similarity between two spectral signatures. This metric is used to measure the spectral quality of the endmember extracted with regards to some (possibly available) reference signatures. In the case of synthetic data these reference signatures are

available *de facto*, while in the case of real hyperspectral data the reference signatures may be obtained in optimal conditions (e.g., in the laboratory) by a ground spectro-radiometer, so that these signatures are not affected by atmospheric interferers, non-linear mixtures, geometric corrections, etc. In this regard, it is quite important to use a metric that is as insensitive as possible to these effects. The SA is robust in the presence of illumination interferers. The SA between a reference signature $\mathbf{m}$ and an estimated spectral signature (e.g. an endmmeber) $\hat{\mathbf{m}}$ is given by the expression (5.1). In Eq. (5.1), the $\cdot$ operator represents the dot product between two vectors and $|\cdot|$ operator represents the vector euclidean norm. As mentioned before, we use this metric mainly because it is robust in the multiplication of pixel vectors by constants and, consequently, is invariant before unknown multiplicative scalings that may arise due to differences in illumination and angular orientation. Low SA scores mean high spectral similarity between the compared vectors (the value range of SA is $[0, 90]$ degrees).

$$\mathrm{SA} = \arccos \frac{\mathbf{m} \cdot \hat{\mathbf{m}}}{|\mathbf{m}|\,|\hat{\mathbf{m}}|} \tag{5.1}$$

5.1.2 Root mean square error (RMSE)

A second metric used in this work to evaluate the quality of spectral unmixing results is the RMSE. Low reconstruction errors mean that the pixel is well described as a linear combination of the endmembers and its abundances. However, a high reconstruction error means that the linear combination of the endmembers and the abundances does not properly reconstruct the original hyperspectral scene. This may be caused by a wrong choice of the endmembers, which do not describe the spectral singularity of this pixel as a linear combination of these endmembers, or to an inappropriate estimation of endmember abundances. In the case of real data sets, errors may also arise errors due to the fact that the linear mixture model may not properly characterize nonlinear mixing effects that often happen in the nature. Such nonlinear effects generate model outliers that will result in reconstruction errors, so that the higher the reconstruction error the higher the number of outliers Eq. (5.2) shows how to compute the RMSE between the original and reconstructed image. Since ground-truth fractional abundances are very difficult to be obtained in practice, this metric provides a way to use the original hyperspectral image as a reference for the evaluation.

$$\mathrm{RMSE}(\mathbf{Y}, \hat{\mathbf{Y}}) = \sqrt{\frac{1}{nl} \sum_{i}^{n} ||y_i - \hat{y}_i||^2}. \tag{5.2}$$

5.1.3 Normalized mean square error (NMSE)

A variation of the RMSE called NMSE, which computes the error with regards to the original signal power, is used to evaluate compressive sensing approaches in this work. The main advantage of this metric is that it is independent from the signal power. This metric is appropriate for the assessment of compressive sensing since in this case we are interested in measuring the reconstruction error with regards to the signal power, while

in the case of spectral unmixing we are interested in the error of the spectral unmixing process independently of the original signal power. Eq. (5.3) shows how to compute the NMSE between the original and the reconstructed image. In this expression, the operator $||\cdot||_F^2$, is the squared Frobenious norm of a vector.

$$\text{NMSE} = ||\mathbf{M}(\widehat{\mathbf{A}} - \mathbf{A})||_F^2 / ||\mathbf{MA}||_F^2. \tag{5.3}$$

5.2 Hyperspectral data used in the experiments

In our experiments we have used both synthetic and real hyperspectral datasets. The primary reason for the use of synthetic imagery as a complement to real data analysis is that all details of the simulated images are known. These details can be efficiently investigated because they can be manipulated individually and precisely. As a result, algorithm performance can be examined in a controlled manner. Another reason is that, despite the proliferation of techniques for hyperspectral unmixing and compressive sensing, available algorithms have traditionally not been compared by using a unified scheme. In this regard, one of the contributions of this thesis is the development of a framework and test set for experimental comparison of algorithms, and an assessment of the state of the art for spectral unmixing and compressive sensing by drawing comparisons between substantially different approaches to the problem in rigorous fashion. For instance, the spectral unmixing comparison includes algorithms with and without the pure pixel assumption, and with and without spatial pre-processing, in a way that each method is fairly compared with others on the same common ground. In particular, the inclusion of algorithms without the pure pixel assumption is considered to be very important since the new generation of hyperspectral imaging instruments continue increasing their spectral resolution at the expense of maintaining (or even decreasing) the spatial resolution in the hope of imaging larger portions of the surface of the Earth. In the following we describe the synthetic and real hyperspectral data sets used in our experiments.

5.2.1 Synthetic data

A database of five 100×100-pixel synthetic hyperspectral scenes has been created using fractals to generate distinct spatial patterns. Several natural objects can be approximated by fractals to a certain degree, including clouds, mountain ranges, coastlines, vegetables, etc. thus providing a baseline for simulating spatial patterns often found in nature. In this work, we used fractals to simulate linear mixtures of a set of endmember signatures randomly selected from a spectral library compiled by the U.S. Geological Survey (USGS)[1] and made up of a total of 420 signatures. Fig. 5.1 displays the five fractal images used in the simulations. These images are further divided into a number of clusters using the k-means algorithm [92], where the number of clusters extracted from the five fractal images was always larger than the number of endmember signatures, fixed in our experiments to $p = 9$. The abundance proportions in the regions associated to

[1] http://speclab.cr.usgs.gov/spectral-lib.htm

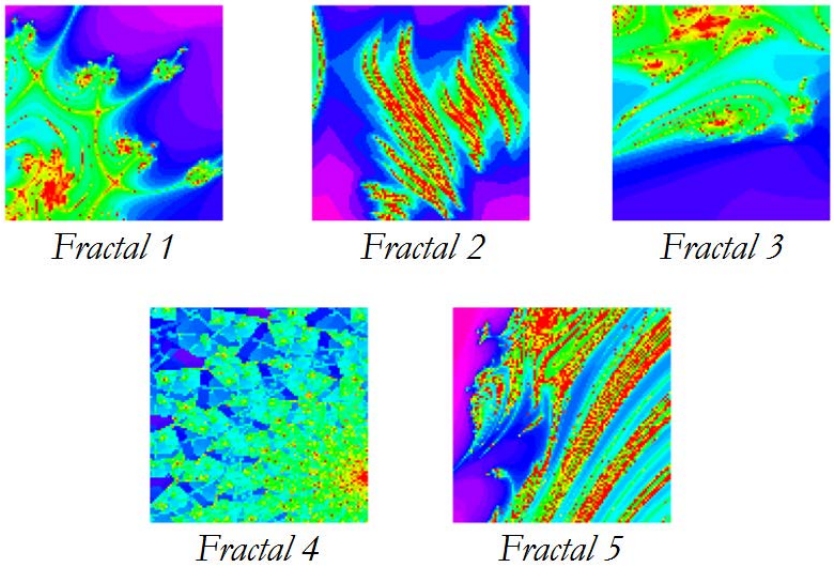

Figure 5.1: Synthetic images used in experiments, where spatial patterns were generated using fractals.

each cluster have been set so that pixels closer to the border of the region are more heavily mixed, while the pixels located at the center of the region are more spectrally pure in nature (the images does not contain any completely pure pixels, a situation often encountered in real-world analysis scenarios, however there are some pixels with a high purity degree). Zero-mean Gaussian noise was added to the synthetic scenes in different signal to noise ratios (SNRs) –from 30 dB to 110 dB – to simulate contributions from ambient and instrumental sources, following the procedure described in [7].

A crucial step in the simulation procedure is how to assign a spectral signature to each cluster. For this purpose, we have implemented an automatic procedure that follows a simple strategy in which the $p = 9$ signatures are first assigned to spatially disjoint regions belonging to different clusters. The remaining regions are then assigned spectral signatures in an automatic way, ensuring that: 1) spatially adjacent clusters always have different signatures associated to them, and 2) there is a balance among the overall number of pixels in the image which are associated to each spectral signature. Inside each region, the abundance proportions of spectral signatures have been generated following a procedure that tries to imitate reality as much as possible, i.e., those pixels closer to the borders of the regions are more heavily mixed, while the pixels located at the center of the regions are more spectrally pure in nature. This is accomplished by linearly mixing the signature associated to each cluster with those associated to neighboring clusters, making sure that the most spectrally pure signature remains at the center of the region while signature purity decreases linearly away from the center to the borders of the regions. For this purpose, a Gaussian filter is applied where the width of the Gaussian is carefully adjusted according to the width of each window. With the aforementioned procedure, which is graphically illustrated by a block diagram in Fig. 5.2, the simulated regions

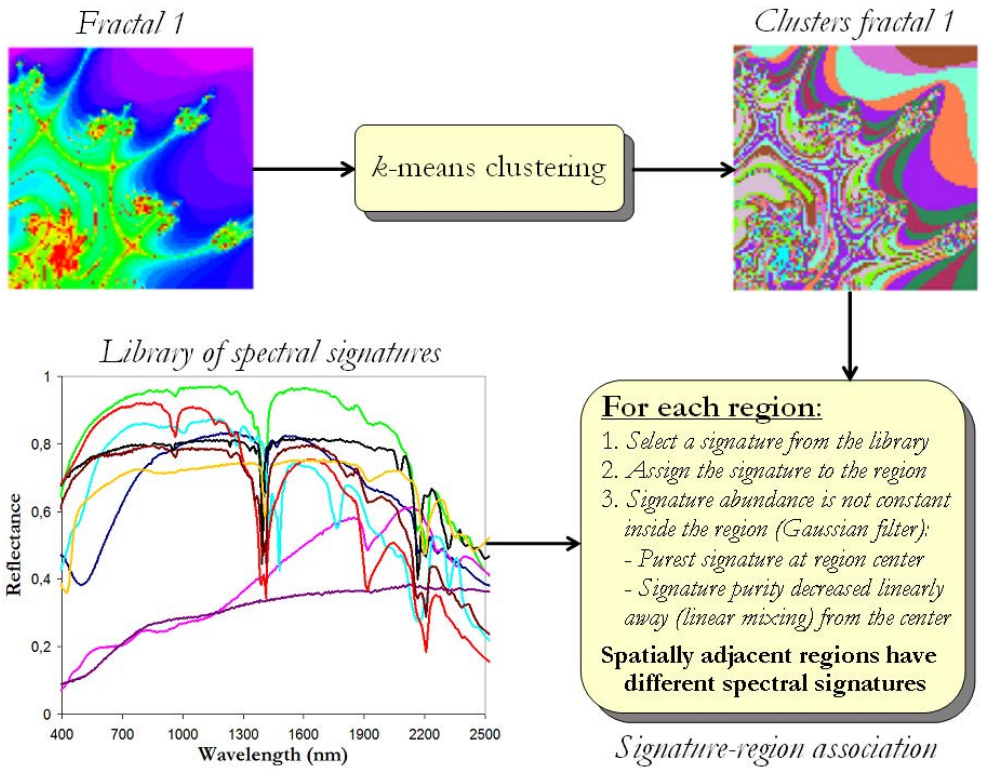

Figure 5.2: Block diagram describing our procedure for generating synthetic hyperspectral images.

exhibit the following properties:

1. All the simulated pixels inside a region are mixed, and the simulated image does not contain completely pure pixels. This increases the complexity of the unmixing problem and simulates the situation often encountered in real-world analysis scenarios, in which completely pure pixels are rarely found.

2. Pixels close to the borders of the region are more heavily mixed than those in the center of the region.

3. If the simulated region is sufficiently large, the pixels located at the center can exhibit a degree of purity of 99% of a certain endmember. However, if the size of the simulated region is small, the degree of purity of pixels at the center of the region can decrease until 95% of a certain endmember, while pixels located in the region borders are generally more heavily mixed.

For illustrative purposes, Fig. 5.3 shows the spectra of the USGS signatures used in the simulation of one of the synthetic scenes (the one labeled as "Fractal 1" in Fig. 5.1). The full database of simulated hyperspectral images is available online[2]. The abundance

[2]http://www.hypercomp.es/hypermix/Downloads

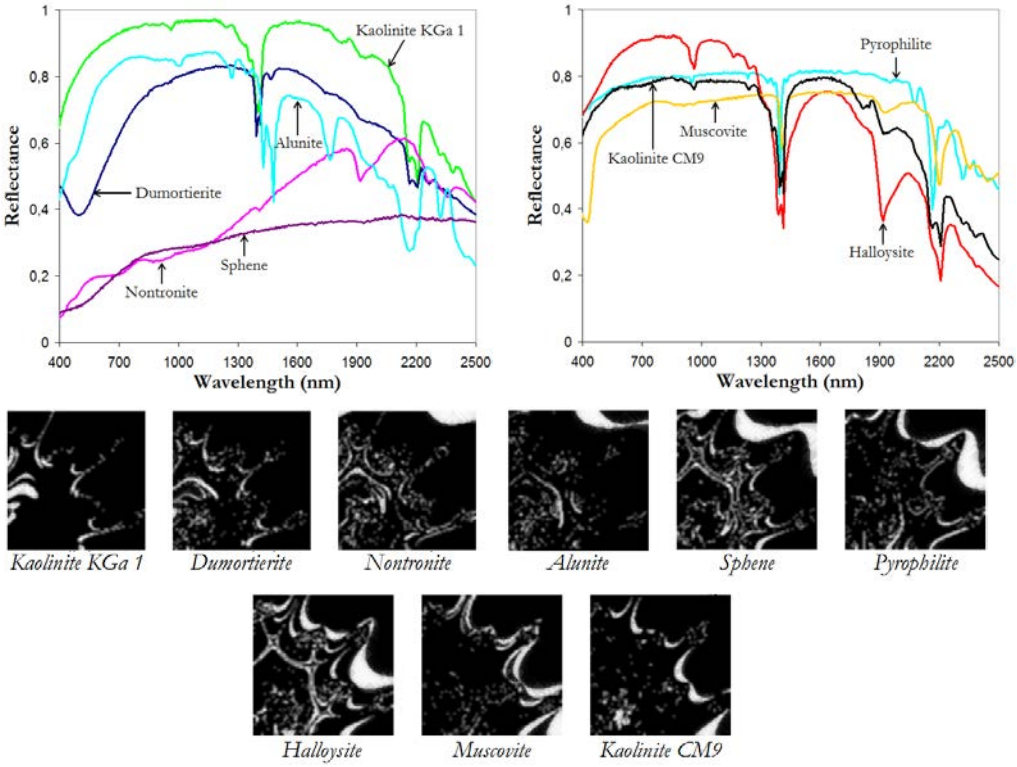

Figure 5.3: USGS library signatures (top) and fractional abundance distributions (bottom) considered for generating the simulated hyperspectral scene labeled as "Fractal 1" in experiments.

maps associated to each reference USGS signature in the construction of the synthetic scene are also displayed in Fig. 5.3, where black color indicates 0% abundance of the corresponding mineral, white color indicates 100% abundance of the mineral, and the fractional abundances in each pixel of the scene sum to unity, thus ensuring that the simulated fractal images strictly adhere to a fully constrained linear mixture model.

Finally, in order to evaluate the accuracy of compressive sensing algorithms we have developed a much simpler set of synthetic scenes. The reason is that we have experimentally observed that the synthetic scenes based on fractals may provide confusing interpretations when used to validate compressive sensing. Specifically, in compressive sensing we are more interested in analyzing the quality of the reconstruction independently of spectral mixing effects, while the fractal scenes are specifically developed to analyze the quality of the mixed pixel characterization process. In other words, the fractal images are characterized by a more complex structure designed for unmixing validation. As a result, we need more simple scenes in the latter case in order to properly substantiate the quality of reconstruction after compression in a simple and intuitive way. For this prupose, we have developed a set of synthetic scenes using again the USGS library [3]. The simulated images consist of a set of 5×5 squares of 10×10 pixels

[3] http://speclab.cr.usgs.gov/spectral-lib.html

(a) Endmember #1 (b) Endmember #2 (c) Endmember #3 (d) Endmember #4 (e) Endmember #5

Figure 5.4: True abundance maps used to generate a set of simple synthetic scenes used to validate compressive sensing algorithms.

each one, and the scenes have a total size of 110×110 pixels. The first row of squares contains the endmembers, the second row contains mixtures of two endmembers, the third row contains mixtures of three endmembers, and so on. Zero-mean Gaussian noise was added to the synthetic scenes with the SNR defined as $\text{SNR} = 10 \cdot \log_{\mathbf{10}} \frac{\mathbb{E}\|\mathbf{MA}\|_{\mathbf{F}}^{\mathbf{2}}}{\mathbb{E}\|\mathbf{N}\|_{\mathbf{F}}^{\mathbf{2}}}$, where $\mathbb{E}$ denotes mean value, to simulate contributions from ambient and instrumental noise sources. Fig. 5.4 displays the ground-truth abundances maps used for generating the synthetic scenes in this particular case.

5.2.2 Real hyperspectral data

In addition to synthetic data experiments, it is very important to substantiate algorithm performance using real data sets. However, the evaluation of compressive sensing and, particularly, spectral unmixing techniques is very difficult because there are very few hyperspectral scenes with reliable reference information that can be used to substantiate unmixing techniques. This is due to the fact that it is very difficult, in practice, to collect ground-truth information of fractional abundances at a sub-pixel level. However, the well-known AVIRIS Cuprite scene has been widely used to evaluate spectral unmixing applications. The scene, available online in reflectance units[4] after atmospheric correction, is characterized by the availability of some very reliable reference information available from USGS. Specifically, the portion used in experiments corresponds to a 350×350-pixel subset of the sector labeled as f970619t01p02_r02_sc03.a.rfl in the online data. The scene comprises 224 spectral bands between 0.4 and 2.5 μm, with full width at half maximum of 10 nm and spatial resolution of 20 meters per pixel. Prior to the analysis, several bands were removed due to water absorption and low SNR in those bands, leaving a total of 188 reflectance channels to be used in the experiments. The Cuprite site is well understood mineralogically, and has several exposed minerals of interest, all included in the USGS library considered in experiments, denoted splib06[5] and released in September 2007. In our experiments, we use spectra obtained from this library to validate endmember extraction algorithms. For illustrative purposes, Fig. 5.5 shows a mineral map produced in 1995 by USGS, in which the Tricorder 3.3 software product was used to map different minerals present in the Cuprite mining district[6]. It should be noted that the Tricorder map is only available for hyperspectral data collected in 1995, while the publicly available AVIRIS Cuprite data was collected in 1997. Therefore, a

[4] http://aviris.jpl.nasa.gov/html/aviris.freedata.html
[5] http://speclab.cr.usgs.gov/spectral.lib06
[6] http://speclab.cr.usgs.gov/cuprite95.tgif.2.2um_map.gif

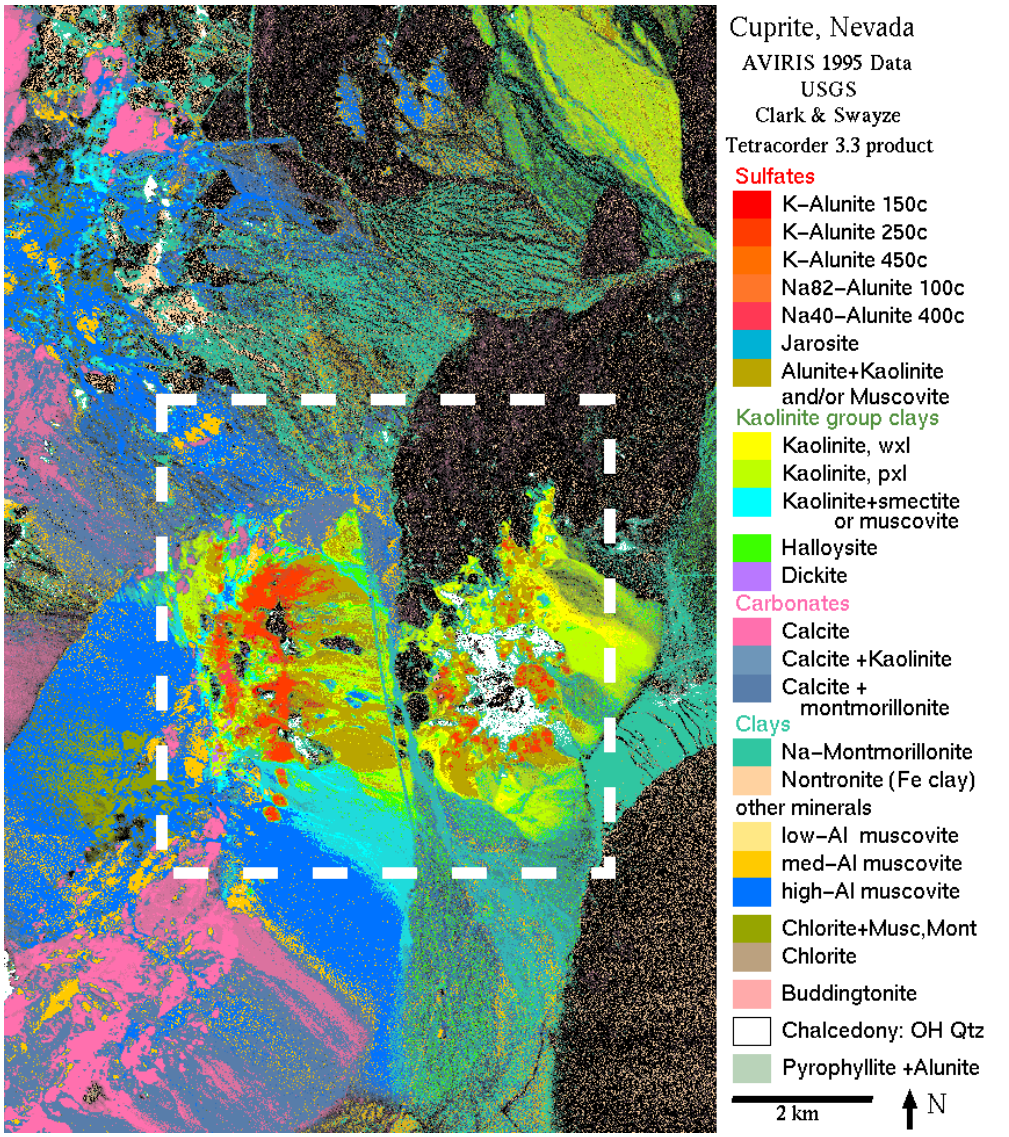

Figure 5.5: USGS map showing the location of different minerals in the Cuprite mining district in Nevada. The map is available online at: http://speclab.cr.usgs.gov/cuprite95.tgif.2.2um_map.gif. The white rectangle depicts the area used in our experiments.

direct comparison between the 1995 USGS map and the 1997 AVIRIS data (as well as a comparison in terms of fractional abundances) is not possible. In this work, we use the RMSE and NMSE metric to evaluate the quality of reconstruction provided by spectral unmixing and compressive sensing techniques, respectively.

5.3 Evaluation of spectral unmixing algorithms

In this section we present an evaluation of the new spectral unmixing techniques developed in this thesis work. Specifically, we will pay attention to the impact of spatial pre-processing on algorithms for spectral unmixing with and without the pure pixel assumption. The section is organized as follows. First, we illustrate the results obtained with synthetic data and then we conduct an evaluation using real data. The metrics used for evaluation purposes are the SA and the RMSE.

5.3.1 Results with synthetic data

This section describes the results obtained for spectral unmixing algorithms using the synthetic data sets generated using fractals. For clarity, we first conduct the evaluation using one synthetic scene only (i.e., the "Fractal 1" dataset). Then, we generalize the obtained results for all the synthetic data sets used in the comparison.

5.3.1.1 Analysis of one synthetic scene

The goal of this section is to analyze the impact of spatial pre-processing using only one of the synthetic scenes generated for validation. The scene selected is the "Fractal 1" data set. Of particular importance in this preliminary assessment is to analyze how the regions in the scene are characterized (since the generation of the scene was based up on simulated regions). Fig. 5.6(a) shows the band #50 of the "Fractal 1" image with SNR = 110 dB which is, from the practical point of view, absence of noise. On the other hand, Fig. 5.6(b) shows the result obtained after a clustering of the scene (using the ISODATA algorithm). Finally, Fig. 5.6(c) shows the regions obtained by the RBSPP algorithm after the region selection steps. The parameter g_{min} of ISODATA was set empirically to p, the number of endmembers estimated by a consensus between VD and HYSIME, while the parameter g_{max} was set to $2p$, a value that generates an explicit over-segmentation in order to let the algorithm automatically decide about the number of classes. As we can see in Fig. 5.6, the algorithm selects the largest regions in the classification map with highest purity. If we compare the selected regions with the fractional abundance maps for the "Fractal 1" displayed in Fig. 5.3, we can see that a high abundance value is observed in the pixels of the selected regions. This result intuitively indicates that the RBSPP method can properly guide the endmember extraction algorithms to those regions which are more likely to contain endmembers, discarding non-spatially homogeneous regions and non-pure regions which are more likely to contain mixed pixels, outliers and anomalous pixels.

In order to illustrate the performance of the proposed SSPP, we show the individual outcome of each processing step for the same "Fractal 1" synthetic image. Fig. 5.7 shows the outcome of applying Gaussian filtering with different values of σ for the synthetic image simulated with SNR=70 dB. On the other hand, Figs. 5.8(a-c) respectively show the outcome of calculating the RMSE between the original image and the images obtained after Gaussian filtering in Fig. 5.7. Figs. 5.8(d-h) respectively show the spatial homogeneity images obtained for the synthetic image with SNR values ranging between

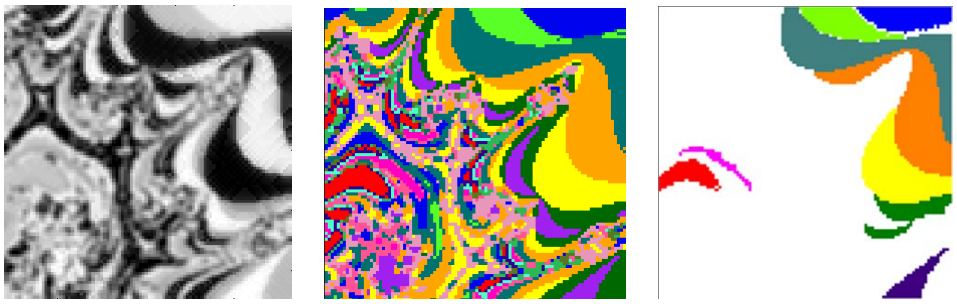

(a) Original image "Fractal 1" (b) ISODATA classification map (c) Regions selected by RBSPP

Figure 5.6: (a) Band #50 of the original image "Fractal 1" with SNR = 110 dB. (b) ISODATA classification map. (c) Regions selected by RBSPP in the case of "Fractal 1" dataset.

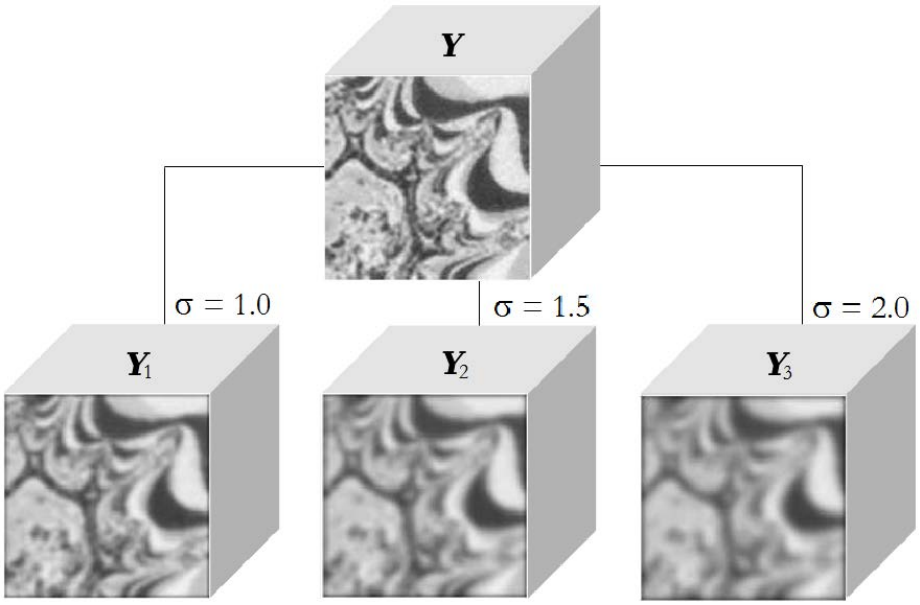

Figure 5.7: Gaussian filtering of the synthetic hyperspectral image "Fractal 1" in Fig. 5.3

30 dB and 110 dB . As shown by Figs. 5.8(d-h), the spatial homogeneity calculation is robust in the presence of noise. Figs. 5.8(i-m) respectively show the spectral purity images obtained for the synthetic image with SNR values ranging between 30 dB and 110 dB . Fig. 5.8(n) shows the outcome of the unsupervised clustering procedure with ISODATA for the synthetic image with SNR=110 dB . Finally, Figs. 5.8(o-s) shows spatially selected pixels during the fusion step after considering values of ρ from 50 to 90. Figs. 5.8(t-x) shows spectrally selected pixels during the fusion step after considering values of β from 50 to 90. The most important conclusion that can be derived from this example is that the SSPP can provide similar results with regards to those obtained by the RBSPP in the considered scene but, quite importantly, the SSPP is able to tolerate higher noise rations in order to provide the same results.

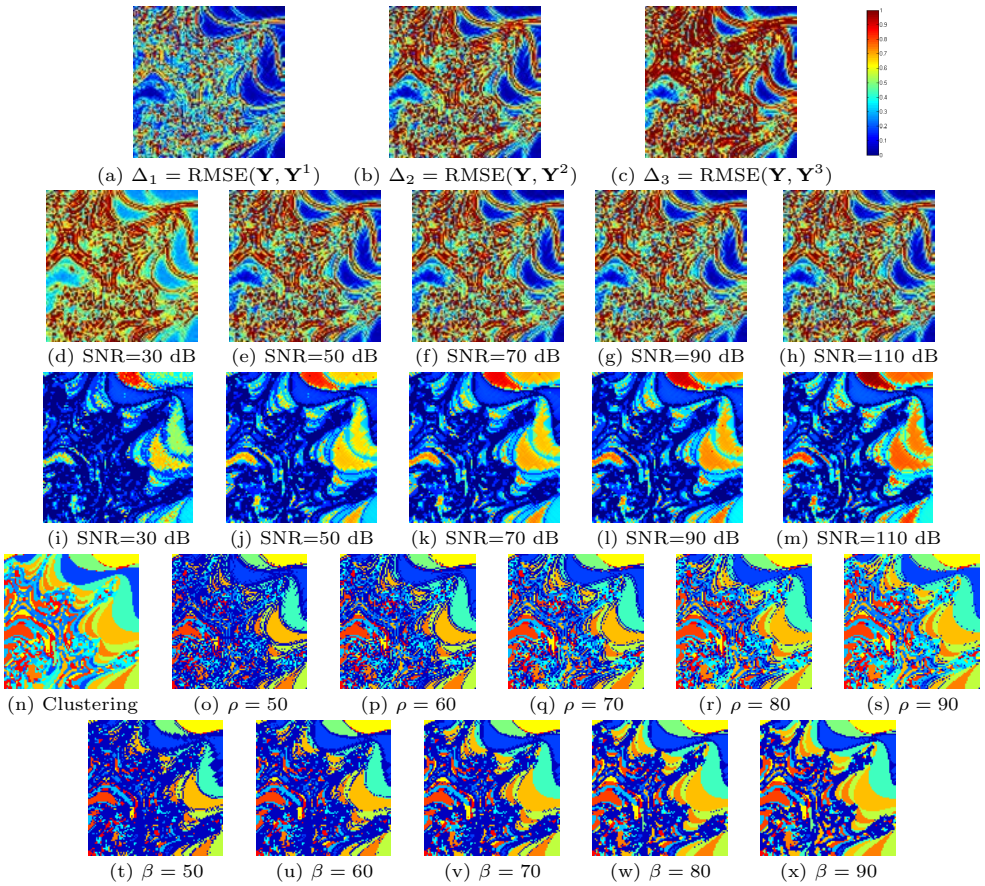

(a) $\Delta_1 = \text{RMSE}(\mathbf{Y}, \mathbf{Y}^1)$ (b) $\Delta_2 = \text{RMSE}(\mathbf{Y}, \mathbf{Y}^2)$ (c) $\Delta_3 = \text{RMSE}(\mathbf{Y}, \mathbf{Y}^3)$

(d) SNR=30 dB (e) SNR=50 dB (f) SNR=70 dB (g) SNR=90 dB (h) SNR=110 dB

(i) SNR=30 dB (j) SNR=50 dB (k) SNR=70 dB (l) SNR=90 dB (m) SNR=110 dB

(n) Clustering (o) $\rho = 50$ (p) $\rho = 60$ (q) $\rho = 70$ (r) $\rho = 80$ (s) $\rho = 90$

(t) $\beta = 50$ (u) $\beta = 60$ (v) $\beta = 70$ (w) $\beta = 80$ (x) $\beta = 90$

Figure 5.8: Performance of SSPP with the simulated hyperspectral scene labeled as "Fractal 1". (a-c) Outcome of calculating the RMSE between the original synthetic image and the images obtained after Gaussian filtering in Fig. 5.7. (d-h) Spatial homogeneity scores for different SNR values.(i-m) Spectral purity scores for different SNR values. (n) Spectral clustering of the image with SNR=110 dB . (o-s) Spatially selected pixels during the fusion step considering different values of ρ.(t-x) Spectrally selected pixels during the fusion step considering different values of β.

5.3.1.2 Comparative assessment using all synthetic scenes

Before describing our experiments, it is first important to address the parameter values used for the our proposed algorithms. In the case of SPP we optimized the spatial window size in each experiment and only report the best obtained results for each considered metric in each case. In the case of the RBSPP, for the different clustering methods the parameter g_{min} of ISODATA was set empirically to p, the number of endmembers estimated by a consensus between VD and HYSIME, while the parameter g_{max} was set to $2p$, a value that generates an explicit over-segmentation in order to let the algorithm automatically decide about the number of classes. In the case of k-means and RHSEG, we explicitly set $g = p$. For RHSEG we also set $spectral\_wght = 0.2$, which results in a good trade-off between spatial and spectral information [93]. Finally, in the case of

SSPP the parameters ρ, β and σ were carefully optimized on each case. The threshold used during the spectrally purity index calculation step was set to $\theta = 0.7$ empirically. In summary, the three spatial pre-processing methods were carefully optimized in each experiment and only the best results are reported in our comparison.

Table 5.1 shows the average SA scores (in degrees) between the reference USGS mineral spectra and their corresponding endmember pixels produced by several endmember extraction algorithms, across the five synthetic scenes in Fig. 5.1. As a result, each value reported in Table 5.1 corresponds to the average SA obtained after processing the five considered scenes with the same SNR (five different SNR values, ranging from 30 dB to 110 dB , are reported in the table). In all cases, the input parameters of the different endmember extraction methods tested have been carefully optimized so that the best performance observed for each method after a wide range of values for each parameter is reported.

In order to study the impact of the clustering techniques in the RBSPP method we performed the experiments with the different unsupervised clustering techniques considered in this thesis work (ISODATA, k-means and RHSEG). As shown by Table 5.1 the impact of the clustering method is not very high so that in the following we use only the ISODATA algorithm for simplicity. As shown by Table 5.1, the combination of the proposed RBSPP and SSPP methods with spectral-based algorithms does not always provide the best results in terms of SA. The SA is probably not the best tool for measuring spectral similarities when the differences are just in a few –but diagnostic– wavelengths (e.g., the spectra of Muscovite and Pyrophilite in Fig. 5.3). However, the results obtained by the proposed spatial pre-processing algorithms are always comparable to those provided by other methods, and just in a few cases RBSPP and SSPP in combination with the method outperforms the results provided by the original method. The best results in Table 5.1 for the case of lower SNR (30 dB) are found by SSPP+VCA and RBSPP+VCA in first and second place. This is due to VCA is the only considered endmember extraction algorithm which performs noise characterization in the data before conducting the endmember search. Since RBSPP and SSPP discards those pixels which are contained in mixed regions, the noise characterization process conducted by VCA is more efficient for endmember extraction purposes because it is performed only with those pixels located in spectrally pure and spatially homogeneous regions.

As shown by Table 5.1, the combination of the proposed SSPP method with spectral-based algorithms without the pure signature assumption (N-FINDR, OSP and VCA) generally provides the best results (lower spectral angles) when the SNR is very low (30 dB), also in the case of RBSPP the higher the noise the better the results with regards the spectral-based algorithms without the pure signature assumption. This indicates robustness of the proposed approaches in high noise conditions. As the SNR increases, the results obtained by SSPP and RBSPP are always comparable to those provided by other pre-processing methods. It is also clear from Table 5.1 that the algorithms without the pure signature assumption (MVSA and SISAL) provide the worst spectral angle scores when the noise is very high. This is expected, as these algorithms generate the endmembers form the simplex with minimum volume enclosing all observations and are,

Table 5.1: Average spectral similarity scores (in degrees) between the USGS mineral spectra and their corresponding endmember pixels produced by several endmember extraction algorithms across the five synthetic scenes in Fig. 5.1.

Algorithm	**SNR=30 dB**	**SNR=50 dB**	**SNR=70 dB**	**SNR=90 dB**	**SNR=110 dB**
N-FINDR	2.095	0.463	0.383	0.388	0.361
OSP	2.118	0.452	0.349	0.361	0.345
VCA	1.193	0.467	0.377	0.430	0.426
MVSA	13.908	1.365	0.130	0.028	0.024
SISAL	5.129	1.259	0.541	0.553	0.193
SPP+N-FINDR	2.293	0.778	0.701	0.694	0.693
SPP+OSP	2.342	0.622	0.536	0.529	0.529
SPP+VCA	2.271	0.455	0.327	0.319	0.347
SPP+MVSA	12.451	1.007	0.100	0.023	0.020
SPP+SISAL	2.159	0.621	0.113	0.064	0.328
RBSPP*+N-FINDR	2.174	0.874	0.676	0.786	0.804
RBSPP*+OSP	2.226	0.764	1.020	1.088	1.034
RBSPP*+VCA	**1.033**	0.685	0.678	0.809	0.714
RBSPP*+MVSA	14.323	**1.114**	**0.110**	0.029	0.254
RBSPP*+SISAL	6.365	2.083	1.176	0.949	2.043
RBSPP†+N-FINDR	2.220	0.648	0.708	0.618	0.690
RBSPP†+OSP	2.275	0.588	0.724	0.605	0.567
RBSPP†+VCA	1.307	0.973	0.890	0.761	0.512
RBSPP§+N-FINDR	2.272	0.982	0.845	0.677	0.895
RBSPP§+OSP	3.332	0.910	0.860	0.809	0.941
RBSPP§+VCA	1.301	0.818	0.936	0.686	1.083
SSPP+N-FINDR	**2.089**	0.538	0.403	0.454	0.556
SSPP+OSP	**2.107**	0.520	0.384	0.439	0.452
SSPP+VCA	**1.010**	0.722	**0.176**	**0.180**	**0.189**
SSPP+MVSA	**11.896**	**1.007**	**0.108**	**0.024**	**0.020**
SSPP+SISAL	**3.597**	**1.158**	**0.151**	**0.242**	**0.098**
AMEE	2.670	1.260	0.969	1.193	1.252
SSEE	2.124	1.077	0.576	0.722	0.645

*Implemented with ISODATA. †Implemented with k-means. §Implemented with RHSEG.

generally, sensitive to noise. However, Table 5.1 reveals that pre-processing methods can be beneficial for such algorithms. In particular, the proposed SSPP in combination with the MVSA algorithm outperforms in all cases providing the best result when the SNR is very high (110 dB), and with SISAL in high noise cases. In the other hand the RBSPP also outperforms in the case of MVSA with 50 dB and 70 dB . As a result, we can conclude that our proposed spatial pre-processing techniques have the potential to improve endmember identification algorithms, with and without the pure signature assumption, in different noise conditions. Since our proposed spatial pre-processing techniques discard those pixels which are not relevant to the endmember extraction process, the search conducted by such algorithms is more efficient because it is performed only using those pixels located in spatially homogeneous and spectrally pure regions.

On the other hand, Table 5.2 shows the RMSE scores (measured across the five synthetic scenes in Fig. 5.1) after reconstructing the scenes using the endmembers extracted by several methods. Again, each value reported in the table corresponds to the RMSE obtained after reconstructing five different scenes but simulated with the same SNR. In all cases, we derive $p = 9$ endmembers using the different tested methods and then estimate their fractional abundances in the original hyperspectral image using FCLSU [4]. Then, we reconstruct the original image using the derived endmembers and fractional abundances, and measure the error with regards to the original hyperspectral scene using RMSE. Table 5.2 indicates that the MVSA and SISAL (without any pre-processing) provide the best overall results (lower RMSE values) across all tested methods, regardless of the considered SNR in the simulation. This is a consequence of the fact that these algorithms generate *virtual* endmembers, intended to perfectly enclose all other observations in the data. Resulting from their *virtual* nature, these endmembers could be far away from the true endmembers and still provide low RMSE reconstruction errors. From this perspective, the application of pre-processing methods such as SSPP and RBSPP does not significantly affect the performance of these two algorithms in terms of RMSE. However, it is very important to emphasize that the *virtual* endmembers generated by MVSA and SISAL may be unrealistic or far away from the true endmembers used in the image simulations. In this regard, our previous experiments in Table 5.1 (using the spectral angle as the similarity criterion) indicated that SSPP and RBSPP have the potential to improve the similarity of extracted endmembers with regards to the reference signatures used for the construction of the hyperspectral scenes while, at the same time, produce very low RMSE scores in Table 5.2. This is a very important feature, as it reveals that pre-processing can assist MVSA and SISAL to produce *virtual* endmembers which are more realistic in nature. Although the results obtained with synthetic hyperspectral scenes are very encouraging, further experiments with a real hyperspectral scene are conducted in the following subsection in order to fully substantiate the advantages that can be gained by using pre-processing methods prior to endmember extraction and spectral unmixing.

Table 5.2: Average error scores after reconstructing the five synthetic scenes in Fig. using the endmembers extracted by several methods.

Algorithm	**SNR=30 dB**	**SNR=50 dB**	**SNR=70 dB**	**SNR=90 dB**	**SNR=110 dB**
N-FINDR	0.356	0.039	0.009	0.007	0.008
OSP	0.359	0.039	0.010	0.008	0.008
VCA	0.369	0.044	0.017	0.021	0.018
MVSA	0.297	0.030	0.003	0.001	0.000
SISAL	0.297	0.030	0.003	0.001	0.000
SPP+N-FINDR	0.359	0.045	0.017	0.016	0.016
SPP+OSP	0.368	0.048	0.016	0.015	0.015
SPP+VCA	0.368	0.040	0.011	0.009	0.009
SPP+MVSA	0.297	0.030	0.003	0.001	0.000
SPP+SISAL	0.312	0.030	0.003	0.001	0.001
RBSPP+N-FINDR	0.358	0.049	0.028	0.026	0.028
RBSPP+OSP	0.359	0.055	0.072	0.054	0.054
RBSPP+VCA	0.308	0.048	0.033	0.043	0.028
RBSPP*+N-FINDR	0.358	0.049	0.028	0.026	0.028
RBSPP*+OSP	0.359	0.055	0.072	0.054	0.054
RBSPP*+VCA	**0.308**	0.048	0.033	0.043	0.028
RBSPP*+MVSA	**0.297**	**0.030**	**0.003**	**0.001**	0.004
RBSPP*+SISAL	0.310	**0.030**	**0.003**	**0.001**	0.004
RBSPP†+N-FINDR	0.360	0.042	0.018	0.018	0.022
RBSPP†+OSP	0.361	0.042	0.019	0.023	0.017
RBSPP†+VCA	0.320	0.070	0.034	0.070	0.029
RBSPP§+N-FINDR	0.372	0.078	0.023	0.023	0.024
RBSPP§+OSP	0.388	0.087	0.025	0.029	0.027
RBSPP§+VCA	0.340	0.066	0.040	0.035	0.046
SSPP+N-FINDR	**0.356**	0.040	0.012	0.011	0.014
SSPP+OSP	**0.356**	0.040	0.012	0.011	0.011
SSPP+VCA	**0.310**	0.052	**0.007**	**0.004**	**0.006**
SSPP+MVSA	**0.297**	**0.030**	**0.003**	**0.001**	**0.000**
SSPP+SISAL	**0.297**	**0.030**	**0.003**	0.003	**0.000**
AMEE	0.627	0.484	0.468	0.473	0.484
SSEE	0.358	0.135	0.035	0.066	0.026

*Implemented with ISODATA. †Implemented with k-means. §Implemented with RHSEG.

5.3.2 Results with real data

In this section we will describe the experiments performed with the real dataset collected by AVIRIS over the Cuprite mining district. We first show a comparison of the results obtained for the endmember extraction algorithms with respect the pre-processing techniques developed in this thesis work in terms of accuracy and also in terms of computational complexity. Table 5.3 tabulates the SA scores (in degrees) obtained after comparing the USGS library spectra of *alunite*, *buddingtonite*, *calcite*, *kaolinite* and *muscovite*, with the corresponding endmembers extracted by different algorithms from the AVIRIS Cuprite scene. In all cases, the input parameters of the different endmember extraction methods tested have been carefully optimized so that the best performance for each method is reported. The smaller the SA values across the five minerals in Table 5.3, the better the results. It should be noted that Table 5.3 only displays the smallest SA scores of all endmembers with respect to each USGS signature for each algorithm. For reference, the mean SA values across all five USGS signatures is also reported. The number of endmembers to be extracted was set to $p = 19$ in all experiments after the consensus reached between HYSIME [7] and the VD concept [25], implemented using $P_F = 10^{-3}$ as the input false alarm probability. As shown by Table 5.3, the use of SSPP and RBSPP provide similar results with respect to the endmember extraction algorithms with the pure signature assumption such as VCA. However in the case of the endmember extraction algorithms without the pure pixel assumption such as MVSA and SISAL there is a clear improvement in the case of SSPP and also RBSPP improves the results with respect to the SISAL algorithm. In this experiment, however, the best performance (in terms of spectral angle) was obtained by the endmember extraction algorithms AMEE which include both spatial and spectral information.

On the other hand, Fig. 5.9 shows the error maps obtained after reconstructing the AVIRIS Cuprite scene using $p = 19$ endmembers extracted by different methods. Fig. 5.9 shows that the use of SSPP and RBSPP for pre-processing increases slightly the RMSE obtained by these algorithms, but as we observed in Table 5.3 this has also the potential to provide more realistic endmembers for those algorithms. Hence, the joint analysis of the two considered metrics (spectral angle and reconstruction RMSE) indicates that pre-processing using SSPP and RBSPP can significantly improve the performance of algorithms without the pure signature assumption. As shown by Fig. 5.9, SSPP also provides the lowest reconstruction RMSE scores as compared with the other pre-processing schemes when applied to the algorithms designed under the pure signature assumption (N-FINDR, OSP and VCA) and RBSPP also provide better results with these algorithms.

From the experiments reported in this subsection, we can conclude that the inclusion of the spatial information on the spectral unmixing process can improve the available spectral unmixing algorithms. By guiding the endmember extraction process to those regions which are spatially homogeneous we reduce the noise effect in the endmember extraction process and also discard anomalous pixels.

To conclude this section, we note that the application of SSPP and RBSPP does not increase the computational complexity of the endmember identification stage.

Table 5.3: Spectral similarity scores (in degrees) between USGS mineral spectra and their corresponding endmembers extracted by several algorithms from the AVIRIS Cuprite scene.

Algorithm	**Alunite GDS84**	**Buddingtonite GDS85**	**Calcite WS272**	**Kaolinite KGa-1**	**Muscovite GDS107**	**Mean**
N-FINDR	4.81	4.29	7.60	9.92	5.05	6.33
OSP	4.81	4.16	9.52	10.76	5.29	6.91
VCA	6.91	5.38	9.53	9.65	6.47	7.59
MVSA	12.72	8.41	5.69	15.04	5.36	9.44
SISAL	9.78	5.13	12.78	13.53	8.00	9.84
SPP+N-FINDR	7.72	4.27	9.34	11.26	5.69	7.66
SPP+OSP	6.06	4.27	8.43	12.28	4.64	7.14
SPP+VCA	14.11	8.49	11.94	13.86	5.61	10.80
SPP+MVSA	8.43	8.46	17.52	10.41	13.32	11.63
SPP+SISAL	9.02	5.06	11.41	9.21	7.21	8.38
RBSPP+N-FINDR	7.22	5.71	**5.59**	10.43	5.08	6.81
RBSPP+OSP	6.86	**4.16**	10.05	11.14	5.70	7.58
RBSPP+VCA	6.86	**4.34**	**8.31**	10.19	5.42	**7.02**
RBSPP+MVSA	**8.41**	**6.53**	**4.94**	**12.72**	15.42	9.60
RBSPP+SISAL	**7.80**	6.33	**9.03**	**10.85**	**5.28**	**7.86**
SSPP+N-FINDR	5.48	6.31	5.70	**9.64**	5.86	6.60
SSPP+OSP	7.46	6.13	**5.50**	**9.64**	5.95	6.94
SSPP+VCA	**5.48**	6.72	**9.53**	11.10	**4.77**	**7.52**
SSPP+MVSA	**9.46**	**6.39**	**4.95**	**11.93**	6.21	**7.79**
SSPP+SISAL	**6.95**	**4.91**	**11.71**	**8.25**	**6.91**	**7.74**
AMEE	4.81	4.17	5.87	8.74	4.61	5.64
SSEE	4.81	4.16	8.48	10.73	4.63	6.57

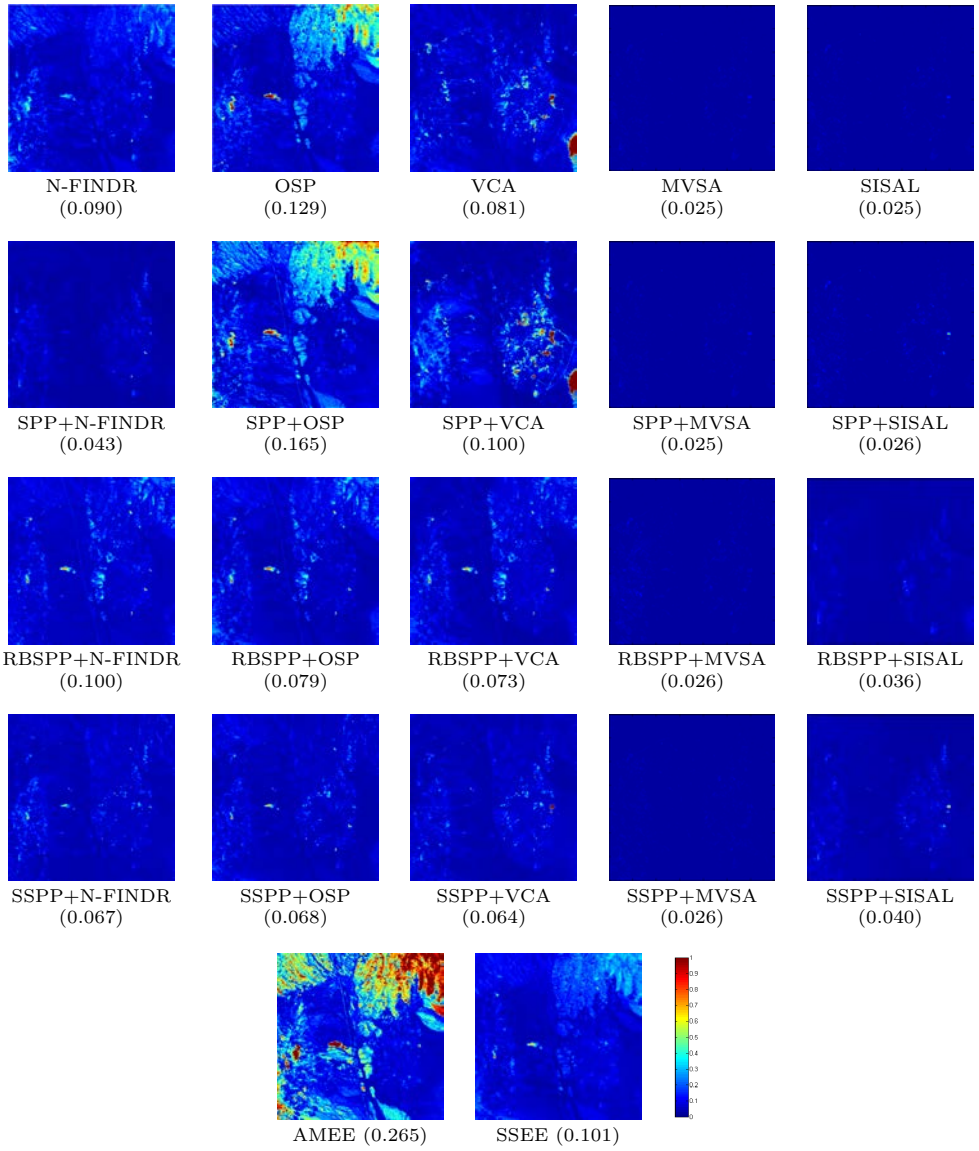

Figure 5.9: Errors measured for various endmember extraction algorithms after reconstructing the AVIRIS Cuprite scene.

This is because the pre-processing acts as a pixel selection module that discards a significant number of pixels (prior to endmember extraction) using both spatial and spectral information. Hence, the proposed SSPP and RBSPP have the potential to significantly reduce the time needed by endmember identification algorithms to conduct the endmember searching process (see Table 5.4). Even if the SSPP is slightly more complex than the other two pre-processing frameworks tested (SPP and RBSPP), it can significantly accelerate the endmember identification stage by discarding a higher number of pixels, thus resulting in low total processing times in Table 5.4. This is particularly the case for MVSA, which could significantly reduce its high complexity due to the smaller

pool of pixels fed to the algorithm after pre-processing.

5.4 Evaluation of compressive sensing algorithms

In this section we evaluate the performance of the newly developed HYCA and C-HYCA algorithms for hyperspectral compressive sensing. Again, we perform experiments with both synthetic and real data sets. However, in this section we use the simple synthetic scenes in Fig. 5.4 instead of the fractal images. This is because, in order to validate compressive sensing techniques, we prefer to use a simple toy example to empirically prove model. However, the fractal images were specifically developed for the spectral unmixing validation and they were generated using complex fractal patterns which could confuse our validation. Then, we perform a validation of compressive sensing techniques using real hyperspectral data as well.

5.4.1 Results with synthetic data

In this subsection, we conduct a series of experiments using different versions of HYCA and C-HYCA algorithms on synthetic data. Specifically, we have considered three cases. In the first case we disabled the non-negativity constraint and we assumed that the mixing matrix $\mathbf{M}^*$ is an orthogonal matrix computed as $\mathbf{M}^* := orth(\mathbf{M})$, where $\mathbf{M}$ denotes the original mixing matrix used to generate the dataset and $\mathbf{M}^*$ denotes the mixing matrix used in the reconstruction algorithm. In the second case we used for sampling $\mathbf{H}_i = \mathbf{G}_i\mathbf{M}^\sharp$ without the non-negativity constraint. Finally, in the third case we used the non-negativity constraint considering the original mixing matrix used for the dataset generation. In this experiment, we set $q = 3$. Since the original data set has $l = 224$ bands, the compression ratio is $l/q = 74.67$ and the number of measurements per pixel band is $q/l = 0.0134$. In our experiments, we set the window size $ws = 2$.

Table 5.5 shows the NMSE obtained for both versions (HYCA and C-HYCA) in different cases. We performed 10 Monte-Carlo runs, sampling not only the noise but also the elements of the linear operator H. The regularization parameter λ was hand-tuned for optimal performance in the case of the HYCA algorithm. Having in mind the linear model, the parameter δ is set to $\delta = \|H(\mathbf{N})\|_F$. As we can see in Table 5.5, by disabling the non-negativity constraint the algorithm is more robust to noise. However, the implementation with the non-negativity constraint provides better results when there is no noise. This is expected, as noise introduces outliers in the model which lead to errors in the reconstruction when we use the non-negativity constraint. If we compare the HYCA and C-HYCA criteria on Table 5.5, we can see that both versions provide very good results with low reconstruction errors. We can also observe that HYCA outperforms C-HYCA, which is probably due to the parameter optimization conducted in the case of HYCA.

Table 5.4: Processing times (in seconds) measured in a desktop PC with intel core i7 920 CPU at 2.67 Ghz with 4 GB of RAM.

Algorithm	**Preprocessing time**	**Endmember extraction time**	**Total processing time**
N-FINDR	-	466.08	466.08
OSP	-	136.09	136.09
VCA	-	31.12	31.12
MVSA	-	$\simeq$ 25000	$\simeq$ 25000
SISAL	-	170.40	170.40
SPP+N-FINDR	50.06	466.08	516.14
SPP+OSP	50.06	136.09	186.15
SPP+VCA	50.06	31.12	81.18
SPP+MVSA	50.06	$\simeq$ 25000	$\simeq$ 25000
SPP+SISAL	50.06	170.40	220.46
RBSPP+N-FINDR	96.51	17.72	**114.23**
RBSPP+OSP	96.51	5.71	**102.22**
RBSPP+VCA	96.51	5.89	102.40
RBSPP+MVSA	96.51	967.40	**1063.91**
RBSPP+SISAL	96.51	170.40	**166.91**
SSPP+N-FINDR	77.49	15.24	**92.73**
SSPP+OSP	77.49	3.60	**81.09**
SSPP+VCA	77.49	1.69	79.18
SSPP+MVSA	77.49	393.53	**471.02**
SSPP+SISAL	77.49	6.16	**83.65**
AMEE	–	76.06	76.06
SSEE	–	1051.23	1051.23

Table 5.5: Average NMSE between the original and the reconstructed dataset for $q = 3$ and different SNR values, after 10 Monte-Carlo runs.

Version	SNR=30db	SNR=50db	SNR=70db	SNR=∞
HYCA *	$8.27 \cdot 10^{-4}$	$0.52 \cdot 10^{-4}$	$0.52 \cdot 10^{-4}$	$0.30 \cdot 10^{-4}$
HYCA †	$0.44 \cdot 10^{-4}$	$0.45 \cdot 10^{-4}$	$0.40 \cdot 10^{-4}$	$0.37 \cdot 10^{-4}$
HYCA §	$21.08 \cdot 10^{-4}$	$0.68 \cdot 10^{-4}$	$0.33 \cdot 10^{-4}$	$0.20 \cdot 10^{-4}$
C-HYCA *	$22.7 \cdot 10^{-4}$	$3.35 \cdot 10^{-4}$	$3.24 \cdot 10^{-4}$	$3.36 \cdot 10^{-4}$
C-HYCA †	$2.73 \cdot 10^{-4}$	$2.00 \cdot 10^{-4}$	$1.31 \cdot 10^{-4}$	$1.59 \cdot 10^{-4}$
C-HYCA §	$7.26 \cdot 10^{-4}$	$0.51 \cdot 10^{-4}$	$0.29 \cdot 10^{-4}$	$0.28 \cdot 10^{-4}$

* First case without non-negativity and $\mathbf{E}^* := orth(\mathbf{E})$. † Second case with $\mathbf{H}_i = \mathbf{G}_i\mathbf{E}^\sharp$. § Third case using the non-negativity constraint.

5.4.2 Results with real data

In this experiment, we use the well-known AVIRIS Cuprite data set, available online in reflectance units after atmospheric correction. This scene has been widely used to validate the performance of endmember extraction algorithms. The portion used in experiments corresponds to a 250 by 190 pixels subset of the sector labeled as f970619t01p02_r02_sc03a.rfl in the online data. The scene comprises 224 spectral bands between 0.4 and 2.5 μm, with full width at half maximum of 10 nm and spatial resolution of 20 meters per pixel. Prior to the analysis, several bands were removed due to water absorption and low SNR in those bands, leaving a total of 188 reflectance channels to be used in the experiments. We used a window size of $ws = 2$, so that $m = 4$. Here, we estimated the number of endmembers with HYSIME algorithm [7].

Here, we have also considered the same three cases as in the experiment with simulated data. But in this case the mixing matrix was estimated from the original data using the VCA [26], so that in the first case we use $\mathbf{M}^* := orth(\widehat{\mathbf{M}})$ where $\widehat{\mathbf{M}}$ is the mixing matrix estimated by VCA algorithm. In the second case $\mathbf{H}_i = \mathbf{G}_i\widehat{\mathbf{M}}^\sharp$ and $\mathbf{M}^* := \widehat{\mathbf{M}}$. Finally in the third case, due to the non-linear mixtures and outliers present in the real images, the non-negativity constraint may be violated. In order to ensure that the mixing matrix encloses the whole data set and the non-negativity constraint is satisfied, we open the cone defined in the mixing matrix $\mathbf{M}^*$ as follows:

$$\mathbf{M}^* := \widehat{\mathbf{M}} + \Delta \cdot (\widehat{\mathbf{M}} - \overline{\mathbf{M}}) \tag{5.4}$$

where Δ is a scalar which defines how much the cone is opened and $\overline{\mathbf{M}}$ is a matrix containing the mean spectrum of the endmembers. By choosing a value of Δ large enough, then all observed spectral vectors are inside the cone. In the current data set, $\Delta = 6$ ensures this constraint. In order to evaluate the performance of HYCA and C-HYCA with the real dataset, we perform experiments with the compression ratios $224/q$ with $q = 5, 9, 13, 17$. In all cases we used a window size of $ws = 2$.

Table 5.6 shows the value of NMSE over 10 Monte-Carlo runs for several versions of the proposed method with different compression ratios over the Cuprite dataset. In this experiment we can see that the version with the non-negativity constraint provide better

Table 5.6: Average NMSE between the AVIRIS Cuprite data and its reconstructed version (after 10 Monte-Carlo runs) for different compression ratios.

Version	$q = 5$	$q = 9$	$q = 13$	$q = 17$
HYCA *	$98.13 \cdot 10^{-4}$	$5.21 \cdot 10^{-4}$	$2.59 \cdot 10^{-4}$	$4.54 \cdot 10^{-4}$
HYCA †	$376.83 \cdot 10^{-4}$	$200.39 \cdot 10^{-4}$	$108.80 \cdot 10^{-4}$	$34.56 \cdot 10^{-4}$
HYCA §	$4.66 \cdot 10^{-4}$	$2.50 \cdot 10^{-4}$	$1.28 \cdot 10^{-4}$	$1.05 \cdot 10^{-4}$
C-HYCA *	$24.05 \cdot 10^{-4}$	$5.77 \cdot 10^{-4}$	$3.54 \cdot 10^{-4}$	$2.63 \cdot 10^{-4}$
C-HYCA †	$590.82 \cdot 10^{-4}$	$351.57 \cdot 10^{-4}$	$268.54 \cdot 10^{-4}$	$225.88 \cdot 10^{-4}$
C-HYCA §	$3.84 \cdot 10^{-4}$	$2.24 \cdot 10^{-4}$	$1.74 \cdot 10^{-4}$	$1.31 \cdot 10^{-4}$

* First case without non-negativity and $\mathbf{M}^* := orth(\mathbf{M})$. † Second case with $\mathbf{H}_i = \mathbf{G}_i\mathbf{M}^\sharp$. § Third case using the non-negativity constraint.

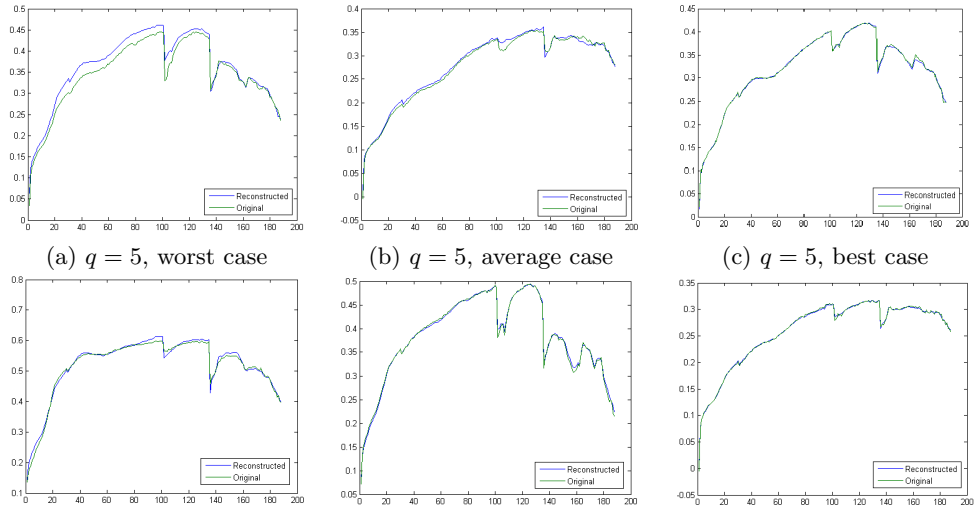

(a) $q = 5$, worst case (b) $q = 5$, average case (c) $q = 5$, best case

(d) $q = 15$, wort case (e) $q = 15$, average case (f) $q = 15$, best case

Figure 5.10: Worst (a,d), average (b,e), and best (c,f) reconstructed pixels in the AVIRIS Cuprite scene for values of $q = 5$ and $q = 15$, respectively.

.

results than the other versions. Here, we observe a slightly worse performance in the second case which is probably due to the fact that we are estimating the endmembers from the original data. For illustrative purposes, Fig. 5.10 shows the reconstructed and the original spectral signatures with highest, average and lowest error for the C-HYCA algorithm (with the non-negativity constraint) for different compression ratios. In this plot, we can see that, even in the worst case, the reconstructed pixel preserves the shape of the original pixel, which means that the features of the signature are well-preserved. In the other two cases the reconstructed and the original pixels are extremely similar.

Fig. 5.11 shows the NMSE between the original and the reconstructed images of Cuprite for different compression ratios. Note that the scale of this figures is between 0 and $2 \cdot 10^{-3}$. Most of errors are in the transitions areas between different land-cover classes. This is expected, as the TV regularizer promotes smoothness in the homogeneous regions. Furthermore, Fig. 5.11 indicates that most of the pixels have a very low

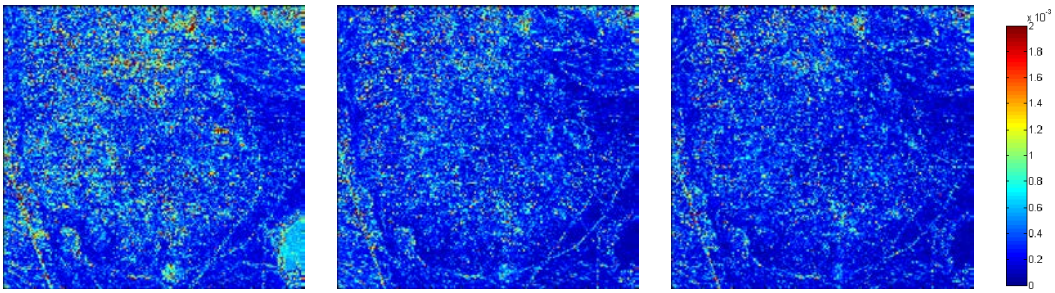

(a) $q = 5$ (b) $q = 7$ (c)$q = 9$

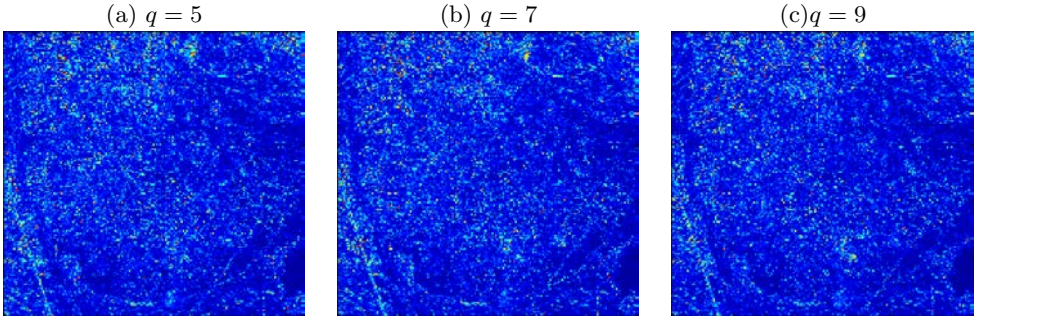

(d) $q = 11$ (e)$q = 13$ (f) $q = 15$

Figure 5.11: NMSE between the original and the reconstructed Cuprite dataset for different compression ratios (a-f)

.

Table 5.7: NMSE between the original and the reconstructed Cuprite dataset after applying 10 Monte-Carlo runs of the C-HYCA algorithm with values of $ws = [4, 6, 8]$ and compression ratio of l/q with $l = 188$ and $q = 5$.

Algorithm	$ws = 4$	$ws = 6$	$ws = 8$
C-HYCA	$2.95 \cdot 10^{-4}$	$3.01 \cdot 10^{-4}$	$3.01 \cdot 10^{-4}$

reconstruction error, which means that the reconstructed and the original spectrum are very similar in most of the cases. This proves the effectiveness of the proposed unmixing-based compressive sensing framework using spatial information. Note that the spectra shown in Fig. 5.10(a,d) correspond to the worst case, a situation in which the error is much higher than the errors of the large majority of the pixels in the image. This can be achieved without much effort in parameter settings, particularly in the C-HYCA implementation which is less sensitive to parameter inputs. In order to illustrate the sensitivity of the constrained version of HYCA to different window sizes, Table 5.7 shows the values of NMSE obtained for the C-HYCA algorithm applied to the AVIRIS Cuprite dataset using different window sizes $ws = [4, 6, 8]$ and compression ratio l/q with $l = 188$ and $q = 5$. As we can see in Table 5.7, the results are very similar for different window sizes but slightly better results can be found by choosing an optimum window size of $ws = 4$.

To conclude this section, Table 5.8 shows the execution time of the HYCA and C-HYCA reconstruction algorithms for the AVIRIS Cuprite data set after running the

Table 5.8: Execution times of HYCA and C-HYCA in the reconstruction of the AVIRIS Cuprite scene.

Algorithm	Time (secs)	Time/#pixels
HYCA	319.78	$6.662 \cdot 10^{-3}$
C-HYCA	303.78	$6.633 \cdot 10^{-3}$

algorithms during 200 iterations. This experiment was performed in a desktop computer Intel Core i7 920 CPU at 2.67 GHz with 4 GB of RAM. As shown by Table 5.8, both algorithms have similar complexity although C-HYCA outperforms in a few seconds the HYCA implementation.

5.5 Discussion

In this section we have provided experiments (using both synthetic and real hyperspectral data) that confirm our two main hypothesis in the present thesis work:

1. On the one hand, it has been found that spatial information can assist in the process of spectral unmixing under certain circumstances. However, the use or not of spatial information in spectral unmixing applications should be ultimately decided by the end-user, since there are certain scenarios in which the assumption that pure spectral signatures are often located in spatially homogeneous areas may not hold. For this reason, it is important that the incorporation of spatial information is performed as an optional step, tackled in this work by means of spatial pre-processing algorithms that do not require the modification of spectral-based techniques for unmixing hyperspectral data.

2. On the other hand, the dimensionality and size of remotely sensed hyperspectral images creates additional challenges that have been tackled in this work by means of compressive sensing strategies that use the concept of spectral unmixing and spatial information to provide a highly effective reconstruction of the hyperspectral data with almost no loss of the critical information that is needed for the analysis of the data. In this regard, there exists a strong relationship between compression and spectral unmixing since the information provided by unmixing (possibly complemented by spatial information) can be intelligently used to represent hyperspectral data in a very effective way.

Regarding our specific contributions in the area of spatial pre-processing prior to spectral unmixing, it has been shown that SPP is a simple, yet effective methodology which integrates both the spatial and the spectral information contained in the hyperspectral data in simultaneous fashion. The SPP allows one to incorporate spatial information into the traditional spectral-based endmember search conducted by standard algorithms, with the peculiarity that the algorithms used for endmember searching do not need to be modified. Instead, the proposed approach works as an (optional) spatial pre-processing module which can be applied to the original hyperspectral image prior

to the execution of an endmember extraction algorithm, thus allowing one to make use of the standard hyperspectral processing chain for spectral unmixing since this module works independently of other relevant modules of such chain, such as dimensionality reduction, endmember extraction or spectral unmixing.

Our experiments using both simulated and real data sets revealed that the SPP is quite promising in the sense that it can take advantage of spatial information in order to intelligently guide the traditional, spectral-based approach to extract endmembers from a hyperspectral scene, and also avoid that important endmembers are discarded during the process. The SPP has also several competitive advantages with regards to other available approaches for spatial-spectral integration. Most notably, the incorporation of spatial information in SPP does not degrade the spectral quality of the final endmembers. Another advantage is that the choice of the size and shape of the spatial context around each pixel vector is not a critical parameter requiring fine-tuning. Quite opposite, the only input parameter for spatial pre-processing is the size of a spatial window. This parameter is not critical for the final outcome due to its weighted implementation, but needs to be fine-tuned in order to achieve optimal performance.

In order to address the dependence of the SPP from the window size parameter, a new region-based spatial pre-processing technique called RBSPP has been combined with classic endmember extraction and spectral unmixing algorithms. Our experimental results have been discussed in terms of three criteria: 1) the spectral purity of extracted endmembers; 2) the capacity of such endmembers to produce an accurate reconstruction of the original hyperspectral image; and 3) the computational complexity of the considered algorithms. After analyzing these criteria we conclude that the RBSPP can assist in the selection of spectral endmembers which are more relevant in spatial sense without increasing the computational complexity. It is also observed in experiments that RBSPP is quite sensitive to noise present in the input data and the spatial and the spectral information is not equally weighted in the process.

To address the sensitivity to noise and the fact that spatial and spectral information are not equally treated in the RBSPP, we have developed a new spatial-spectral pre-processing (SSPP) method which can also be used prior to endmember identification and spectral unmixing of remotely sensed hyperspectral images. It considers spatial and spectral information simultaneously and fuses both sources of information at the pre-processing level. According to our experimentation, the SSPP exhibits the potential to improve the endmembers identified by algorithms designed with and without the pure signature assumption. Moreover, the SSPP can be combined (as a separate module) with any endmember identification algorithm without the need to modify such algorithm, and it does not increase (but often reduce) its computational complexity. In the case of endmember identification algorithms which are computationally very expensive, the proposed pre-processing allows for the application of these methods to real hyperspectral scenes in computationally tractable fashion.

Finally, taking advantage of the lessons learned after exploring the impact of spatial information in spectral unmixing, we have developed two new compressive sensing algorithms that allow for an efficient representation of hyperspectral data. Specifically,

it has been shown in experiments that HYCA framework takes advantage of two main properties of hyperspectral data, namely the high spatial correlation of abundance fractions and the low number of endmembers to explain the observed data. The former property is exploited by minimizing the total variation (TV) of the reconstructed images of abundance fractions and the latter property is exploited by formulating the reconstruction problem with respect to abundance fractions, which have much lower dimension than the original data. While HYCA depends on the tuning of a regularization parameter controlling the relative weight between the TV regularizer and the data term, C-HYCA does not depend on any regularization parameter. As demonstrated by our experiments with synthetic and real hyperspectral data, both approaches provide good results in the task of compressing remotely sensed hyperspectral data sets and are strongly related with the concept of spectral unmixing that has been widely used to interpret hyperspectral data.

Chapter 6

Conclusions and future lines

The incorporation of spatial information into the process of spectral unmixing of hyperspectral image data sets has been a long-awaited goal by the remote sensing community. Several well-known algorithms have been used for spectral unmixing by considering only the spectral properties of the data when conducting the search. However, there is a need to incorporate the spatial arrangement of the data in the development of endmember extraction and spectral unmixing algorithms. This is particularly the case in certain scenarios in which spatial information can help in modeling better the spectral variability observed in natural scenes, although in other scenarios spatial information may confuse the analysis and interpretation of the data. For this reason, it is very important that spatial information can be included *selectively*, by letting the end-user decide when such spatial information is relevant for the spectral unmixing process or not.

Another important problem in hyperspectral data management and interpretation is the sheer volume of data that hyperspectral images often comprise. At the same time, many applications require that the subtle details provided by the very fine spectral resolution are retained for subsequent analyses. Hence, the hyperspectral compression problem has found many challenges since high compression ratios and high fidelity in data reconstruction are often required. By realizing the importance of preserving spectral information, many efforts have been devoted to design and development of compression algorithms for hyperspectral imagery but very few of them have been based on the use of spectral unmixing principles in order to guide the compression process.

In this thesis work, we have address the two aforementioned problems and contributed several innovative algorithms that provide solutions to the specific problems mentioned above.

- One of the main contributions of this thesis work has been the development of new techniques for the incorporation of the spatial information in the hyperspectral unmixing process. The proposed spatial pre-processing techniques guide traditional spectral unmixing using spatial information and discard mixed and anomalous pixels which are more likely to represent outliers and noise. The specific new algorithms developed in this category have been the SPP, a spatial pre-processing framework based on fixed window sizes; the RBSPP, a region-based approach

which guides the process to those regions which are spatially homogeneous and spectrally pure; and the SSPP, a spatial-spectral method which calculates a spatial homogeneity factor and spectral purity index for each pixel, then fuses both spatial and spectral information by selecting those pixels which are located in spatially homogeneous regions and are spectrally pure.

- Another main contribution of this work is the development of a new framework for hyperspectral compressive sensing that uses hyperspectral unmixing in order to obtain a better reconstruction of the original image, so that (at the end of the reconstruction process) the hyperspectral image together with the endmembers and the fractional abundances can be obtained. As a result, the presented framework performs both spectral unmixing and compressive sensing in simultaneous fashion. The proposed framework makes use of the high spatial correlation generally present in hyperspectral scenes to obtain a better reconstruction, such that the incorporation of spatial information also allow for the obtainment of higher compression ratios. The specific new algorithms developed in this category are a hyperspectral coded aperture (HYCA) method which requires a parameter that needs to be fine-tuned, and a constrained version (C-HYCA) in which all the parameters can be calculated automatically, which represents an important contribution since reference information is generally difficult to obtain *a priori* in hyperspectral imaging.

For all developed algorithms, an exhaustive quantitative and comparative assessment has been performed in order to evaluate the accuracy and computational performance of these methods. The experiments have been conducted using both synthetic and real data, performing comparison with classic techniques available in the literature in order to substantiate the improvements and contributions of the newly proposed methods over the already existing ones. In the case of spectral unmixing techniques, we have evaluated the impact of spatial pre-processing over a variety of algorithms for endmember extraction (with and without the pure pixel assumption) and for abundance estimation. The results show some advantages of the inclusion of spatial information, in particular, when the noise level in the hyperspectral data is relatively high. These advantages are particularly apparent with the real hyperspectral data considered in experiments. Similarly, the newly developed compressive sensing algorithms have been extensively evaluated and it has been found that the reconstruction errors that they provide are very small even when the SNR is high, which makes these algorithms suitable in most hyperspectral imaging applications. Also, it is worth noting that the achieved compression ratios are very high (without losing spectral quality) by means of the intelligent exploitation of the spatial correlation present in hyperspectral images. This is an interesting observation, as our previous experience in the inclusion of spatial information in the spectral unmixing process also led us to develop a robust unmixing-based framework for data compression which can operate under extremely high compression rations (without sacrificing spectral quality) by means of the intelligent exploitation of spatial information. The result of this process is a framework that can perform spectral unmixing and compressive sensing

simultaneously and a general conclusion that the use of spatial information can help in the different hyperspectral image analysis tasks.

Another important consideration that should be highlighted for the newly developed methods is that their computational complexity is not very high. Although the spatial pre-processing methods introduce a new stage in the hyperspectral unmixing chain, in most cases this stage discards several pixels from the original hyperspectral data set and, as a result, there is a time saving in the subsequent processing stages that makes the spectral unmixing chain (with spatial pre-processing) even faster than the same chain without pre-processing. The same comments also apply in the context of compressive sensing, as our proposed framework is implemented using spectral unmixing chains considering spatial information. Furthermore the techniques developed in this thesis work are highly parallel in nature, which opens the door to future developments in the area of parallel implementation in high performance computing architectures such as clusters of computers, multi-core systems, graphics processing units (GPUs) or field programmable gate arrays (FPGAs), which represent suitable computing platforms to achieve spectral unmixing and compression of hyperspectral data in real time.

In addition to the computationally efficient implementation of the newly proposed algorithms in future developments, we are currently exploring the combination of spatial pre-processing with additional unmixing techniques (possibly non-linear). For the compressive sensing algorithms, currently we need the mixing matrix in order to get the final image reconstruction, but in some cases this mixing matrix is unknown in advance. To address this issue, a possible future research line could be the estimation of the mixing matrix from the compressed data in order to avoid the need to have the mixing matrix in advance in order to reconstruct the data. Currently, we are also working towards the inclusion of the HYCA and C-HYCA algorithms in our open-source tool HyperMix[1] [135, 136](see Fig. 6.1), which is also a main outcome of the present thesis work and already contains all the spatial pre-processing algorithms developed in this work, together with several algorithms comprising the different steps of the hyperspectral unmixing chain addressed in this work, as well as all the data sets used for experimental validation. This tool will allow interested readers to repeat our results and conduct additional experiments with full availability of our source codes and evaluation metrics, which are also available in the tool for evaluation purposes.

[1] http://www.hypercomp.es/hypermix

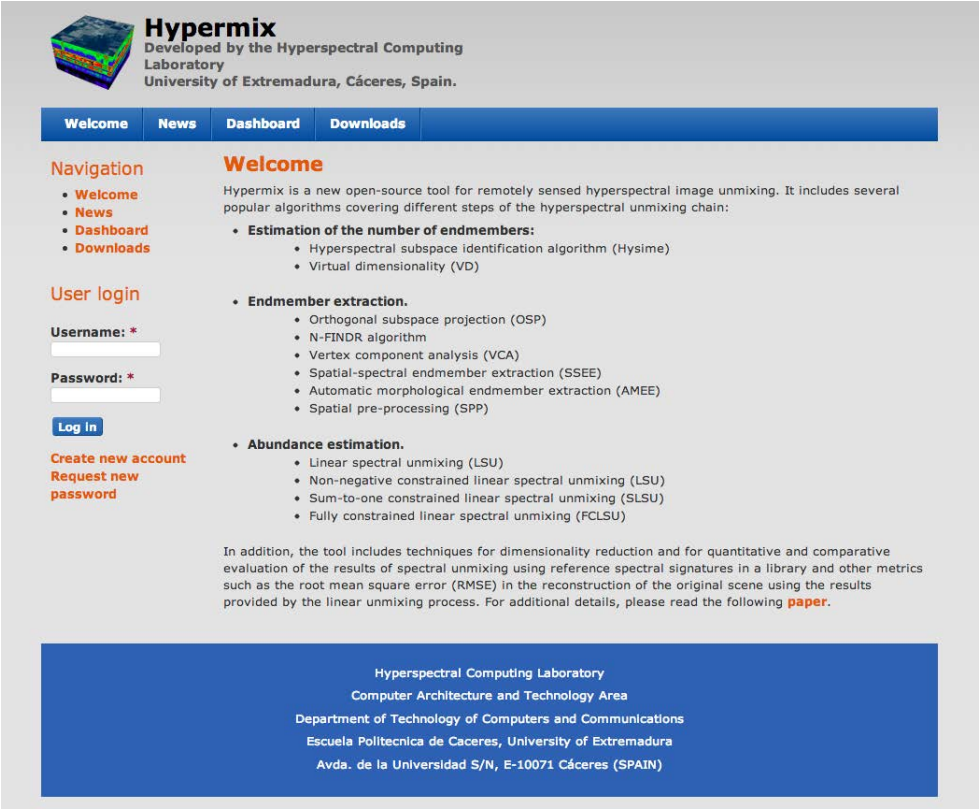

Figure 6.1: The HyperMix tool comprising most of the algorithms described in this chapter (available online: http://www.hypercomp.es/hypermix).

Apendix A

Alternating direction method of multipliers for HYCA and C-HYCA algorithms

We now introduce the details of our HYCA and C-HYCA algorithms. The optimization problem for HYCA can be written in the following equivalent form:

$$\min_{\mathbf{A}\geq 0} \quad \frac{1}{2}||\mathbf{Z}-\mathbf{K}(\mathbf{A})||_F^2 + \lambda_{TV}\mathrm{TV}(\mathbf{A}), \tag{A.1}$$

In (A.1), the first term measures the data misfit and the second term promotes piecewise smooth abundance images. From $\widehat{\mathbf{A}}$, the estimate of $\mathbf{A}$ in the matrix form, we infer the original hyperspectral data set by computing $\mathbf{M}\widehat{\mathbf{A}}$.

To solve the problem in Eq. (A.1), we follow closely the methodology introduced in [132]. The core idea is to introduce a set of new variables per regularizer and then use the alternating direction method of multipliers (ADMM) [133] to solve the resulting constrained optimization problem. By a careful choice of the new variables, the initial problem is converted into a sequence of much simpler problems. With this in mind, an equivalent way of writing the optimization problem in Eq. (A.1) is:

$$\min_{\mathbf{A}} \frac{1}{2}\|\mathbf{Z}-\mathbf{K}(\mathbf{A})\|_F^2 + \lambda_{TV}\|\mathbf{\Psi A}\|_{1,1} + \iota_{R+}(\mathbf{A}), \tag{A.2}$$

where:

$$\|\mathbf{\Psi A}\|_1 = \sum_{i=1}^{p}\mathrm{TV}(\mathbf{A}_i) := \mathrm{TV}(\mathbf{A}), \tag{A.3}$$

with $\mathbf{A}_i := \mathbf{A}(i,:)$ (matlab notation) is the ith image of representation coefficients with respect to matrix $\mathbf{M}$. Therefore, $\mathbf{\Psi}$ is the discrete gradient operating over the images $\mathbf{A}_i$, and $\iota_{R+}(\mathbf{A}) = \sum_{i=1}^{n}\iota_{R+}(\mathbf{a}_i)$ is the indicator function ($\mathbf{a}_i$ represents the i-th element of $\mathbf{A}$ and $\iota_{R+}(\mathbf{a}_i)$ is zero if $\mathbf{a}_i$ belongs to the nonnegative orthant and $+\infty$ otherwise). Given the objective function in Eq. (A.2), we write the following equivalent formulation:

$$\begin{aligned} \min_{\mathbf{A},\mathbf{V}_1,\mathbf{V}_2,\mathbf{V}_3,\mathbf{V}_4} \quad & \frac{1}{2}||\mathbf{Y}-\mathbf{K}(\mathbf{V}_1)||_F^2 + \iota_{R+}(\mathbf{V}_2) + \lambda_{TV}||(\mathbf{V}_3,\mathbf{V}_4)||_1 \\ \text{subject to} \quad & \mathbf{A}=\mathbf{V}_1 \\ & \mathbf{A}=\mathbf{V}_2 \\ & \mathbf{\Psi A}=(\mathbf{V}_3,\mathbf{V}_4) \end{aligned} \tag{A.4}$$

Which in compact form becomes:

$$\min_{\mathbf{A},\mathbf{V}} g(\mathbf{V}) \text{ subject to } \mathbf{GA}+\mathbf{BV}=\mathbf{0}, \tag{A.5}$$

where:

$$\begin{aligned} &\mathbf{V} \equiv (\mathbf{V}_1,\mathbf{V}_2,\mathbf{V}_3,\mathbf{V}_4), \\ &g(\mathbf{V}) \equiv \frac{1}{2}||\mathbf{Z}-\mathbf{K}(\mathbf{V}_1)||_F^2 + \iota_{R+}(\mathbf{V}_2) + \lambda_{TV}||(\mathbf{V}_3,\mathbf{V}_4)||_1 \end{aligned} \tag{A.6}$$

and:

$$\mathbf{G}=\begin{bmatrix}\mathbf{I}\\ \mathbf{I}\\ \mathbf{\Psi}\end{bmatrix}, \qquad \mathbf{B}=\begin{bmatrix}-\mathbf{I} & \mathbf{0} & \mathbf{0}\\ \mathbf{0} & -\mathbf{I} & \mathbf{0}\\ \mathbf{0} & \mathbf{0} & -\mathbf{I}\end{bmatrix}.$$

Algorithm 1 Alternating direction method of multipliers (ADMM) pseudocode for solving problem (A.5).

1. **Initialization**: set $k=0$, choose $\mu>0$, $\mathbf{A}^{(0)}$, $\mathbf{V}^{(0)}$, $\mathbf{D}^{(0)}$
2. **repeat:**
3. $\mathbf{A}^{(k+1)} \leftarrow \arg\min_{\mathbf{A}} \mathcal{L}(\mathbf{A}^{(k)},\mathbf{V}^{(k)},\mathbf{D}^{(k)})$
4. $\mathbf{V}^{(k+1)} \leftarrow \arg\min_{\mathbf{v}} \mathcal{L}(\mathbf{A}^{(k+1)},\mathbf{V}^{(k)},\mathbf{D}^{(k)})$
5. $\mathbf{D}^{(k+1)} \leftarrow \mathbf{D}^{(k)} - \mathbf{GA}^{(k+1)} - \mathbf{BV}^{(k+1)}$
6. **until** some stopping criterion is satisfied.

The ADMM algorithm for the formulation (A.5) is shown in Algorithm 1, where (see [132], [137]):

$$\mathcal{L}(\mathbf{A},\mathbf{V},\mathbf{D}) \equiv g(\mathbf{A},\mathbf{V}) + \frac{\mu}{2}\|\mathbf{GA}+\mathbf{BV}-\mathbf{D}\|_F^2, \tag{A.7}$$

is the augmented Lagrangian for problem (A.5), $\mu>0$ is a positive constant, and $\mathbf{D}/\mu$ denotes the Lagrange multipliers associated to the constraint $\mathbf{GA}+\mathbf{BV}=\mathbf{0}$. In each iteration, Algorithm 1 sequentially optimizes $\mathcal{L}$ with respect to $\mathbf{A}$ (step 3) and $\mathbf{V}$ (step 4), and then updates the Lagrange multipliers (step 5).

If we expand the augmented Lagrangian introduced in (A.7) we obtain:

$$\begin{aligned} &\mathcal{L}(\mathbf{A},\mathbf{V}_1,\mathbf{V}_2,\mathbf{V}_3,\mathbf{V}_4,\mathbf{D}_1,\mathbf{D}_2,\mathbf{D}_3,\mathbf{D}_4) = \\ &\quad \frac{1}{2}||\mathbf{Z}-\mathbf{K}(\mathbf{V}_1)||_F^2 + \iota_{R+}(\mathbf{V}_2) + \lambda_{TV}||(\mathbf{V}_3,\mathbf{V}_4)||_1 + \frac{\mu}{2}\|\mathbf{A}-\mathbf{V}_1-\mathbf{D}_1\|_F^2 + \\ &\quad \frac{\mu}{2}\|\mathbf{A}-\mathbf{V}_2-\mathbf{D}_2\|_F^2 + \frac{\mu}{2}\|\mathbf{\Psi}_h\mathbf{A}-\mathbf{V}_3-\mathbf{D}_3\|_F^2 + \frac{\mu}{2}\|\mathbf{\Psi}_h\mathbf{A}-\mathbf{V}_4-\mathbf{D}_4\|_F^2 \end{aligned} \tag{A.8}$$

where $\mathbf{\Psi}_h$ and $\mathbf{\Psi}_v$ denotes the operator which computes the horizontal and vertical differences respectively.

The pseudocode of HYCA is shown in Algorithm 2. It is the expansion of the ADDM algorithm presented in Algorithm 1.

Algorithm 2 Pseudocode of the HYCA algorithm.

1. Initialization: set $k = 0$, choose $\mu \geq 0$,$\mathbf{A^{(0)}}$, $\mathbf{V}_1^{(0)}$,$\mathbf{V}_2^{(0)}$,$\mathbf{V}_3^{(0)}$,$\mathbf{V}_4^{(0)}$,$\mathbf{D}_1^{(0)}$,$\mathbf{D}_2^{(0)}$,$\mathbf{D}_3^{(0)}$,$\mathbf{D}_4^{(0)}$

2. repeat:

3. $\mathbf{A}^{(k+1)} \leftarrow \arg\min_{\mathbf{A}} \mathcal{L}(\mathbf{A}, \mathbf{V}_1^{(k)}, \mathbf{V}_2^{(k)}, \mathbf{V}_3^{(k)}, \mathbf{V}_4^{(k)}, \mathbf{D}_1^{(k)}, \mathbf{D}_2^{(k)}, \mathbf{D}_3^{(k)}, \mathbf{D}_4^{(k)})$

4. $\mathbf{V}_1^{(k+1)} \leftarrow \arg\min_{\mathbf{V}_1} \mathcal{L}(\mathbf{A}^{(k)}, \mathbf{V}_1, \mathbf{V}_2^{(k)}, \mathbf{V}_3^{(k)}, \mathbf{V}_4^{(k)})$

5. $\mathbf{V}_2^{(k+1)} \leftarrow \arg\min_{\mathbf{V}_2} \mathcal{L}(\mathbf{A}^{(k)}, \mathbf{V}_1^{(k)}, \mathbf{V}_2, \mathbf{V}_3^{(k)}, \mathbf{V}_4^{(k)})$

6. $\mathbf{V}_3^{(k+1)} \leftarrow \arg\min_{\mathbf{V}_3^{(k)}} \mathcal{L}(\mathbf{A}^{(k)}, \mathbf{V}_1^{(k)}, \mathbf{V}_2^{(k)}, \mathbf{V}_3, \mathbf{V}_4^{(k)})$

6. $\mathbf{V}_4^{(k+1)} \leftarrow \arg\min_{\mathbf{V}_4^{(k)}} \mathcal{L}(\mathbf{A}^{(k)}, \mathbf{V}_1^{(k)}, \mathbf{V}_2^{(k)}, \mathbf{V}_3^{(k)}, \mathbf{V}_4)$

7. Update Lagrange multipliers:

$\mathbf{D}_1^{(k+1)} \leftarrow \mathbf{D}_1^{(k)} - \mathbf{A}^{(k+1)} + \mathbf{V}_1^{(k+1)}$

$\mathbf{D}_2^{(k+1)} \leftarrow \mathbf{D}_2^{(k)} - \mathbf{A}^{(k+1)} + \mathbf{V}_2^{(k+1)}$

$\mathbf{D}_3^{(k+1)} \leftarrow \mathbf{D}_3^{(k)} - \mathbf{\Psi}_h\mathbf{A}^{(k+1)} + \mathbf{V}_3^{(k+1)}$

$\mathbf{D}_4^{(k+1)} \leftarrow \mathbf{D}_4^{(k)} - \mathbf{\Psi}_v\mathbf{A}^{(k+1)} + \mathbf{V}_4^{(k+1)}$

8. Update iteration: $k \leftarrow k + 1$

9. until some stopping criterion is satisfied.

The goal of the Step 3 in Algorithm 2 is to determine the value of the variable $\mathbf{A}$ at each iteration. Given that we run an optimization over the variable $\mathbf{A}$, the terms of the objective function (A.8) which do no contain this variable are not taken into account. The reduced optimization function becomes, then:

$$\mathbf{A}^{(k+1)} \leftarrow \arg\min_{\mathbf{A}} \frac{\mu}{2}\|\mathbf{A} - \mathbf{V}_1 - \mathbf{D}_1\|_F^2 + \frac{\mu}{2}\|\mathbf{A} - \mathbf{V}_2 - \mathbf{D}_2\|_F^2 + \frac{\mu}{2}\|\mathbf{\Psi}_h\mathbf{A} - \mathbf{V}_3 - \mathbf{D}_3\|_F^2 + \frac{\mu}{2}\|\mathbf{\Psi}_v\mathbf{A} - \mathbf{V}_4 - \mathbf{D}_4\|_F^2 \tag{A.9}$$

The minimization of the augmented Lagrangian with respect to $\mathbf{A}$ is a quadratic problem with a block cyclic system matrix, thus effectively solved in the Fourier domain:

$$\mathbf{A}^{(k+1)} \leftarrow (\mathbf{\Psi}_{\boldsymbol{h}}^T\mathbf{\Psi}_{\boldsymbol{h}} + \mathbf{\Psi}_{\boldsymbol{v}}^T\mathbf{\Psi}_{\boldsymbol{v}} + 2\mathbf{I})^{-1}(\xi_1 + \xi_2 + \mathbf{\Psi}_h\xi_3 + \mathbf{\Psi}_v\xi_3), \tag{A.10}$$

where $\xi_1 = \mathbf{V}_1^{(k)} + \mathbf{D}_1^{(k)}$, $\xi_2 = \mathbf{V}_2^{(k)} + \mathbf{D}_2^{(k)}$, $\xi_3 = \mathbf{V}_3^{(k)} + \mathbf{D}_3^{(k)}$, $\xi_4 = \mathbf{V}_4^{(k)} + \mathbf{D}_4^{(k)}$.

Steps 4–6 of HYCA compute the minimization of the augmented Lagrangian with respect to $\mathbf{V}$, which is decoupled with respect to $\mathbf{V}_1$, $\mathbf{V}_2$ and $(\mathbf{V}_3, \mathbf{V}_4)$. The minimization with respect to $\mathbf{V}_1$ is a quadratic problem involving the inverse of the operator $(\mathbf{K}^T\mathbf{K} + \mu\mathbf{I})$ ($\mathbf{I}$ stands for identity operator) which, given the structure of the linear operator $\mathbf{H}$, can be precomputed. To compute $\mathbf{V}_1$, the optimization problem to be solved is:

$$\mathbf{V}_1^{(k+1)} \leftarrow \arg\min_{\mathbf{V}_1} \frac{1}{2}||\mathbf{Z} - \mathbf{K}(\mathbf{V}_1)||_F^2 + \frac{\mu}{2}\|\mathbf{A} - \mathbf{V}_1 - \mathbf{D}_1\|_F^2 \tag{A.11}$$

whose solution is:

$$\mathbf{V}_1^{(k+1)} \leftarrow \left(\mathbf{K}^T\mathbf{K} + \mu\mathbf{I}\right)^{-1}[\mathbf{K}^T\mathbf{Z} + \mu(\mathbf{A}^k - \mathbf{D}_1)] \tag{A.12}$$

To compute $\mathbf{V}_2$, the optimization problem to be solved is:

$$\mathbf{V}_2^{(k+1)} \leftarrow \arg\min_{\mathbf{V}_2} \iota_{R+}(\mathbf{V}_2) + \frac{\mu}{2}\|\mathbf{A} - \mathbf{V}_2 - \mathbf{D}_2\|_F^2 \tag{A.13}$$

In (A.13), the role of the ι_{R+} term is to project the solution onto the nonnegative orthant and the value of $\mathbf{V}_2$ is given by:

$$\mathbf{V}_2^{(k+1)} \leftarrow \max(0, \mathbf{A} - \mathbf{D}_2), \tag{A.14}$$

Finally the minimization with respect to $(\mathbf{V}_3, \mathbf{V}_4)$ is carried out by a block minimization with respect to $\mathbf{V}_3$ and to $\mathbf{V}_4$. In order to compute $\mathbf{V}_3$ and $\mathbf{V}_4$, we solve the optimization problem:

$$\mathbf{V}_3^{(k+1)}, \mathbf{V}_4^{(k+1)} \leftarrow \arg\min_{\mathbf{V}_3, \mathbf{V}_3} \lambda_{TV}||(\mathbf{V}_3, \mathbf{V}_4)||_1 + \frac{\mu}{2}\|\mathbf{\Psi}_h\mathbf{A} - \mathbf{V}_3 - \mathbf{D}_3\|_F^2 + \frac{\mu}{2}\|\mathbf{\Psi}_h\mathbf{A} - \mathbf{V}_4 - \mathbf{D}_4\|_F^2 \tag{A.15}$$

whose solution is the well-known *vect–soft threshold* (see, *e.g.*, [138]), applied independently to each variable:

$$\mathbf{V}_3^{(k+1)} \leftarrow \text{vect-soft}(\mathbf{A} - \mathbf{D}_3, \lambda_{TV}/\mu), \tag{A.16}$$

$$\mathbf{V}_4^{(k+1)} \leftarrow \text{vect-soft}(\mathbf{z} - \mathbf{D}_4, \lambda_{TV}/\mu), \tag{A.17}$$

where vect–soft$(\cdot, \tau)$ denotes the row-wise application of the vect–soft-threshold function $\mathbf{b} \mapsto \frac{\max\{\|\mathbf{x}\|_2 - \tau, 0\}}{\max\{\|\mathbf{x}\|_2 - \tau, 0\} + \tau}$.

The convergence conditions from [133, Theorem 1] are met: matrix $\mathbf{G}$ is full column rank and function g introduced in (A.5) is closed, proper, and convex. Under these conditions, the same theorem states that, for any $\mu > 0$, if (A.5) has a solution, say $\mathbf{A}^*$, then the sequence $\{\mathbf{A}^{(k)}\}$ converges to $\mathbf{A}^*$. If (A.5) does not have a solution, then at least one of the sequences $\{\mathbf{A}^{(k)}\}$ or $\{\mathbf{D}^{(k)}\}$ diverges. The stopping criterion adopted in the algorithm is $k = 200$.

In the ADMM scheme, the setting of the parameter μ has a strong impact over the convergence speed. In our case we set the μ parameter by hand using a wide range of values for optimal performance.

Similarly in the case of C-HYCA we also used the ADMM methodology to solve the C-HYCA minimization problem:

$$\min_{\mathbf{A} \geq 0} \text{TV}(\mathbf{A}) \quad \text{subject to:} \quad \|\mathbf{Z} - \mathbf{K}(\mathbf{A})\|_F^2 \leq \sigma, \tag{A.18}$$

where σ is a scalar value linked to the noise statistics.

As have been done before in the case of HYCA here we also introduce a set of new variables per term of the objective function and then use the alternating direction method

of multipliers (ADMM) [133] described above to solve the resulting convex constrained optimization problem. By a careful choice of the new variables, the initial problem is converted into a sequence of much simpler problems. With this in mind, let's define $\iota_{B(\epsilon)}$ as the indicator on a ball of radius ϵ, i.e., $\iota_{B(\epsilon)}(\mathbf{A}) = 0$ if $\|\mathbf{A}\|_F \leq \varepsilon$ and $+\infty$ otherwise. With these definition in place, an equivalent way of writing the optimization problem in (A.18) is

$$\min_{\mathbf{A}} \|\mathbf{\Psi A}\|_{1,1} + \iota_{B(\sigma)}(\mathbf{Z} - \mathbf{K}(\mathbf{A})) + \iota_{R+}(\mathbf{A}). \tag{A.19}$$

Given the objective function in (A.19), we write the following convex constrained equivalent formulation:

$$\begin{aligned} \min_{\mathbf{A},\mathbf{V}_1,\mathbf{V}_2,\mathbf{V}_3,\mathbf{V}_5} \quad & ||\mathbf{V}_1, \mathbf{V}_2||_1 + \iota_{B(\sigma)}(\mathbf{V}_3) + \iota_{R+}(\mathbf{V}_5) \\ \text{subject to:} \quad & \mathbf{\Psi A} = (\mathbf{V}_1, \mathbf{V}_2) \\ & \mathbf{A} = \mathbf{V}_4 \\ & \mathbf{Z} - \mathbf{K}(\mathbf{V}_4) = \mathbf{V}_3 \\ & \mathbf{A} = \mathbf{V}_5 \end{aligned} \tag{A.20}$$

which we solve via ADMM as described before in 1, but here note that we have to introduce the new variables $\mathbf{V}_5$ and $\mathbf{D}_5$.

If we expand the augmented Lagrangian in this case we obtain:

$$\begin{aligned} &\mathcal{L}(\mathbf{A}, \mathbf{V}_1, \mathbf{V}_2, \mathbf{V}_3, \mathbf{V}_4, \mathbf{V}_5, \mathbf{D}_1, \mathbf{D}_2, \mathbf{D}_3, \mathbf{D}_4, \mathbf{D}_5) = \\ &\quad ||\mathbf{V}_1, \mathbf{V}_2||_1 + \frac{\mu}{2}\|\mathbf{\Psi}_h\mathbf{A} - \mathbf{V}_1 - \mathbf{D}_1\|_F^2 + \frac{\mu}{2}\|\mathbf{\Psi}_v\mathbf{A} - \mathbf{V}_2 - \mathbf{D}_2\|_F^2 + \\ &\quad \iota_{B(\sigma)}(\mathbf{V}_3) + \frac{\mu}{2}\|\mathbf{V}_3 - (\mathbf{Z} - \mathbf{K}(\mathbf{V}_4)) - \mathbf{D}_3\|_F^2 + \frac{\mu}{2}\|\mathbf{A} - \mathbf{V}_4 - \mathbf{D}_4\|_F^2 \end{aligned} \tag{A.21}$$

The minimization of the augmented Lagrangian with respect to $\mathbf{A}$ is a quadratic problem with a block cyclic system matrix, thus effectively solved in the Fourier domain:

$$\mathbf{A}^{(k+1)} \leftarrow (\mathbf{\Psi}_{\boldsymbol{h}}^T\mathbf{\Psi}_{\boldsymbol{h}} + \mathbf{\Psi}_{\boldsymbol{v}}^T\mathbf{\Psi}_{\boldsymbol{v}} + 2\mathbf{I})^{-1}(\mathbf{\Psi}_h\xi_1 + \mathbf{\Psi}_v\xi_2 + \xi_4 + \xi_5), \tag{A.22}$$

where $\xi_1 = \mathbf{V}_1^{(k)} + \mathbf{D}_1^{(k)}$, $\xi_2 = \mathbf{V}_2^{(k)} + \mathbf{D}_2^{(k)}$, $\xi_4 = \mathbf{V}_4^{(k)} + \mathbf{D}_4^{(k)}$, $\xi_5 = \mathbf{V}_5^{(k)} + \mathbf{D}_5^{(k)}$.

The minimization with respect to $(\mathbf{V}_1, \mathbf{V}_2)$ is carried out by a block minimization with respect to $\mathbf{V}_1$ and to $\mathbf{V}_2$. whose solution is the well-known *vect–soft threshold*, applied independently to each variable:

$$\mathbf{V}_1^{(k+1)} \leftarrow \text{vect-soft}(\mathbf{A} - \mathbf{D}_1, 1/\mu), \tag{A.23}$$

$$\mathbf{V}_2^{(k+1)} \leftarrow \text{vect-soft}(\mathbf{A} - \mathbf{D}_2, 1/\mu), \tag{A.24}$$

The minimization with respect to $\mathbf{V}_3$ is a projection on a ball of radius σ:

$$\begin{aligned} &\text{if } \|\xi_3\| \leq \sigma \text{ then } \mathbf{V}_1^{(k+1)} \leftarrow \xi_3, \\ &\quad \text{otherwise } \mathbf{V}_1^{(k+1)} \leftarrow \frac{\sigma\xi_3}{\|\xi_3\|_F}, \end{aligned} \tag{A.25}$$

where $\xi_3 = \mathbf{Z} - \mathbf{K}(\mathbf{V}_4) + \mathbf{D}_3$.

The minimization with respect to V_4 is a quadratic problem involving the inverse of the operator $(\mathbf{K}^T\mathbf{K} + \mu\mathbf{I})$ ($\mathbf{I}$ stands for identity operator) which, given the structure of the linear operator $\mathbf{H}$, can be precomputed.

$$\mathbf{V}_4^{(k+1)} \leftarrow (\mathbf{K}^T\mathbf{K} + \mu\mathbf{I})^{-1}[(\mathbf{A} - \mathbf{D}_4) + \mathbf{K}^T(-\mathbf{V}_3 + \mathbf{Z} + \mathbf{D}_1)]. \tag{A.26}$$

Finally, the the minimization with respect to $\mathbf{V}_5$ is a componentwise projection on the nonnegative orthant and the value of $\mathbf{V}_5$ is given by:

$$\mathbf{V}_5^{(k+1)} \leftarrow \max(0, \mathbf{A} - \mathbf{D}_5), \tag{A.27}$$

As we can see in this case it is not neccesary the λ_{TV} parameter and we need to estimate the σ parameter instead, which can be estimated automatically due to it is linked to the noise statistics of the image.

Apendix B

Publications

The results of this thesis work have been published in several international journal papers, book chapters and peer-reviewed international conference papers. Specifically, the applicant has co-authored 7 JCR journal papers (6 of which are already published and one under revision), 2 book chapters and 18 international peer-reviewed conference papers directly related with this thesis work. This theis work have been supported by the National Program for Research Staff Formation "Programa de Formacion de Personal Investigador (FPI)" of the Spanish Ministry of Science and Innovation. The candidate has been an pre-doctoral researcher in the Department of Computer and Communications in the University of Extremadura, forming part of the research group "Hyperspectral Computing Laboratory" (HyperComp) of the University of Extremadura during four years. During the development of the thesis, the candidate has been a visitor (for a total of 11 months) with the Pattern and Image Analysis Group, Instituto de Telecomunicações, Instituto Superior Técnico, Lisbon, Portugal. In the following we describe the publications achieved by the candidate, providing also a short description of the journal or conference where it was presented and and indication of the specific contributions of the candidate to each publication.

B.1 International journal papers

1. G. Martin, J. M. Bioucas-Dias and A. Plaza. Hyperspectral coded aperture (HYCA): A New Technique for Hyperspectral Compressive Sensing. *IEEE Transactions on Geoscience and Remote Sensing*, submitted [JCR(2012)=2.985]. This paper has been submitted to the *IEEE Transactions on Geoscience and Remote Sensing* which is a Q1 journal in the area of electrical engineering and the most important journal in the technology of remote sensing. The paper describes the HYCA and C-HYCA methods described in this thesis work. The paper also includes an extensive evaluation these methods in terms of accuracy and computational performance. The candidate contributed the implementation of both methods and also the development of all experiments presented in the paper. This work was carried out in collaboration with experts from the Instituto Superior

Técnico, Lisbon, Portugal.

2. G. Martin and A. Plaza. Spatial-Spectral Preprocessing Prior to Endmember Identification and Unmixing of Remotely Sensed Hyperspectral Data. *IEEE Journal of Selected Topics in Applied Earth Observations and Remote Sensing*, vol. 5, no. 2, pp. 380-395, April 2012 [JCR(2011)=1.489]. This paper was published in the journal *IEEE Journal of Selected Topics in Applied Earth Observations and Remote Sensing* which is a Q2 journal in the area of electrical engineering. The paper describes the SSPP method described in this thesis work. The paper also includes a comparison between the SSPP method and other endmember extraction methods which reveals the great potential of spatial pre-processing techniques in order to improve the accuracy and computational performance of endmember extraction and spectral unmixing algorithms. The candidate contributed the design and implementation of the SSPP method and also the development of all experiments in the method comparison.

3. E. M. T. Hendrix, I. Garcia, J. Plaza, G. Martin and A. Plaza. A New Minimum Volume Enclosing Algorithm for Endmember Identification and Abundance Estimation in Hyperspectral Data. *IEEE Transactions on Geoscience and Remote Sensing*, vol. 50, no. 7, pp. 2744-2757, July 2012 [JCR(2011)=2.895]. This paper was published in the journal *IEEE Transactions on Geoscience and Remote Sensing*, which is a Q1 journal in the area of electrical engineering and the most important journal in the technology of remote sensing. The paper develops a new endmember extraction technique without the pure pixel assumption which uses a minimum volume approach in order to estimate de endmembers from the original data set without assuming that the endmembers are present in the data. The candidate contributed the experiments comparing the algorithm with other standard approaches for endmember extraction and spectral unmixing algorithms using both real and synthetic fractals data. This work was carried out in collaboration with experts from the University of Malaga.

4. J. Plaza, E. M. T. Hendrix, I. Garcia, G. Martin and A. Plaza. On Endmember Identification in Hyperspectral Images without Pure Pixels: A Comparison of Algorithms. *Journal of Mathematical Imaging and Vision*, vol. 42, no. 2-3, pp. 163-175, February 2012 [JCR(2011)=1.391]. This paper was published in the *Journal of Mathematical Imaging and Vision* which is a Q1 journal in the area of applied mathematics and a Q1 journal in the area of computer science, and software engineering. This work develops a comparative assessment of different methods for endmember extraction and spectral unmixing, with and without the pure pixel assumption. The candidate contributed the development of the database of synthetic images used in the comparison and also the development of all experiments in the method comparison. This work was carried out in collaboration with experts from the University of Malaga.

5. S. Sanchez, A. Paz, G. Martin and A. Plaza. Parallel Unmixing of Remotely Sensed

Hyperspectral Images on Commodity Graphics Processing Units. *Concurrency and Computation: Practice & Experience*, vol. 23, no. 13, pp. 1538-1557, September 2011 [JCR(2009)=1.004]. This work was published in the journal *Concurrency and computation: Practice and experience* which is a Q2 journal in the field computer science, software engineering. The paper describes a comparison for different implementations of hyperspectral analysis algorithms developed for graphics processing units (GPUs). The candidate provided support in the GPU design and implementation of spectral unmixing algorithms and also helped obtaining the results presented in the comparison.

6. G. Martin and A. Plaza. Region-Based Spatial Preprocessing for Endmember Extraction and Spectral Unmixing. *IEEE Geoscience and Remote Sensing Letters*, vol. 8, no. 4, pp. 745-749, July 2011 [JCR(2011)=1.560]. This paper was published in the journal *IEEE Geoscience and Remote Sensing Letters*, which is a Q1 journal in the area of electrical engineering. This paper describes the RBSPP method presented in the thesis, along with a comparison of the RBSPP algorithm in combination with other endmember extraction algorithms that assume the presence of pure pixels. The paper presents results with the synthetic fractal images database and also with the real AVIRIS Cuprite dataset. The candidate contributed the design and implementation of the RBSPP algorithm and also the development of all experiments in the method comparison.

7. G. Martin, V. Gonzalez-Ruiz, A. Plaza, J. P. Ortiz and I. Garcia. Impact of JPEG2000 Compression on Endmember Extraction and Unmixing of Remotely Sensed Hyperspectral Data. *Journal of Applied Remote Sensing*, vol. 4, Article ID 041796, 24 pages, July 2010 [JCR(2010)=1.000]. This paper was published in the *Journal of Applied Remote Sensing* which is a Q3 journal in the areas of remote sensing and imaging science and photographic technology. This paper presents a study of how lossy compressions impacts the outcome of spectral unmixing applications, and was crucial for the development of the compressive sensing techniques described in this work. The study analyzes the impact of compression on several endmember extraction techniques such as AMEE, OSP, NFINDR and SSEE that were applied to images compressed with the JPEG2000 format with different compression ratios. The candidate contributed the design and implementation of the algorithms compared in this work and also the development of all experiments in the method comparison.

B.2 Book chapters

1. A. Plaza, J. Plaza, G. Martin and S. Sanchez. Hyperspectral Data Processing Algorithms, in: Hyperspectral Remote Sensing of Vegetation. Edited by P. S. Thenkabail, J. G. Lyon and A. Huete, Taylor & Francis, 2011, ISBN: 9781439845370, pp. 121-137. This chapters includes an analysis of several techniques for hyperspectral image processing, with particular focus on spectral

unmixing techniques (both linear and non-linear). The candidate contributed with the development of several spectral unmixing and endmember extraction techniques that were used in the experimental results. Also the candidate performed all the experiments related with linear spectral unmixing techniques.

2. A. Plaza, G. Martin, J. Plaza, M. Zortea and S. Sanchez. Recent Developments in Spectral Unmixing and Endmember Extraction, in: Optical Remote Sensing - Advances in Signal Processing and Exploitation Techniques. Edited by S. Prasad, L. Bruce and J. Chanussot, Springer, 2011, ISBN: 978-3-642-1241-6, pp. 235-268. The chapter provide an overview of existing techniques for spectral unmixing and endmember extraction, with particular attention paid to recent advances in the field such as the incorporation of spatial information into the endmember searching process, or the use of nonlinear mixture models for fractional abundance characterization. The candidate contributed with the development of several spectral unmixing and endmember extraction techniques that were used in the experimental results. The candidate performed all the experiments involving linear spectral unmixing techniques.

B.3 Peer-reviewed international conference papers

1. G. Martin, J. Bioucas-Dias and A. Plaza. Hyperspectral Coded Aperture: A New Technique for Hyperspectral Unmixing. *European Signal Processing Conference (EUSIPCO'2013)*, Marrakesch, Morocco, 2013. This work has been submitted to the workshop *EUSIPCO* in 2013. In this workshop, the HYCA and C-HYCA methods are presented to the signal processing community and the contribution of the applicant was the implementation of these methods and the developments of all the experimental validation results analyzing the performance of both methods with synthetic and real hyperspectral scenes.

2. L. I. Jimenez, G. Martin and A. Plaza. HyperMix: A New Tool for Quantitative Evaluation of Endmember Identification and Spectral Unmixing Techniques. *IEEE Geoscience and Remote Sensing Symposium (IGARSS'2012)*, Munich, Germany, 2012. This work was presented as an oral presentation in the workshop *IGARSS* in 2012. This workshop is attended by thousands of researchers worldwide in the remote sensing field, and it is the most international important workshop in the remote sensing area. In this work we presented a new open source tool for hyperspectral unmixing called HyperMix, which was developed by the HyperComp research group and which contains many of the algorithms discussed in this thesis. The contribution of the canddidate was the development of several endmember extraction techniques such as OSP, NFINDR, AMEE, SPP and SSEE using the open source library Orfeo Toolbox for the inclusion in the HyperMix tool.

3. G. Martin, J. Bioucas-Dias and A. Plaza. Hyperspectral Coded Aperture: A New Algorithm for Hyperspectral Compressive Sensing. *IEEE Geoscience and Remote Sensing Symposium (IGARSS'2012)*, Munich, Germany, 2012. This work was

presented as an oral presentation in the workshop *IGARSS* in 2012. This workshop is attended by thousands of researchers worldwide in the remote sensing field, and it is the most international important workshop in the remote sensing area. In this work we presented the new HYCA algorithm, which has been developed in the framework of this thesis work. The contribution of the applicant was the implementation of the HYCA method and the development of all the experimental validation results analyzing the performance of this method with synthetic and real hyperspectral scenes.

4. G. Martin, J. Bioucas-Dias and A. Plaza. A New Technique for Hyperspectral Compressive Sensing Using Spectral Unmixing. *SPIE Optics and Photonics, Satellite Data Compression, Communication, and Processing Conference*, San Diego, CA, 2012. This work was presented in an oral presentation in the workshop *SPIE Optics and Photonics*. This workshop is attended by thousands of researchers worldwide in the remote sensing field, and it is one of the most international important workshop in the remote sensing area. In this work we presented the constrained version of HYCA algorithm (C-HYCA) discussed in this thesis work. The contribution of the applicant was the implementation of the C-HYCA method and the development of all the experimental validation results analyzing the performance of this method with synthetic and real hyperspectral scenes.

5. G. Martin, L. I. Jimenez and A. Plaza. A New Tool for Evaluating Spectral Unmixing Applications for Remotely Sensed Hyperspectral Image Analysis. *International Conference on Geographic Object-Based Image Analysis (GEOBIA)*, Rio de Janeiro, Brazil, 2012. This work was presented in *GEOBIA'2012* in Rio de Janeiro in 2012, which is a workshop in which students and interested users presented their latest research and results related with geo-information data processing. In this workshop we presented the HyperMix tool for hyperspectral image analysis and processing, developed as an Open Source tool using the Orfeo ToolBox library. The paper also presents a quantitative assessment of the accuracy and computational performance of the algorithms included in the HyperMix tool with the synthetic fractal images and also with the real AVIRIS Cuprite dataset. The cnadidate contributed the development of several algorithms included in the HyperMix tool. The candidate also assisted in the design and development of the tool.

6. G. Martin, J. Plaza and A. Plaza. On the Incorporation of Spatial Information to Endmember Identification Algorithms without the Pure Pixel Assumption. *IEEE GRSS Workshop on Hyperspectral Image and Signal Processing: Evolution in Remote Sensing (WHISPERS'11)*, Lisbon, Portugal, 2011. This work was presented as an oral presentation in the *IEEE WHISPERS* which is one of the most important international workshops specialized in hyperspectral remote sensing. In this work we presented a comparative assessment of the spatial pre-processing techniques SPP and RBSPP in combination with endmember extraction techniques that do not assume the presence of pure pixels such as SISAL and MVSA. The

results presented in this workshop are included in this thesis work. The contribution of the candidate was the development of the RBSPP algorithm and also the experimental results which were entirely produced by the candidate.

7. G. Martin and A. Plaza. Joint Spectral and Spatial Preprocessing Prior to Endmember Extraction from Hyperspectral Images. *SPIE Optics and Photonics, Satellite Data Compression, Communication, and Processing Conference*, San Diego, CA, 2011. This work was presented in an oral presentation in the workshop *SPIE Optics and Photonics*. This workshop is attended by thousands of researchers worldwide in the remote sensing field, and it is one of the most international important workshop in the remote sensing area. The paper presents a new technique for spatial preprocessing corresponding to the first steps of the design of the SSPP technique. The candidate contributed with the development and design of the new preprocessing technique and also performed all the experiments for the comparative assessment with the fractal synthetic image database and also with the real image of Cuprite.

8. G. Martin, A. Plaza and M. Zortea. Noise-Robust Spatial Preprocessing Prior to Endmember Extraction from Hyperspectral Data. *IEEE International Geoscience and Remote Sensing Symposium (IGARSS'2011)*, Vancouver, Canada, 2011. This work was presented as an oral presentation in the workshop *IGARSS* in 2011. This workshop is attended by thousands of researchers worldwide in the remote sensing field, and it is the most international important workshop in the remote sensing area. In this work, we presented part of the SSPP technique for spatial preprocessing which has been extensively discussed in the thesis work. The candidate contributed with the development and design of the new preprocessing technique and also performed all the experiments for the comparative assessment with the fractal synthetic image database and also with the real image of Cuprite.

9. G. Martin and A. Plaza. Spatial-Spectral Preprocessing for Volume-Based Endmember Extraction Algorithms Using Unsupervised Clustering. *IEEE GRSS Workshop on Hyperspectral Image and Signal Processing: Evolution in Remote Sensing (WHISPERS'2010)*, Reykjavik, Iceland, 2010. This work was presented as an oral presentation in the *IEEE WHISPERS* which is one of the most important international workshops specialized in hyperspectral remote sensing. In this paper we presented the RBSPP technique developed in this thesis work. The paper also includes a comparative assessment of the RBSPP technique in combination with other algorithms for endmember extraction that assume the presence of pure pixel in the data. Experimental results with synthetic and real hyperspectral data, collected over the Cuprite mining district, were performed in this work. The candidate contributed with the design and development of the RBSPP technique and the development of all the experimental results for the comparative assessment.

10. G. Martin and A. Plaza. Spatial Preprocessing for Endmember Extraction Using Unsupervised Clustering and Orthogonal Subspace Projection Concepts. *IEEE*

International Geoscience and Remote Sensing Symposium (IGARSS'2010), Hawaii, USA, 2010. This work was presented as an oral presentation in the workshop *IEEE IGARSS* in 2010. This workshop is attended by thousands of researchers worldwide in the remote sensing field, and it is the most international important workshop in the remote sensing area.. The paper presents a new technique for spatial preprocessing corresponding to the first steps of the design of the RBSPP. The paper includes a comparative assessment of the proposed technique in combination with other algorithms for endmember extraction that assume the presence of pure pixels in the data. Experimental results with the fractal synthetic image database were also performed in this work. The candidate contributed with the design and development of the preprocessing technique and achievement of all the experimental results for the comparative assessment.

11. S. Sanchez, G. Martin and A. Plaza. Parallel Implementation of the N-FINDR Endmember Extraction Algorithm on Commodity Graphics Processing Units. *IEEE International Geoscience and Remote Sensing Symposium (IGARSS'2010)*, Hawaii, USA, 2010. This work was presented in the workshop *IEEE IGARSS* in 2010. This workshop is attended by thousands of researchers worldwide in the remote sensing field, and it is the most international important workshop in the remote sensing area. The paper presents a methodology to implement the N-FINDR algorithm in GPU architectures. The paper shows the results of the algorithm implemented in GPU with regards to an optimized implementation of the N-FINDR algorithm in a non-parallel architecture. The candidate contributed with support in the design of the methodology for the implementation of the N-FINDR algorithm in the GPU architecture.

12. S. Sanchez, G. Martin, A. Plaza and C.-I Chang. GPU Implementation of Fully Constrained Linear Spectral Unmixing for Remotely Sensed Hyperspectral Data Exploitation. *SPIE Optics and Photonics, Satellite Data Compression, Communication, and Processing Conference*, San Diego, CA, 2010. This work was presented an an oral presentation in the workshop *SPIE Optics and Photonics*. This workshop is attended by thousands of researchers worldwide in the remote sensing field, and it is one of the most international important workshop in the remote sensing area. The paper presents new parallel implementations of unconstrained, partially constrained and fully constrained linear spectral unmixing algorithms. The implementations were developed in GPUs. The candidate contributed with support in the design of the implementation of this techniques in the GPU architecture.

13. A. Plaza, J. Plaza, I. Dopido, G. Martin, M. D. Iordache and S. Sanchez. New Hyperspectral Unmixing Techniques in the Framework of the Earth Observation Optical Data Calibration and Information Extraction (EODIX) Project. *3rd International Symposium on Recent Advances in Quantitative Remote Sensing (RAQRS'2010)*, Valencia, Spain, 2010. In this paper, we describe some of the advances carried out in one of the tasks of the EODIX project, focused on the area

of spectral unmixing and classification of remotely sensed data. The candidate contributed with the development of the spatial preprocessing techniques presented in this work.

14. S. Sanchez, G. Martin, A. Plaza and J. Plaza. Near Real-Time Endmember Extraction from Remotely Sensed Hyperspectral Data Using NVidia GPUs. *SPIE Photonics Europe, Real-Time Image and Video Processing Conference*, Brussels, Belgium, 2010. This paper was presented in the *SPIE Photonics Europe* which congregated a huge amount of researchers in the area of remote sensing. The paper presents a new parallel implementation of the N-FINDR algorithm. The implementations was developed in GPUs. The candidate contributed with support in the design of the implementation of this technique in the GPU architecture.

15. A. Plaza, J. Plaza and G. Martin. Spatial-Spectral Endmember Extraction from Hyperspectral Imagery Using Multi-Band Morphology and Volume Optimization. *IEEE International Conference on Image Processing (ICIP'2009)*, Cairo, Egypt, 2009. This work was presented an an oral presentation in the *IEEE ICIP*, sponsored by the *IEEE Signal Processing Society*. This conference is the premier forum for the presentation of technological advances and research results in the fields of theoretical, experimental, and applied image and video processing. The paper presents a new approach for characterization of mixed pixels in remotely sensed hyperspectral images which first performs joint spatial-spectral pixel characterization via extended morphological transformations, and then automatically extracts endmembers using volume optimization and convex geometry concepts. The candidate contributed with the development of the experimental results presented in this work.

16. A. Plaza, J. Plaza and G. Martin. Incorporation of Spatial Constraints into Spectral Mixture Analysis of Remotely Sensed Hyperspectral Data. *IEEE International Workshop on Machine Learning for Signal Processing (MLSP'2009)*, Grenoble, France, 2009. This work was presented in an oral presentation in the *IEEE MLSP* which is the main workshop organized by the *Machine Learning for Signal Processing Technical Committee* under the *IEEE Signal Processing Society*. In this paper we discuss the advantages that can be obtained after including spatial information in techniques for endmember extraction and fractional abundance estimation, using a database of synthetic hyperspectral scenes with artificial spatial patterns generated using fractals, and a real hyperspectral scene collected by AVIRIS sensor in the Cuprite mining district. The candidate contributed with the development of the experimental results presented in this work.

17. A. Plaza, G. Martin and M. Zortea. On the Incorporation of Spatial Information to Spectral Mixture Analysis: Survey and Algorithm Comparison. *IEEE GRSS Workshop on Hyperspectral Image and Signal Processing: Evolution in Remote Sensing (WHISPERS'2009)*, Grenoble, France, 2009. This work was presented in an oral presentation in the *IEEE WHISPERS* in 2009 which is one of the most

important international workshops specialized in hyperspectral remote sensing. In this paper, we provide a survey on the use of spatial information in endmember extraction and further compare six different algorithms (three of which only use spectral information) in order to substantiate the impact of using spatial-spectral information versus only spectral information when searching for image endmembers. The comparison is carried out using a synthetic hyperspectral scene with spatial patterns generated using fractals, and a real hyperspectral scene collected by AVIRIS sensor in the Cuprite mining district. The candidate contributed with the development of the experimental results presented in this work.

18. A. Plaza, G. Martin and M. Zortea. Analysis of Different Strategies for Incorporating Spatial Information in Endmember Extraction from Hyperspectral Data. *IEEE International Geoscience and Remote Sensing Symposium (IGARSS'09)*, Cape Town, South Africa, 2009. This work was presented in the workshop *IEEE IGARSS* in 2012. This workshop is attended by thousands of researchers worldwide in the remote sensing field, and it is the most international important workshop in the remote sensing area. In this paper, we present a thorough analytical comparison of endmember extraction methods which include spatial information in the search of spectral endmembers versus a few algorithms which are exclusively based on spectral information. Our quantitative and comparative assessment of algorithm accuracy and computational performance, conducted using both synthetic and real hyperspectral data, provides interesting findings about the potential benefits that can be obtained after incorporating spatial information into the design of endmember extraction algorithms. The candidate contributed with the development of the experimental results presented in this work.

Bibliography

[1] H. Akaike. A new look at the statistical model identification. 19(6):716–723, 1974. [Cited in pag. 8]

[2] A. Plaza, P. Martinez, R. Perez, and J. Plaza. Spatial/spectral endmember extraction by multidimensional morphological operations. *IEEE Trans. Geosci. Remote Sens.*, 40(9):2025–2041, 2002. [Cited in pags. 8, 19, 25 and 31]

[3] C.-I Chang and D. Heinz. Constrained subpixel target detection for remotely sensed imagery. *IEEE Trans. Geosci. Remote Sens.*, 38:1144–1159, 2000. [Cited in pags. 8, 13 and 23]

[4] D. Heinz and C.-I. Chang. Fully constrained least squares linear mixture analysis for material quantification in hyperspectral imagery. *IEEE Trans. Geosci. Remote Sens.*, 39:529–545, 2001. [Cited in pags. 8, 13 and 60]

[5] R. O. Green, M. L. Eastwood, C. M. Sarture, T. G. Chrien, M. Aronsson, B. J. Chippendale, J. A. Faust, B. E. Pavri, C. J. Chovit, M. Solis, M. R. Olah, and Orlesa Williams. Imaging spectroscopy and the airborne visible/infrared imaging spectrometer (aviris). *Remote Sens. Environ.*, 65:227–248, 1998. [Cited in pag. 8]

[6] A. Ifarraguerri and C.-I Chang. Multispectral and hyperspectral image analysis with convex cones. *IEEE Trans. Geosci. Remote Sens.*, 37(2):756–770, 1999. [Cited in pag. 8]

[7] J. M. Bioucas-Dias and J. M. P. Nascimento. Hyperspectral subspace identification. *IEEE Trans. Geosci. Remote Sens.*, 46(8):2435–2445, 2008. [Cited in pags. 8, 32, 37, 42, 50, 62 and 67]

[8] R. A. Neville, K. Staenz, T. Szeredi, J. Lefebvre, and P. Hauff. Automatic endmember extraction from hyperspectral data for mineral exploration. *Proc. 21st Canadian Symp. Remote Sens.*, pages 21–24, 1999. [Cited in pag. 8]

[9] A. A. Green, M. Berman, P. Switzer, and M. D. Craig. A transformation for ordering multispectral data in terms of image quality with implications for noise removal. *IEEE Trans. Geosci. Remote Sens.*, 26:65–74, 1988. [Cited in pag. 8]

[10] J. Li and J. Bioucas-Dias. Minimum volume simplex analysis: a fast algorithm to unmix hyperspectral data. In *IEEE International Geoscience and Remote Sensing Symposium*, volume 3, pages 250–253, 2008. [Cited in pags. 8 and 22]

[11] J. B. Lee, S. Woodyatt, and M. Berman. Enhancement of high spectral resolution remote-sensing data by noise-adjusted principal components transform. *IEEE Trans. Geosci. Remote Sens.*, 28(3):295–304, 1990. [Cited in pags. 8 and 15]

[12] G. Schwarz. Estimating the dimension of a model. *Ann. Stat.*, 6:461–464, 1978. [Cited in pag. 8]

[13] J. Rissanen. Modeling by shortest data description. *Automatica*, 14:465–471, 1978. [Cited in pag. 8]

[14] J. H. Bowles, P. J. Palmadesso, J. A. Antoniades, M. M. Baumback, and L. J. Rickard. Use of filter vectors in hyperspectral data analysis. *Proc. SPIE Infrared Spaceborne Remote Sensing III*, 2553:148–157, 1995. [Cited in pag. 8]

[15] H. Ren and C.-I Chang. Automatic spectral target recognition in hyperspectral imagery. *IEEE Trans. Aerosp. Electron. Syst.*, 39(4):1232–1249, 2003. [Cited in pags. 8 and 18]

[16] I.T. Jolliffe. *Principal Component Analysis*. New York: Spriger Verlag, 1986. [Cited in pags. 8 and 37]

[17] J. W. Boardman, F. A. Kruse, and R. O. Green. Mapping Target Signatures Via Partial Unmixing of Aviris Data. *Proc. JPL Airborne Earth Sci. Workshop*, pages 23–26, 1995. [Cited in pags. 8 and 11]

[18] G. Martin and A. Plaza. Region-based spatial preprocessing for endmember extraction and spectral unmixing. *IEEE Geosci. Remote Sens. Lett.*, 8(4):745–749, 2011. [Cited in pags. 8 and 31]

[19] N. Keshava and J. F. Mustard. Spectral unmixing. *IEEE Signal Process. Mag.*, 19(1):44–57, 2002. [Cited in pags. 8, 19, 33 and 37]

[20] J. Bioucas-Dias. A variable splitting augmented lagragian approach to linear spectral unmixing. In *IEEE Hyperspectral Image and Signal Processing: Evolution in Remote Sensing*, pages 1–4, 2009. [Cited in pags. 8 and 22]

[21] M. Zortea and A. Plaza. Spatial preprocessing for endmember extraction. *IEEE Trans. Geosci. Remote Sens.*, 47(8):2679–2693, 2009. [Cited in pags. 8, 27 and 31]

[22] G. Martin and A. Plaza. Spatial-spectral preprocessing prior to endmember identification and unmixing of remotely sensed hyperspectral data. *IEEE J. Sel. Topics Appl. Earth Observations Remote Sens.*, 5(2):380–395, 2012. [Cited in pags. 8 and 35]

[23] D. M. Rogge, B. Rivard, J. Zhang, A. Sanchez, J. Harris, and J. Feng. Integration of spatial–spectral information for the improved extraction of endmembers. *Remote Sens. Environ.*, 110(3):287–303, 2007. [Cited in pags. xi, 8, 20, 21, 26 and 31]

[24] L. L. Scharf. *Statistical Signal Processing, Detection Estimation and Time Series Analysis*. Addison-Wesley, 1991. [Cited in pag. 8]

[25] C.-I Chang and Q. Du. Estimation of number of spectrally distinct signal sources in hyperspectral imagery. *IEEE Trans. Geosci. Remote Sens.*, 42(3):608–619, 2004. [Cited in pags. 8, 23, 32, 37 and 62]

[26] J. M. P. Nascimento and J. M. Bioucas-Dias. Vertex Component Analysis: A Fast Algorithm to Unmix Hyperspectral Data. *IEEE Trans. Geosci. Remote Sens.*, 43(4):898–910, 2005. [Cited in pags. 8, 18 and 67]

[27] A. F. H. Goetz and B. Kindel. Comparison of unmixing result derived from aviris, high and low resolution, and Hydice images at Cuprite, NV. In *Proceedings IX NASA/JPL Airborne Earth Science Workshop*, Pasadena, California, 1999. [Cited in pag. 7]

[28] D. Landgrebe. *Multispectral Data Analysis, A Signal Theory Perspective*. Springer Hoboken, NJ, 1998. [Cited in pag. 7]

[29] R. A. Schowengerdt. *Remote Sensing: Models and Methods for Image Processing, 2nd ed.* Academic Press: New York, 1997. [Cited in pags. 7, 26 and 30]

[30] J. Chanussot, M. M. Crawford, and B.-C. Kuo. Foreword to the special issue on hyperspectral image and signal processing. *IEEE Trans. Geosci. Remote Sens.*, 48(11):3871–3876, 2010. [Cited in pag. 7]

[31] A. Plaza, Q. Du, J. Bioucas-Dias, X. Jia, and F. Kruse. Foreword to the special issue on spectral unmixing of remotely sensed data. *IEEE Trans. Geosci. Remote Sens.*, 49(11):4103–4110, 2011. [Cited in pags. 7 and 8]

[32] A. Plaza, J. Plaza, G. Martin, and S. Sanchez. Hyperspectral data processing algorithms. In J. G. Lyon P. S. Thenkabail and A. Huete, editors, *Hyperspectral Remote Sensing of Vegetation*, chapter 5, pages 121–137. Taylor and Francis, "Abingdon, United Kingdom", 2011. [Cited in pag. 7]

[33] A. Plaza, J. A. Benediktsson, J. Boardman, J. Brazile, L. Bruzzone, G. Camps-Valls, J. Chanussot, M. Fauvel, P. Gamba, J.A. Gualtieri, M. Marconcini, J. C. Tilton, and G. Trianni. Recent advances in techniques for hyperspectral image processing. 113:110–122, 2009. [Cited in pag. 10]

[34] D. Manolakis and G. Shaw. Detection algorithms for hyperspectral imaging aplications. 19(1):29–43, 2002. [Cited in pag. 10]

[35] J. M. Bioucas-Dias, A. Plaza, N. Dobigeon, M. Parente, Q. Du, P. Gader, and J. Chanussot. Hyperspectral unmixing overview: Geometrical, statistical and sparse regression-based approaches. *IEEE J. Sel. Topics Appl. Earth Observations Remote Sens.*, 5(2):354–379, 2012. [Cited in pags. 11, 12, 40 and 42]

[36] J. B. Adams, M. O. Smith, and P. E. Johnson. Spectral mixture modeling: a new analysis of rock and soil types at the Viking Lander 1 site. 91:8098–8112, 1986. [Cited in pag. 11]

[37] A. R. Gillespie, M. O. Smith, J. B. Adams, S. C. Willis, A. F. Fisher, and D. E. Sabol. Interpretation of residual images: Spectral mixture analysis of AVIRIS images, Owens Valley, California. In R. O. Green, editor, *Proc. 2nd AVIRIS Workshop*, volume 90–54, pages 243–270, 1990. [Cited in pag. 11]

[38] J. J. Settle and N. A. Drake. Linear mixing and the estimation of ground cover proportions. 14:1159–1177, 1993. [Cited in pag. 11]

[39] R. O. Green, M. L. Eastwood, C. M. Sarture, T. G. Chrien, M. Aronsson, B. J. Chippendale, J. A. Faust, B. E. Pavri, C. J. Chovit, M. Solis, et al. Imaging spectroscopy and the airborne visible/infrared imaging spectrometer (AVIRIS). 65(3):227–248, 1998. [Cited in pag. 11]

[40] D. Heinz and C.-I Chang. Fully constrained least squares linear mixture analysis for material quantification in hyperspectral imagery. *IEEE Trans. Geosci. Remote Sens.*, 39:529–545, 2001. [Cited in pag. 11]

[41] A. Plaza, P. Martinez, R. Perez, and J. Plaza. A quantitative and comparative analysis of endmember extraction algorithms from hyperspectral data. *IEEE Trans. Geosci. Remote Sens.*, 42(3):650–663, 2004. [Cited in pags. 11, 15 and 26]

[42] A. Plaza, G. Martin, J. Plaza, M. Zortea, and S. Sanchez. Recent developments in spectral unmixing and endmember extraction. In S. Prasad, L. M. Bruce, and J. Chanussot, editors, *Optical Remote Sensing*, chapter 12, pages 235–267. Springer-Verlag, Berlin, Germany, 2011. [Cited in pags. 11 and 12]

[43] C.-I Chang. *Hyperspectral Imaging: Techniques for Spectral Detection and Classification.* Kluwer Academic/Plenum Publishers: New York, 2003. [Cited in pags. 11, 19 and 23]

[44] K. J. Guilfoyle, M. L. Althouse, and C.-I Chang. A quantitative and comparative analysis of linear and nonlinear spectral mixture models using radial basis function neural networks. *IEEE Trans. Geosci. Remote Sens.*, 39:2314–2318, 2001. [Cited in pag. 12]

[45] J. Plaza, A. Plaza, R. Perez, and P. Martinez. On the use of small training sets for neural network-based characterization of mixed pixels in remotely sensed hyperspectral images. *Pattern Recognition*, 42:3032–3045, 2009. [Cited in pag. 12]

[46] C. C. Borel and S. A. W. Gerstl. Nonlinear spectral mixing model for vegetative and soil surfaces. 47(3):403–416, 1994. [Cited in pag. 12]

[47] B. Hapke. *Theory of Reflectance and Emittance Spectroscopy.* Cambridge Univ. Press, 1993. [Cited in pag. 12]

[48] J. M. Bioucas-Dias and A. Plaza. Hyperspectral unmixing: geometrical, statistical, and sparse regression-based approaches. In *Proc. SPIE Image and Signal Process. Remote Sens. XVI*, volume 7830, pages 1–15, 2010. [Cited in pag. 12]

[49] M. Parente and A. Plaza. Survey of geometric and statistical unmixing algorithms for hyperspectral images. In *IEEE Hyperspectral Image and Signal Processing: Evolution in Remote Sensing*, pages 1–4, 2010. [Cited in pag. 12]

[50] A. Plaza, P. Martinez, R. Perez, and J. Plaza. A quantitative and comparative analysis of endmember extraction algorithms from hyperspectral data. *IEEE Trans. Geosci. Remote Sens.*, 42(3):650–663, 2004. [Cited in pag. 12]

[51] G. Shaw and H. Burke. Spectral imaging for remote sensing. *Lincoln Lab. J.*, 14(1):3–28, 2003. [Cited in pag. 12]

[52] N. Keshava and J. F. Mustard. Spectral unmixing. 19(1):44–57, 2002. [Cited in pag. 12]

[53] N. Keshava, J. Kerekes, D. Manolakis, and G. Shaw. An algorithm taxonomy for hyperspectral unmixing. In *Proc. SPIE AeroSense Conference on Algorithms for Multispectral and Hyperspectral Imagery VI*, volume 4049, pages 42–63, 2000. [Cited in pag. 12]

[54] Y. H. Hu, H. B. Lee, and F. L. Scarpace. Optimal linear spectral unmixing. *IEEE Trans. Geosci. Remote Sens.*, 37:639–644, 1999. [Cited in pag. 12]

[55] M. Petrou and P. G. Foschi. Confidence in linear spectral unmixing of single pixels. *IEEE Trans. Geosci. Remote Sens.*, 37:624–626, 1999. [Cited in pag. 12]

[56] J.J. Settle. On the relationship between spectral unmixing and subspace projection. *IEEE Trans. Geosci. Remote Sens.*, 34:1045–1046, 1996. [Cited in pag. 12]

[57] A. S. Mazer and M. Martin. Image processing software for imaging spectrometry data analysis. 24(1):201–210, 1988. [Cited in pag. 12]

[58] R. H. Yuhas, A. F. H. Goetz, and J. W. Boardman. Discrimination among semi-arid landscape endmembres using the spectral angle mapper (SAM) algorithm. In *Proc. Ann. JPL Airborne Geosci. Workshop, R. O. Green, Ed. Publ., 92-14*, volume 1, pages 147–149, 1992. [Cited in pag. 12]

[59] J. C. Harsanyi and C.-I Chang. Hyperspectral image classification and dimensionality reduction: An orthogonal subspace projection approach. *IEEE Trans. Geosci. Remote Sens.*, 32(4):779–785, 1994. [Cited in pag. 12]

[60] C. Chang, X. Zhao, M. L. G. Althouse, and J. J. Pan. Least squares subspace projection approach to mixed pixel classification for hyperspectral images. *IEEE Trans. Geosci. Remote Sens.*, 36(3):898–912, 1998. [Cited in pag. 12]

[61] D. C. Heinz, C.-I. Chang, and M. L. G. Althouse. Fully constrained least squares-based linear unmixing. In *IEEE International Geoscience and Remote Sensing Symposium*, volume 1, pages 1401–1403, 1999. [Cited in pag. 12]

[62] R. B. Singer and T. B. McCord. Mars: Large scale mixing of bright and dark surface materials and implications for analysis of spectral reflectance. In *Proc. Lunar and Planetary Sci. Conf.*, pages 1835–1848, 1979. [Cited in pag. 12]

[63] B. Hapke. Bidirection reflectance spectroscopy. I. theory. 86:3039–3054, 1981. [Cited in pag. 12]

[64] R. N. Clark and T. L. Roush. Reflectance spectroscopy: Quantitative analysis techniques for remote sensing applications. 89(7):6329–6340, 1984. [Cited in pag. 12]

[65] C.-I Chang and Q. Du. Estimation of number of spectrally distinct signal sources in hyperspectral imagery. *IEEE Trans. Geosci. Remote Sens.*, 42(3):608–619, 2004. [Cited in pag. 15]

[66] M. Wax and T. Kailath. Detection of signals by information theoretic criteria. *IEEE Trans. Acoust. Speech Signal Process.*, 33(2):387–392, 1985. [Cited in pag. 15]

[67] J. Harsanyi, W. Farrand, and C.-I. Chang. Determining the number and identity of spectral endmembers: An integrated approach using Neyman-Pearson eigenthresholding and iterative constrained RMS error minimization. In *Proc. Thematic Conf. Geologic Remote Sens.*, volume 1, pages 1–10, 1993. [Cited in pag. 15]

[68] M. Berman, H. Kiiveri, R. Lagerstrom, A. Ernst, R. Dunne, and J. F Huntington. ICE: a statistical approach to identifying endmembers in hyperspectral images. *IEEE Trans. Geosci. Remote Sens.*, 42(10):2085–2095, 2004. [Cited in pags. 16 and 22]

[69] L. Miao and H. Qi. Endmember extraction from highly mixed data using minimum volume constrained nonnegative matrix factorization. *IEEE Trans. Geosci. Remote Sens.*, 45(3):765–777, 2007. [Cited in pags. 16 and 22]

[70] C.-I. Chang, C.-C. Wu, W. Liu, and Y.-C. Ouyang. A new growing method for simplex-based endmember extraction algorithm. *IEEE Trans. Geosci. Remote Sens.*, 44(10):2804–2819, 2006. [Cited in pag. 16]

[71] J. Wang and C.-I. Chang. Applications of independent component analysis in endmember extraction and abundance quantification for hyperspectral imagery. *IEEE Trans. Geosci. Remote Sens.*, 44(9):2601–2616, 2006. [Cited in pag. 16]

[72] A. Plaza and C.-I Chang. Impact of initialization on design of endmember extraction algorithms. *IEEE Trans. Geosci. Remote Sens.*, 44(11):3397–3407, 2006. [Cited in pag. 16]

[73] C.-I Chang and A. Plaza. A fast iterative algorithm for implementation of pixel purity index. 3(1):63–67, 2006. [Cited in pag. 16]

[74] A. Zare and P. Gader. Hyperspectral band selection and endmember detection using sparsity promoting priors. *IEEE Geosci. Remote Sens. Lett.*, 5(2):256–260, 2008. [Cited in pag. 16]

[75] T.-H. Chan, W.-K. Ma, A. Ambikapathi, and C.-Y. Chi. A simplex volume maximization framework for hyperspectral endmember extraction. *IEEE Trans. Geosci. Remote Sens.*, 49(11):4177–4193, 2011. [Cited in pag. 16]

[76] A. Plaza, P. Martinez, J. Plaza, and R. Perez. Dimensionality reduction and classification of hyperspectral image data using sequences of extended morphological transformations. *IEEE Trans. Geosci. Remote Sens.*, 43(3):466–479, 2005. [Cited in pags. 16 and 19]

[77] C.-I Chang. *Hyperspectral Data Exploitation: Theory and Applications*. John Wiley & Sons: New York, 2007. [Cited in pag. 17]

[78] J. C. Harsanyi and C.-I Chang. Hyperspectral image classification and dimensionality reduction: An orthogonal subspace projection. *IEEE Trans. Geosci. Remote Sens.*, 32(4):779–785, 1994. [Cited in pag. 17]

[79] E. M. T. Hendrix, I. Garcia, J. Plaza, G. Martin, and A. Plaza. A new minimum volume enclosing algorithm for endmember identification and abundance estimation in hyperspectral data. *IEEE Trans. Geosci. Remote Sens.*, 50(2):2744–2757, 2012. [Cited in pag. 21]

[80] J. Plaza, E. M. T. Hendrix, I. Garcia, G. Martin, and A. Plaza. On endmember identification in hyperspectral images without pure pixels: A comparison of algorithms. *Journal of Mathematical Imaging and Vision*, 42(2-3):163–175, 2012. [Cited in pag. 21]

[81] M. D. Craig. Minimum-volume transforms for remotely sensed data. *IEEE Trans. Geosci. Remote Sens.*, 32:542–552, 1994. [Cited in pag. 22]

[82] Y Qian, S. Jia, J. Zhou, and A. Robles-Kelly. Hyperspectral unmixing via l1/2 sparsity-constrained nonnegative matrix factorization. *IEEE Trans. Geosci. Remote Sens.*, 49(11):4282–4297, 2011. [Cited in pag. 22]

[83] A. Zymnis, S.-J. Kim, J. Skaf, M. Parente, and S. Boyd. Hyperspectral image unmixing via alternating projected subgradients. In *41st Asilomar Conference on Signals, Systems, and Computers, Pacific Grove, CA*, 2007. [Cited in pags. 22 and 25]

[84] A. Zare and P. Gader. Sparsity promoting iterated constrained endmember detection in hyperspectral imagery. *IEEE Geosci. Remote Sens. Lett.*, 4(3):446–450, 2007. [Cited in pag. 22]

[85] J. Li, M. Bioucas-Dias, and A. Plaza. Collaborative nonnegative matrix factorization for remotely sensed hyperspectral unmixing. In *IEEE Geoscience and Remote Sensing Symposium (IGARSS), Munich, Germany, July 22-27*, 2012. [Cited in pag. 22]

[86] T.-H. Chan, C.-Y. Chi, Y.-M. Huang, and W.-K. Ma. A convex analysis based minimum-volume enclosing simplex algorithm for hyperspectral unmixing. *IEEE Trans. Signal Process.*, 57(11):4418–4432, 2009. [Cited in pag. 22]

[87] A. Ambikapathi, T.-H. Chan, W.-K. Ma, and C.-Y. Chi. Chance-constrained robust minimum-volume enclosing simplex algorithm for hyperspectral unmixing. *IEEE Trans. Geosci. Remote Sens.*, 49(11):4194–4209, 2011. [Cited in pag. 22]

[88] J. Sigurdsson, M. O. Ulfarsson, J. R. Sveinsson, and J. A. Benediktsson. A smooth hyperspectral unmixing method using cyclic descent. In *IEEE Geoscience and Remote Sensing Symposium (IGARSS), Munich, Germany, July 22-27*, 2012. [Cited in pag. 25]

[89] O. Eches, N. Dobigeon, and J-Y Tourneret. Enhancing hyperspectral image unmixing with spatial correlations. *IEEE Trans. Geosci. Remote Sens.*, 49(11):4239–4247, 2011. [Cited in pag. 25]

[90] G. Martin and A. Plaza. Spatial-spectral preprocessing for volume-based endmember extraction algorithms using unsupervised clustering. In *IEEE GRSS Workshop on Hyperspectral Image and Signal Processing: Evolution in Remote Sensing (WHISPERS'2010), Reykjavik, Iceland*, 2010. [Cited in pag. 31]

[91] G. Ball and D. Hall. ISODATA, a novel method of data analysis and classification. *Tech. Rep. AD-699616, Stanford University*, 1965. [Cited in pag. 33]

[92] J. A. Hartigan and M. A. Wong. Algorithm as 136: A k-means clustering algorithm. *Journal of the Royal Statistical Society, Series C (Applied Statistics)*, 28:100–108, 1979. [Cited in pags. 33 and 49]

[93] J. C. Tilton. Analysis of hierarchically related image segmentations. *Proc. IEEE Workshop Adv. Tech. Anal. Remotely Sensed Data*, pages 60–69, 2003. [Cited in pags. 33 and 57]

[94] J. C. Tilton. HSEG/RHSEG, HSEGViewer and HSEG-Reader User's Manual (Version 1.40). *[ONLINE]. Available: http://techtransfer.gsfc.nasa.gov/ft_tech_rhseg.shtm*, 2008. [Cited in pag. 33]

[95] G. Martin and A. Plaza. Spatial preprocessing for endmember extraction using unsupervised clustering and orthogonal subspace projection concepts. In *IEEE International Geoscience and Remote Sensing Symposium (IGARSS'10), Hawaii*, 2010. [Cited in pag. 34]

[96] J. A. Richards and X. Jia. *Remote Sensing Digital Image Analysis: An Introduction*. Springer, 2006. [Cited in pags. 35 and 37]

[97] G. Martin and A. Plaza. Joint spectral and spatial preprocessing prior to endmember extraction from hyperspectral images. In *SPIE Optics and Photonics, Satellite Data Compression, Communication, and Processing Conference, San Diego, CA*, 2011. [Cited in pag. 35]

[98] G. Martin, A. Plaza, and M. Zortea. Noise-robust spatial preprocessing prior to endmember extraction from hyperspectral data. In *IEEE International Geoscience*

and Remote Sensing Symposium (IGARSS'2011), Vancouver, Canada, 2011. [Cited in pag. 35]

[99] G. Martin, J. Plaza, and A. Plaza. On the incorporation of spatial information to endmember identification algorithms without the pure pixel assumption. In *IEEE GRSS Workshop on Hyperspectral Image and Signal Processing: Evolution in Remote Sensing (WHISPERS'11), Lisbon, Portugal*, 2011. [Cited in pag. 38]

[100] G. Motta, F. Rizzo, and J. A. Storer. *Hyperspectral data compression*. Berlin: Springer, 2006. [Cited in pag. 39]

[101] B. Huang. *Satellite data compression*. Berlin: Springer, 2011. [Cited in pag. 39]

[102] G. Martin, V. Gonzalez-Ruiz, A. Plaza, J. P. Ortiz, and I. Garcia. Impact of jpeg2000 compression on endmember extraction and unmixing of remotely sensed hyperspectral data. *Journal of Applied Remote Sensing*, 4:41796–41820, 2010. [Cited in pag. 39]

[103] Q. Du and J. E. Fowler. Low-complexity principal component analysis for hyperspectral image compression. *International Journal of High Performance Computing Applications*, 22:273–286, 2009. [Cited in pag. 39]

[104] Ch. Song, Y. Li, and B. Huang. A GPU-accelerated wavelet decompression system with SPIHT and Reed-Solomon decoding for satellite images. *IEEE J. Sel. Topics Appl. Earth Observations Remote Sens.*, 4(3), 2011. [Cited in pag. 39]

[105] S.-Ch. Wei and B. Huang. GPU acceleration of predictive partitioned vector quantization for ultraspectral sounder data compression. *IEEE J. Sel. Topics Appl. Earth Observations Remote Sens.*, 4(3):677–682, 2011. [Cited in pag. 39]

[106] D. L. Donoho. Compressed sensing. *IEEE Trans. Inf. Theory*, 52(4):1289–1306, 2006. [Cited in pags. 39 and 41]

[107] E.J. Candes, J. Romberg, and T. Tao. Robust uncertainty principles: Exact signal reconstruction from highly incomplete frequency information. *IEEE Trans. Inf. Theory*, 52(2):489–509, 2006. [Cited in pag. 39]

[108] G. Martin, J. Bioucas-Dias, and A. Plaza. Hyperspectral coded aperture: A new algorithm for hyperspectral compressive sensing. In *IEEE Geoscience and Remote Sensing Symposium (IGARSS'2012), Munich, Germany*, 2012. [Cited in pag. 39]

[109] G. Martin, J. Bioucas-Dias, and A. Plaza. Hyperspectral coded aperture: A new technique for hyperspectral unmixing. In *European Signal Processing Conference (EUSIPCO'2013), Marrakesch, Morocco*, 2013. [Cited in pag. 39]

[110] G. Martin, J. Bioucas-Dias, and A. Plaza. A new technique for hyperspectral compressive sensing using spectral unmixing. In *SPIE Optics and Photonics, Satellite Data Compression, Communication, and Processing Conference, San Diego, CA*, 2012. [Cited in pag. 39]

[111] L. Rudin, S. Osher, and E. Fatemi. Nonlinear total variation based noise removal algorithms. *Physica D*, 60:259–268, 1992. [Cited in pag. 40]

[112] M. B. Wakin M. F. Duarte D. Baron S. Sarvotham K. F. Kelly D. Takhar, J. N. Laska and R. G. Baraniuk. A new compressive imaging camera architecture using optical-domain compression. *Computational Imaging IV*, 6065:43–52, 2006. [Cited in pag. 40]

[113] D. Donoho and M. Elad. Optimal sparse representation in general (non-orthogonal) dictionaries via l1 minimization. *Proceedings of the National Academy of Sciences*, 100:2197–2202, 2003. [Cited in pag. 41]

[114] I. Gorodnitsky and B. Rao. Sparse signal reconstruction from limited data using FOCUSS: A re-weighted minimum norm algorithm. *IEEE Trans. Signal Process.*, 45(3):600–616, 1997. [Cited in pag. 41]

[115] S. Foucart and M. Lai. Sparsest solutions of underdetermined linear systems via lq-minimization for 0. *Applied and Computational Harmonic Analysis*, 26(3):395–407, 2009. [Cited in pag. 41]

[116] D. Donoho, M. Elad, and V. Temlyakov. Stable recovery of sparse overcomplete representations in the presence of noise. *IEEE Trans. Inf. Theory*, 52(1):6–18, 2006. [Cited in pag. 41]

[117] J. Tropp. Just relax: convex programming methods for subset selection and sparse approximation. *ICES report*, pages 04–04, 2004. [Cited in pag. 41]

[118] E. J. Candes, J. K. Romberg, and T. Tao. Compressive sampling and signal inference. *Commun. Pure Appl. Math.*, 59:1207–1223, 2006. [Cited in pag. 41]

[119] M. Gehm R, John, DJ D. Brady, R. Willett, and T. Schulz. Single-shot compressive spectral imaging with a dual-disperser architecture. *Optics Express*, 15(21):14013–14027, 2007. [Cited in pags. 41 and 42]

[120] A. Wagadarikar, R. John, R-Willett D., and Brady. Single disperser design for coded aperture snapshot spectral imaging. *Applied optics*, 47(10):B44–B51, 2008. [Cited in pag. 41]

[121] C. Li, T. Sun, K. Kelly, and Y. Zhang. A compressive sensing and unmixing scheme for hyperspectral data processing. *IEEE Trans. Image Process.*, 21(3):1200–1210, 2011. [Cited in pags. 41 and 42]

[122] Q. Zhang, R. Plemmons, D. Kittle, D. Brady, and S. Prasad. Joint segmentation and reconstruction of hyperspectral data with compressed measurements. *Applied Optics*, 50(22):4417–4435, 2011. [Cited in pags. 41 and 42]

[123] M. Golbabaee and P. Vandergheynst. Joint segmentation and reconstruction of hyperspectral data with compressed measurements. In *IEEE International Conference on Image Processing ICIP 2012, 2012.*, 2012. [Cited in pags. 41 and 42]

[124] P. Vandergheynst M. Golbabaee, S. Arberet. Compressive source separation: Theory and methods for hyperspectral imaging. *arXiv preprint arXiv:1208.4505*, 2012. [Cited in pags. 41 and 42]

[125] M. Lustig, D. L. Donoho, J. M. Santos, and J. M. Pauly. Compressed sensing MRI. *IEEE Signal Process. Mag.*, 2006. [Cited in pag. 41]

[126] E. Y. Sidky and X. Pan. Image reconstruction in circular conebeam computed tomography by constrained, total-variation minimization. *Phys. Med. Biol.*, 53:4777–4807, 2008. [Cited in pag. 41]

[127] D. J. Brady, K. Choi, D. L. Marks, R. Horisaki, and S. Lim. Compressive holography. *Opt. Express*, 17:13040–13049, 2009. [Cited in pag. 41]

[128] M. E. Gehm, R. John, D. J. Brady, R. M. Willett, and T. J. Schulz. Single-shot compressive spectral imaging with a dual-disperser architecture. *Opt. Express*, 15:14013–14027, 2007. [Cited in pag. 41]

[129] M. Shankar, N.P. Pitsianis, and D.J. Brady. Compressive video sensors using multichannel imagers. *Appl. Opt.*, 49:9–17, 2010. [Cited in pag. 41]

[130] S. Sanchez, A. Paz, G. Martin, and A. Plaza. Parallel unmixing of remotely sensed hyperspectral images on commodity graphics processing units. *Concurrency and Computation: Practice and Experience*, 23(13):1538–1557, 2011. [Cited in pag. 42]

[131] L. Rudin, S. Osher, and E. Fatemi. Nonlinear total variation based noise removal algorithms. *Physica D: Nonlinear Phenomena*, 60(1-4):259–268, 1992. [Cited in pag. 43]

[132] M. Afonso, J. Bioucas-Dias, and M. Figueiredo. An augmented lagrangian approach to the constrained optimization formulation of imaging inverse problems. *IEEE Trans. Image Process.*, 20(3):681–695, 2011. [Cited in pags. 43, 44, 77 and 78]

[133] J. Eckstein and D. Bertsekas. On the Douglas-Rachford splitting method and the proximal point algorithm for maximal monotone operators. *Mathematical Programming*, 5:293–318, 1992. [Cited in pags. 43, 77, 80 and 81]

[134] J. Bioucas-Dias and M. Figueiredo. Alternating direction algorithms for constrained sparse regression: Application to hyperspectral unmixing. Raykjavik, Iceland, 2010. [Cited in pag. 45]

[135] L. I. Jimenez, G. Martin, and A. Plaza. Hypermix: A new tool for quantitative evaluation of endmember identification and spectral unmixing techniques. In *IEEE Geoscience and Remote Sensing Symposium (IGARSS'2012), Munich, Germany*, 2012. [Cited in pag. 75]

[136] G. Martin, L. I. Jimenez, and A. Plaza. A new tool for evaluating spectral unmixing applications for remotely sensed hyperspectral image analysis. In *International Conference on Geographic Object-Based Image Analysis (GEOBIA), Rio de Janeiro, Brazil*, 2012. [Cited in pag. 75]

[137] E. Esser. Applications of Lagrangian-based alternating direction methods and connections to split-Bregman. Technical Report 09-31, Univ. California, 2009. [Cited in pag. 78]

[138] S. Wright, R. Nowak, and M. Figueiredo. Sparse reconstruction by separable approximation. *2011 IEEE SPS Best Paper Award, IEEE Trans. on Signal Process.*, 57(7):2479–2493, 2009. [Cited in pag. 80]

TESIS DOCTORAL

Diseño e implementación eficiente de nuevos métodos de preprocesado espacial para desmezclado de imágenes hiperespectrales de la superficie terrestre

Departamento de Tecnología de los Computadores y las Comunicaciones

Gabriel Martín Hernández
2013

TESIS DOCTORAL

Diseño e implementación eficiente de nuevos métodos de preprocesado espacial para desmezclado de imágenes hiperespectrales de la superficie terrestre

Departamento de Tecnología de los Computadores y las Comunicaciones

Gabriel Martín Hernández
2013

TESIS DOCTORAL

Diseño e implementación eficiente de nuevos métodos de preprocesado espacial para desmezclado de imágenes hiperespectrales de la superficie terrestre

Departamento de tecnología de los computadores y de las comunicaciones

Gabriel Martín Hernández

2013